CHARACTERIZATION OF CYLINDRICAL AND ELLIPTICAL TEXTURED JOURNAL BEARING

A Thesis

Submitted in partial fulfilment of the

requirements for the degree of

Doctor of Philosophy

By

THRISEKHAR REDDY GANJI

DEPARTMENT OF MECHANICAL ENGINEERING

INDIAN INSTITUTE OF TECHNOLOGY GUWAHATI

July 2015

CERTIFICATE

It is certified that the work in the thesis entitled **CHARACTERIZATION OF CYLINDRICAL AND ELLIPTICAL TEXTURED JOURNAL BEARING**, by **THRISEKHAR REDDY GANJI**, a student in the Department of Mechanical Engineering, Indian Institute of Technology Guwahati, India, for the award of the degree of Doctor of Philosophy has been carried out under my supervision and that this work has not been submitted elsewhere for a degree.

(S K Kakoty)

Professor

Department of Mechanical Engineering

Indian Institute of Technology Guwahati

February, 2015

To

My parents

And

Family members

Acknowledgement

First and foremost, with a deepest sense of gratitude, I would like to express my sincere thanks to my supervisor, Professor S. K. Kakoty, for his valuable guidance, encouragement, inspiration, creative and scientific ideas which helped me to enhance my knowledge. I appreciate all his contributions of time, ideas, and discussion to make my Ph.D. experience productive and stimulating. I would mention my heartfelt thanks for him for such a wonderful friendly nature that encouraged me to have many scientific discussions and for teachings for life, for which I remain indebted to him.

I also thank to the members of my doctoral committee: Professor S. K. Dwivedy, Professor A. K. Das and Dr. K. Kalita whose helpful suggestions increased both originality and quality of the thesis.

I am happy to acknowledge my debt to Professor Anoop K Dass, HoD of Mechanical Engineering Department for providing me with necessary arrangements to carry out my research.

Last but not the least; I thank my parents and my family members for their unconditional love, support and encouragement to pursue my interests.

Thrisekhar reddy Ganji

IIT Guwahati

Contents

List of Figures

List of Tables

Notation

a, b	Half-length of the ellipse axes in the x- and z-direction (m)
C	Radial clearance (m)
D	Diameter of the bearing (m)
$D_{rr}, D_{\phi\phi}, D_{r\phi}, D_{\phi r}$	Damping coefficients (Ns/m)
$\overline{D}_{rr}, \overline{D}_{\phi\phi}, \overline{D}_{r\phi}, \overline{D}_{\phi r}$	Non-dimensional damping coefficients, $\overline{D}_{ij} = D_{ij} C\omega / W$
e	Relative eccentricity (m)
ε	Eccentricity ratio, $\varepsilon = e/C$
$\overline{h}$	Dimensionless film thickness, $\overline{h} = h/C$
Δh	Variation of film thickness due to the presence of the texture (m)
$\overline{\Delta h}$	Dimensionless Variation of film thickness due to the presence of the texture, $\overline{\Delta h} = \Delta h/C$
$K_{rr}, K_{\phi\phi}, K_{r\phi}, K_{\phi r}$	Stiffness coefficients (N/m)
$\overline{K}_{rr}, \overline{K}_{\phi\phi}, \overline{K}_{r\phi}, \overline{K}_{\phi r}$	Non-dimensional stiffness coefficients, $\overline{K}_{ij} = K_{ij} C/W$
L	Bearing Length (m)
$M, \overline{M}$	Mass, Mass parameter, $\overline{M} = MC\omega^2/W$
p	Lubricant Pressure (Pa)

$\bar{p}$	Dimensionless Lubricant Pressure = $pC^2/6\eta UR$
$\bar{p}_0, \bar{p}_1, \bar{p}_2$	Steady-state and perturbed dimensionless pressures $\bar{p}_0 = p_0C^2/6\eta UR$
p_{max}	Maximum pressure (Pa)
$\bar{q}_z$	Non-dimensional flow coefficient, $\bar{q}_z = 2Q/ULC$
R	Radius of the journal (m)
r_p	Base radius of dimple (m)
r_1	Half-length of imaginary textured square cell (m)
r_x, r_y, r_z	Texture dimensions along x, y and z directions (m)
S	Sommerfeld number, $S = (\eta N/p)\times(R/C)^2$
S_p	Texture area density, $S_p = \pi r_p^{\,2}/4r_1^2$
t	Time (s)
U	Linear velocity (m/s)
W	Load carrying capacity (N)
$\overline{W}$	Dimensionless Load carrying capacity, $\overline{W} = WC^2/6\eta UR^2L$
x, z	Cartesian coordinates
$\bar{x}, \bar{z}$	Dimensionless Cartesian coordinates, $\bar{x} = x/r_p$, $\bar{z} = z/r_p$
x_1, z_1	Local coordinates with their origin at the center of a single dimple cell

$\overline{x_1}, \overline{z_1}$	Local dimensionless coordinates with their origin at the center of a single dimple cell, $\overline{x_1} = x_1/r_p$, $\overline{z_1} = z_1/r_p$
α	Textured portion in circumferential direction
β	Textured portion in axial direction
ϕ	Attitude angle
ξ_1, ξ_2	Dimple aspect ratios for elliptical dimples
δ	Non-dimensional clearance, $\delta = c/2r_p$
η	Dynamic viscosity (Pas)
μ	Coefficient of friction
$\overline{\mu}$	Friction variable, $\overline{\mu} = \mu(R/C)$
θ	Angular coordinate
θ_m	Maximum pressure angular position
ω, ω_p	Journal rotational speed (rad/s), frequency of journal vibration/whirl frequency (rad/s)
τ	Non dimensional time, $\tau = \omega_p t$
λ	Whirl ratio, $\lambda = \omega_p/\omega$
Λ	Bearing number, $\Lambda = 6\eta\omega/p(C/R)^2$
$(\ )_0$	Steady state value

Abstract

Surface texturing is a new emerging area of research in the field of hydrodynamic lubrication. It has been proved that texturing improves the lubrication performance of different mechanical components. In the present work, an attempt has been made to theoretically examine the influence of cylindrical and elliptical asperities on load carrying capacity, flow and friction variable of textured journal bearing. In which these performance parameters are estimated by varying textured portion, texture density, positive and negative texture depths and eccentricity ratio. Here a non-dimensional analysis is carried out to analyze the performance of cylindrical and elliptical texture on journal bearing using finite difference method. In addition, the textured performance characteristics are compared with the smooth journal bearing as well as positive and negative textured journal bearings. It has been observed that positive texture improves load carrying capacity and flow coefficient of hydrodynamic journal bearing, when it results in reduction in friction variable.

Besides, stiffness and damping coefficients of fluid film and stability parameters are estimated. Initially the Reynolds equation is perturbed using the first-order perturbation method to estimate the dynamic coefficients and then these parameters are utilized to estimate the stability parameters for different eccentricity ratios and various texture parameters like texture depth and texture portion.

The presented results are analyzed thoroughly and certain recommendations are made based on the analysis. Partial texturing in circumferential direction beyond 60% does not improve the performances of textured bearings, whereas full texturing in the axial direction is found to improve performance of the textured bearings.

CHAPTER 1
INTRODUCTION AND LITERATURE REVIEW

1.0 State of the art:

Hydrodynamic bearings are preferred due to their simplicity and ease of operation. Hydrodynamic bearings are self-acting. To create and maintain a load-carrying hydrodynamic film, it is necessary only that the bearing surfaces move relative to one another and ample lubricant is available. The lubricant film is then created as the lubricant is dragged into the clearance by the relative motion. This viscous action results in a pressure build-up within the film. The fact that hydrodynamic bearings are self-generating and do not rely on auxiliary equipment makes these bearings very reliable. Hydrodynamic journal bearings and thrust bearings are designed to support radial and axial loads, respectively, on a rotating shaft.

Sharks have used surface texture to lower friction since 200 M years. Parallel placoid riblets guide fluid flow and prevent sideway turbulence across skin. Further, in 1848 smooth balls introduced did not fly as well, after 1880 they were given texture to fly equally as well. Surface texturing has emerged in the last decade as a viable option of surface engineering resulting in significant improvement in load capacity, wear resistance, friction coefficient etc. of tribological mechanical components.

1.1 Surface roughness:

The effects of roughness and waviness play an important role on bearing performance parameter. Bearing performance parameters include the load carrying capacity**,** center of pressure, friction force, friction coefficient, flow rates and power loss. Surface roughness is characterized by deviations in shape, roughness, waviness and lattice structure.

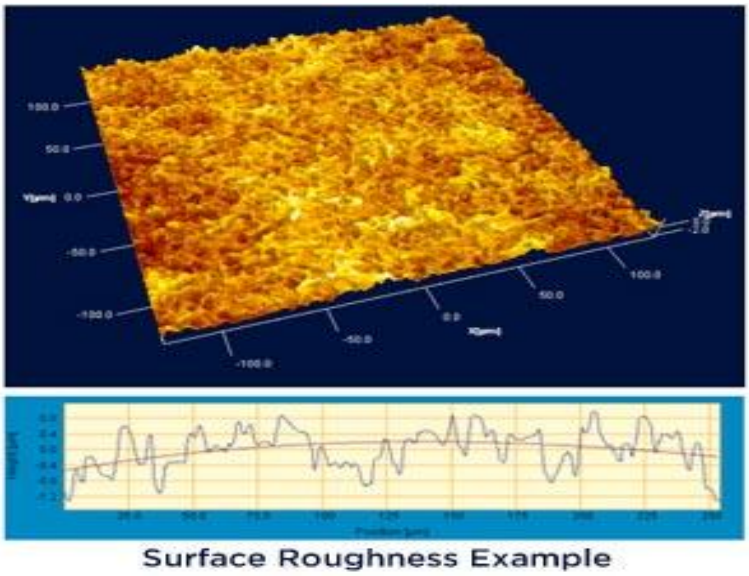

Fig 1.1: Surface roughness *(source: www.aeptechnology.com)*

1.2 Literature review:

1.2.1 Hydrodynamic textured journal bearing:

Tala-Ighil *et al.* [1] examined the influence of texture location on the hydrodynamic journal bearing performance. The theoretical results show that the most important characteristics can be improved through an appropriate arrangement of the textured area on the contact surface. Partial texturing can generate hydrodynamic lift in bearing, when the texture is located in the declining part of the contact pressure field. Ma and Zhu [2] investigated the influence of surface texture in the form of the elliptical-shape dimples with various depths, diameters, area ratios and different operation parameters on friction coefficient under conditions of hydrodynamic lubrication. Experimental results show that the optimum design model for texture parameters is valid, which may provide a theoretical reference for the tribological design of surface texture. Kraker *et al.* [3] formulated texture averaged Reynolds equation, analogous to Patir and Cheng's method for rough surfaces. The application of textured bearing surfaces results in a more complex lubricant flow pattern compared to smooth bearing surfaces. Aurelian *et al.* [4] employed finite element analysis based on the limiting shear stress model to study the influence of texture and wall slip in hydrodynamic fluid bearings. It must be noted that the extended form of the Reynolds equation developed to treat the wall slip effects is different from that used in previously presented studies.

Glu *et al.* [5] presented an analysis of the pressure development of journal bearing in various shaft surface textures and velocity variations using a proposed neural network. Adatepe *et al.* [6] investigated performances of plain and micro-grooved engine journal bearings. Numerous experiments were performed under different static loads by using the purpose-built journal bearing test rig. The results showed that the highest values of coefficient of friction as well as the frictional torque were obtained on the transversal micro-grooved journal bearings. Micro dimples are developed by incremental stamping using the structured tool. The structured tool is manufactured by focused ion beam sputtering. Interference lithography is also used for producing micro dimples on surfaces. Matsumura *et al*. [7] have studied and developed micro fabrication techniques on cylinder surface. Matsumura *et al*. [8] have also developed some micro dimples on aluminum plates. Kango *et al*. [9] investigated the impact of different forms of surface texture on finite journal bearing. It was observed that the presence of micro cavities at different locations of bearing surface help in improving the bearing performance. Brizmer and Kligerman have [10] found that both load capacity and attitude angle of the journal bearings could be improved by using partial LST mode at low eccentricities. Marian *et al*. [11] evaluated the performance of the bearing (fluid film thickness and friction torque) on a specially adapted test rig and the experimental results were compared with the theoretical model. A good agreement was observed between the theoretical model and the experimental results. Gherca *et al.* [12] proved experimentally that surface texturing represents a viable solution for increasing the load-carrying capacity of parallel fluid bearings. Li and Wang [13] have investigated the influence of the radius of the dimples on the tribological performance of a journal bearing. Results showed that the friction coefficient increased with both the width and the height of bulges in the case of journal bearing under light and moderate loading conditions.

1.2.2 Hydrodynamic textured slider bearing:

Cupillard *et al.* [14] performed analysis of a 3D inlet textured slider bearing with a temperature dependent fluid. Results showed that texture has a stronger and positive influence on load carrying capacity when thermal effects are considered. This beneficial effect was at a maximum for the longest dimples with a length shorter than the pad length. Rahmani *et al.* [15] introduced an analytical approach to study the textured surfaces in hydrodynamic lubrication regime. An optimization procedure is employed to achieve the optimum texturing parameters promoting

maximum load capacity, load capacity to lubricant flow rate ratio and minimum friction coefficient for asymmetric partially textured slider bearings.

Tønder [16] studied surface texturing effects on the properties of pivoted plane hydrodynamic bearings by numerical simulation based on the Reynolds equation. Tønder [17] studied two structure patterns, i.e. checkerboard and sinusoidal dimples**.** The tailored surfaces showed a consistent improvement in performance compared to the smooth ones. The effects were, however, less marked than those of the best combinations of striations and macro-geometries. Tønder [18] studied effects of striated, transversely oriented texturing on pivoted gas lubricated sliders and suggested that texturing liquid lubricated bearings may, under certain conditions, prevent bearing failure caused by bubble-induced compressibility of the lubricant. Wolski *et al.* [19] introduced partition iterated function system (PIFS) model, which encapsulates information about 3D topography of textured surfaces. In this study, this issue was addressed using a textured hydrodynamic pad bearing. The results obtained showed that PIFS models might become useful in characterization of textured surfaces. Pie *et al.* [20] introduced a deterministic numerical method, finite cell method (FCM), was proposed for the computation of multi- scale surface texture effects in the hydrodynamic regime. The results of presented method were compared with conventional FEM, CFD and existing theoretical and experimental data. Both computing time and storage required by FCM are significantly reduced, compared with FEM.

1.2.3 Piston ring and cylinder liner:

Mezghani *et al.* [21] developed a numerical model to investigate the effects of groove characteristics on the lubrication condition and friction at the interface between the piston ring and cylinder liner. This model was aimed at solving the average Reynolds equation, which depends on the real surface topographies of the cylinder liner, and described the influence of surface irregularities on the lubricant flow under hydrodynamic lubrication conditions, considering lubricant film rupture and cavitation.

1.2.4 Sliding surfaces:

Yuan *et al.* [22] designed and carried out experiments to study the orientation effects of grooves on the friction performance. The orientation of micro-grooves has a strong effect on the friction performance of sliding surfaces. The merits of perpendicular and parallel orientation may swap

under different contact conditions. Costa and Hutching [23] investigated the influence of surface topography on lubricant film thickness for the reciprocating sliding of patterned plane steel surfaces against cylindrical counter bodies under conditions of hydrodynamic lubrication. Pettersson and Jacobson [24] have shown that well-defined surface textures were produced by lithography and anisotropic etching of silicon wafers. The wafers were subsequently PVD coated retaining the substrate texture. The size and shape of the depressions were varied and evaluated in reciprocating slider under dry and boundary lubricated conditions. Vilhena *et al.* [25] established that specific textures on a tribological surface could contribute to friction reduction in sliding contacts. A pulsed Nd: YAG laser emitting at 1064 nm, was used against 100Cr6 steel samples in order to produce well-defined surface micro-pores, which can act as lubricant reservoirs, micro-hydrodynamic bearings as well as traps for wear debris. Wang *et al.* [26] found the optimum surface texture to improve the load carrying capacity of SiC bearings working in water. It was found that an optimum geometric and distributive range of micro-pits existed, where the load carrying capacity could be increased at least twice over that of a non-textured surface. Wang *et al.* [27] carried out experiments to verify if the low friction range of SiC in water lubrication can be expanded by micro-pores on the contact surface. Pores formed by laser, were distributed in a square array on the contact surface. The effect of the pore area ratio on friction coefficient and the critical load for the transition from hydrodynamic lubrication to mixed lubrication was reported.

1.2.5 Thrust bearing:

Wang *et al.* [28] carried out experiments to investigate the effect of dimple size on friction under line contact condition. The frictional tests of the brass disk sliding against a stationary cylindrical surface of bearing roller were conducted. It was found that the pattern with dimple diameter of 20 μm presented the effect of friction reduction.

1.2.6 Disc with magnetic textures:

Shen *et al.* [29] fabricated micro-scale dimple pattern firstly on the surface of tribo-pair and then a permanent magnet material was electrodeposited into these dimples, so that there are both geometric surface texture and periodic distribution of magnetic field on the surface (magnetic

surface texture). The test results showed that magnetic surface texture was conducive to form effective lubrication at low sliding velocity when lubricated by magnetic fluids.

1.2.7 Steel rings:

Qiu and Khonsari [30] conducted a series of experiments to examine the frictional characteristics of laser surface-textured, heat-treated 17-4 PH stainless steel specimens. Two dimple shapes were tested: circular and elliptical. The surface textured specimens provided low coefficient of friction compared with plain (dimple-free) surfaces.

1.2.8 Bearing sleeve surface:

Galda *et al.* [31] examined the use of a burnishing tool to give good surface characteristics such as surface topography having oil pockets. The proposed technique was very easy and allowed to obtain a deterministic surface on hard materials.

1.2.9 Study on dynamic characteristics:

Das *et al*. [32] presented the dynamic characteristics of hydrodynamic journal bearings lubricated with micro polar fluids. Roy and Laha [33] found the dynamic behavior of axial grooved journal bearings in terms of stiffness and damping coefficients of fluid film. Pai *et al*. [34] has been used a linearized perturbation approach to study the stability characteristics of tri-taper journal using the Reynolds boundary condition. Chetti [35] determined the dynamic characteristics in terms of stiffness, damping coefficients, the critical mass and whirl ratio for various values of size of material characteristic length and the coupling number for a four-lobe journal bearing lubricated with a micro polar fluid. Vijaya Kini *et al*. [36] found the stability characteristics of water lubricated journal bearings having three axial grooves theoretically.

1.3 Scope of the present work:

The following issues have been observed from the foregoing review of literature:

(i) The concept of textured surface bearing is relatively new and there are ample scopes to carry out theoretical as well as experimental studies.

(ii) When there are elaborate studies on effect of different types of texture on slider bearing, similar studies pertaining to hydrodynamic textured bearing are very limited.

(iii) Most of the studies are for specific geometry and therefore, generation of design data for such bearing still remains elusive. To address this issue, non-dimensional characterization of textured bearing has to be carried out.

(iv) Stability being a cause of concern for any hydrodynamic bearing, it would be pertinent to study stability of such bearing and to generate stability parameters.

In view of the above, an attempt has been made to carry out a non-dimensional analysis of textured bearing to generate design data which includes the following:

a. To estimate the steady-state performance characteristics of positive and negative textured journal bearing. Performance characteristics considered here are non-dimensional load capacity, flow coefficient and friction variable.
b. To estimate the dynamic coefficients of the textured journal bearings. Dynamic coefficients include two direct stiffness coefficients, two cross-coupled stiffness coefficients, two direct damping coefficients and two cross-coupled damping coefficients.
c. To study the stability characteristics by estimating stability parameters like mass parameter and whirl ratio.
d. To study the effect of different texture parameters like texture depth, texture density, partial texturing in circumferential and axial directions besides the effect of eccentricity ratio on the steady-state, dynamic and stability characteristics. In addition, the performance characteristics of textured bearing are compared with those of smooth journal bearing.

The study is limited to two types of texturing, viz., cylindrical texture and elliptical texture.

1.4 Organization of the thesis:

The present work deals with characterization of cylindrical and elliptical textured journal bearing. The present thesis is broadly divided into seven chapters. Chapter 1 deals with introduction and literature review. Mathematical formulation and the basic governing equations of textured journal bearing are provided in chapter 2. Chapter 3 deals with the steady-state performance characteristics of cylindrical textured journal bearing. Then, the steady-state performance characteristics of elliptical textured journal bearing are analyzed in chapter 4.

Chapter 5 deals with the analysis of dynamic characteristics and stability characteristics of positive cylindrical textured journal bearing. The analyses of dynamic and stability characteristics of positive elliptical textured journal bearing are provided in chapter 6. Different characteristics of cylindrical and elliptical textured journal bearing have been compared in chapter 7. Finally, the major inferences drawn from the work carried out in this thesis and future scope of work are produced in the same chapter.

1.5 Summary:

In this chapter, introduction to the surface roughness, history and literature are presented. It has been observed that there is ample scope to carry out research on textured journal bearing. In view of this the proposed objectives are carried out and presented in the following chapters.

CHAPTER 2

BASIC EQUATIONS AND OTHER FORMULATIONS

2.0 Introduction:

The basic equations of textured bearing are provided in this chapter. The governing equations of textured journal bearing are the Reynolds equation. The finite difference formulation of the journal bearing is presented in the following section. Further, a non-dimensional scheme for textured journal bearing has been presented here.

2.1 Numerical formulation:

2.1.1 Governing equation and boundary conditions:

In hydrodynamic lubrication problem, the governing equations can be expressed by the well-known Reynolds equation.

$$\frac{\partial}{\partial x}\left(h^3\frac{\partial p}{\partial x}\right)+\frac{\partial}{\partial z}\left(h^3\frac{\partial p}{\partial z}\right)=6\eta U\left(\frac{\partial h}{\partial x}\right) \qquad (2.1)$$

For non-dimensional solution, the substitutions are

$$x=R\theta,\ \ \bar{z}=\frac{z}{L/2},\quad \bar{h}=\frac{h}{C},\quad \bar{p}=\frac{pC^2}{6\eta UR}$$

Non Dimensional Reynolds equation becomes:

$$\frac{\partial}{\partial\theta}\left(\bar{h}^3\frac{\partial\bar{p}}{\partial\theta}\right)+\left(\frac{D}{L}\right)^2\frac{\partial}{\partial\bar{z}}\left(\bar{h}^3\frac{\partial\bar{p}}{\partial\bar{z}}\right)=\frac{\partial\bar{h}}{\partial\theta} \qquad (2.2)$$

The boundary conditions are $\bar{p}(\theta,0)=\bar{p}(\theta,L)=0$, $\bar{p}\left(\theta,\bar{z}\right)=\bar{p}\left(2\pi,\bar{z}\right)$

The boundary conditions shown above should be complemented by the conditions at the boundaries of possible cavitation regions associated with each individual dimple. The Reynolds boundary condition (also known as the Swift-Stieber boundary condition) implies that the pressure gradient with respect to the direction normal to the boundary of the cavitation zone is

zero and the dimensionless pressure inside the cavitation zone is also zero. Using an iterative solution, it is simple to apply this condition to the Reynolds Eq. (2.2). If negative, i.e., sub-ambient pressures are changed to zero in each iterative cycle, the process converges, by numerical diffusion, to the required Reynolds condition [37].

There are other boundary conditions used particularly for analysis of dynamic characteristics, like Kicinski, JFO etc., however, the present analysis uses Reynolds boundary conditions only. The reason behind using Reynolds boundary condition is that it is easy to implement in iterative solution methods, whereas other boundary conditions are difficult to implement. Further, there is no benchmark result based on the relatively new boundary conditions particularly for textured journal bearings to validate the present results. The validation in this work is also carried out for cylindrical textured bearing by comparing results based on Reynolds boundary conditions (chapter 3).

2.1.2 Film thickness equations:

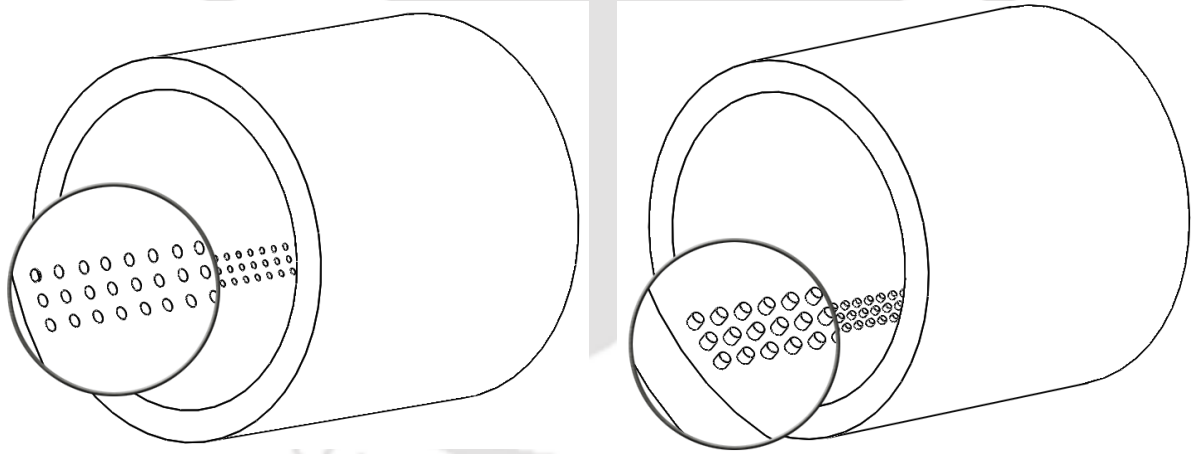

(a) (b)

Figure 2.1: Cylindrical textured journal bearing: (a) Outward dimples (negative) (b) Inward dimples (positive)

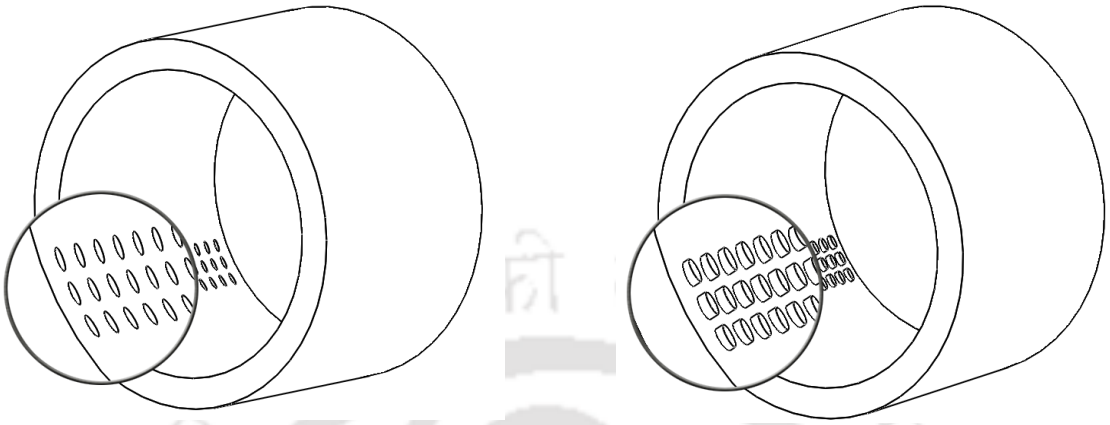

(a) (b)

Figure 2.2: Elliptical textured journal bearing: (a) Outside dimples (negative) (b) Inside dimples (positive)

Figures 2.1 and 2.2 depict cylindrical and elliptical textured journal bearings. Both positive and negative textured bearings are shown in the figures. The film thickness for textured journal bearing, *h*, can be written as follows:

$$h = h_{smooth}(\theta) \mp \Delta h(\theta, \bar{z}) \qquad (2.3)$$

The lubricant film thickness $h_{smooth} = C(1+\varepsilon\cos\theta)$ for smooth bearing (without textures) is dependent upon radial clearance *C*, eccentricity ratio ε and the angular coordinate θ. In the above equation $\Delta h(\theta, \bar{z})$ is the film thickness variation due to the textured surface.

For cylindrical textured bearings $\Delta\bar{h}$ is the non-dimensional texture depth. Non dimensional film thickness for positive and negative cylindrical texture can be written as

$$\left.\begin{aligned} \bar{h} &= 1+\varepsilon\cos\theta \mp \Delta\bar{h} \quad if\ \bar{x}_1^{\,2}+\bar{z}_1^{\,2} \le 1 \\ \bar{h} &= 1+\varepsilon\cos\theta \qquad\quad if\ \bar{x}_1^{\,2}+\bar{z}_1^{\,2} > 1 \end{aligned}\right\} \qquad (2.4)$$

For elliptical textured bearings texture depth is defined as $\Delta\bar{h} = \sqrt{\xi_1\xi_2}/\delta$, where ξ_1, ξ_2, δ are ratio of dimple height to length of longitudinal axis, ratio of dimple height to length of transverse axis and non-dimensional clearance. Non dimensional film thickness for positive and negative elliptical texture can be written as [38]

$$\left.\begin{aligned} \bar{h} &= 1+\varepsilon\cos\theta \mp \frac{\sqrt{\xi_1\xi_2}}{\delta} \quad if \quad \frac{\xi_1}{\xi_2}x_1^{\,2}+\frac{\xi_2}{\xi_1}y_1^{\,2} \le 1 \\ \bar{h} &= 1+\varepsilon\cos\theta \qquad\quad if \quad \frac{\xi_1}{\xi_2}x_1^{\,2}+\frac{\xi_2}{\xi_1}y_1^{\,2} > 1 \end{aligned}\right\} \qquad (2.5)$$

Further details are provided in chapters 3 and 4 for cylindrical and elliptical textured bearings.

2.1.3 Load carrying capacity:

Orthogonal components of non-dimensional load carrying capacity are given by Eqns. (2.6) and (2.7), when Eqn. (2.8) provides the non-dimensional load capacity of journal bearing.

$$\bar{W}_1 = -\int_0^1\int_0^{2\pi} \bar{p}\cos\theta\, d\theta d\bar{z} \qquad (2.6)$$

$$\bar{W}_2 = \int_0^1\int_0^{2\pi} \bar{p}\sin\theta\, d\theta d\bar{z} \qquad (2.7)$$

$$\bar{W} = \sqrt{\left(\int_0^1\int_0^{2\pi} \bar{p}\cos\theta\, d\theta d\bar{z}\right)^2 + \left(\int_0^1\int_0^{2\pi} \bar{p}\sin\theta\, d\theta d\bar{z}\right)^2} \qquad (2.8)$$

$$\phi = \tan^{-1}\left(\frac{\bar{W}_2}{\bar{W}_1}\right) \qquad (2.9)$$

2.1.4 Flow coefficient:

The dimensionless flow coefficient can be written as [39]

$$\bar{q}_z = \frac{1}{2}\left(\frac{D}{L}\right)^2 \int_0^{2\pi} \bar{h}^3 \frac{\partial \bar{p}}{\partial \bar{z}}\, d\theta \qquad (2.10)$$

2.1.5 Friction variable:

The friction variable can be written as [39]

$$\bar{\mu} = \mu\left(\frac{R}{C}\right) = \frac{\int_0^{2\pi}\left(3\bar{h}\left(\partial \bar{p} \big/ \partial\theta\right) + 1/\bar{h}\right) d\theta}{6\bar{W}} \qquad (2.11)$$

2.1.6 Dynamic coefficients:

The pressure and film thickness can be expressed for small amplitude of vibration as [39]

$$\left.\begin{aligned} \bar{p} &= \bar{p}_0 + \varepsilon_1 e^{i\tau}\bar{p}_1 + \varepsilon_0\phi_1 e^{i\tau}\bar{p}_2, \\ \bar{h} &= \bar{h}_0 + \varepsilon_1 e^{i\tau}\cos\theta + \varepsilon_0\phi_1 e^{i\tau}\sin\theta \end{aligned}\right\} \qquad (2.12)$$

The following three equations are obtained by substituting equation (2.12) into equation (2.1) and retaining the first order terms and equating the coefficients of $\varepsilon_0, \varepsilon_1 e^{i\tau}$ *and* $\varepsilon_0\phi_1 e^{i\tau}$

$$\frac{\partial}{\partial\theta}\left(\bar{h}_0^3 \frac{\partial \bar{p}_0}{\partial\theta}\right) + \left(\frac{D}{L}\right)^2 \frac{\partial}{\partial \bar{z}}\left(\bar{h}_0^3 \frac{\partial \bar{p}_0}{\partial \bar{z}}\right) = \frac{\partial \bar{h}_0}{\partial\theta} \qquad (2.13)$$

$$\left.\begin{aligned} &\frac{\partial}{\partial\theta}\left(\bar{h}_0^3 \frac{\partial \bar{p}_1}{\partial\theta}\right) + \left(\frac{D}{L}\right)^2 \frac{\partial}{\partial \bar{z}}\left(\bar{h}_0^3 \frac{\partial \bar{p}_1}{\partial \bar{z}}\right) + 3\frac{\partial}{\partial\theta}\left(\bar{h}_0^2 \frac{\partial \bar{p}_0}{\partial\theta}\cos\theta\right) \\ &+ \left(\frac{D}{L}\right)^2 \frac{\partial}{\partial \bar{z}}\left(\bar{h}_0^2 \frac{\partial \bar{p}_0}{\partial \bar{z}}\cos\theta\right) = -\sin\theta + i2\lambda\cos\theta \end{aligned}\right\} \qquad (2.14)$$

$$\left.\begin{aligned}&\frac{\partial}{\partial\theta}\left(\overline{h_0}^3\frac{\partial\overline{p_2}}{\partial\theta}\right)+\left(\frac{D}{L}\right)^2\frac{\partial}{\partial\bar{z}}\left(\overline{h_0}^3\frac{\partial\overline{p_2}}{\partial\bar{z}}\right)+3\frac{\partial}{\partial\theta}\left(\overline{h_0}^2\frac{\partial\overline{p_0}}{\partial\theta}\sin\theta\right)\\&+\left(\frac{D}{L}\right)^2\frac{\partial}{\partial\bar{z}}\left(\overline{h_0}^2\frac{\partial\overline{p_0}}{\partial\bar{z}}\sin\theta\right)=\cos\theta+i2\lambda\sin\theta\end{aligned}\right\} \qquad (2.15)$$

The stiffness and damping coefficients are given by [40]

$$\begin{aligned}\overline{K}_{rr}&=-\mathrm{Re}\left(\int_0^1\int_0^{2\pi}\overline{p}_1\cos\theta\,d\theta\,d\bar{z}\right)\\\overline{K}_{\phi r}&=-\mathrm{Re}\left(\int_0^1\int_0^{2\pi}\overline{p}_1\sin\theta\,d\theta\,d\bar{z}\right)\\\overline{D}_{rr}&=-\mathrm{Im}\frac{\left(\int_0^1\int_0^{2\pi}\overline{p}_1\cos\theta\,d\theta\,d\bar{z}\right)}{\lambda}\\\overline{D}_{\phi r}&=-\mathrm{Im}\frac{\left(\int_0^1\int_0^{2\pi}\overline{p}_1\sin\theta\,d\theta\,d\bar{z}\right)}{\lambda}\\\overline{K}_{\phi\phi}&=-\mathrm{Re}\left(\int_0^1\int_0^{2\pi}\overline{p}_2\sin\theta\,d\theta\,d\bar{z}\right)\\\overline{K}_{r\phi}&=-\mathrm{Re}\left(\int_0^1\int_0^{2\pi}\overline{p}_2\cos\theta\,d\theta\,d\bar{z}\right)\\\overline{D}_{\phi\phi}&=-\mathrm{Im}\frac{\left(\int_0^1\int_0^{2\pi}\overline{p}_2\sin\theta\,d\theta\,d\bar{z}\right)}{\lambda}\\\overline{D}_{r\phi}&=-\mathrm{Im}\frac{\left(\int_0^1\int_0^{2\pi}\overline{p}_2\cos\theta\,d\theta\,d\bar{z}\right)}{\lambda}\end{aligned} \qquad (2.16)$$

2.1.7 Stability analysis:

Self-excited vibration of the rotor due to fluid film force is known as oil whirl; the frequency of this vibration is about $\frac{\omega}{2}$, where ω is the rotational speed of the rotor. Considering a rotor of mass 2m supported by two bearings. The non-dimensional liberalized equations of journal motion can be written as follows.

$$\overline{M}\Delta\ddot{\bar{x}} + \overline{K}_{XX}\Delta\bar{x} + \overline{K}_{XZ}\Delta\bar{z} + \overline{C}_{XX}\Delta\dot{\bar{x}} + +\overline{C}_{XX}\Delta\dot{\bar{z}} = 0 \qquad (2.17)$$

$$\overline{M}\Delta\ddot{\bar{z}} + \overline{K}_{ZX}\Delta\bar{x} + \overline{K}_{ZZ}\Delta\bar{z} + \overline{C}_{ZX}\Delta\dot{\bar{x}} + +\overline{C}_{ZZ}\Delta\dot{\bar{z}} = 0 \qquad (2.18)$$

Where $\overline{M} = \dfrac{mC\omega^2}{W}$, a non-dimensional mass parameter.

The steady state equilibrium position of the journal is x_0, z_0 and Δx and Δz are the perturbed amount from the steady state position at time‘t’. Therefore, the following expressions are arrived at.

$$\left.\begin{aligned} &\bar{x} = \bar{x}_0 e^{i\lambda\tau},\ \bar{z} = \bar{z}_0 e^{i\lambda\tau} \\ &\dot{\bar{x}} = i\lambda\bar{x}_0 e^{i\lambda\tau},\ \dot{\bar{z}} = i\lambda\bar{z}_0 e^{i\lambda\tau} \\ &\ddot{\bar{x}} = -\lambda^2\bar{x}_0 e^{i\lambda\tau},\ \ddot{\bar{z}} = -\lambda^2\bar{z}_0 e^{i\lambda\tau} \end{aligned}\right\} \qquad (2.19)$$

Substituting the expressions of Eqn.2.19, the equations of motion (Eqns.2.17 and 2.18), a characteristic equation is formed as show in Eqn 2.20:

$$\begin{bmatrix} -\lambda^2\overline{M} + i\lambda\overline{C}_{XX} + K_{XX} & \overline{K}_{XZ} + i\lambda\overline{C}_{XZ} \\ \overline{K}_{ZX} + i\lambda\overline{C}_{ZX} & -\lambda^2 M + i\lambda\overline{C}_{ZZ} + \overline{K}_{ZZ} \end{bmatrix} \begin{Bmatrix} \bar{x}_0 \\ \bar{z}_0 \end{Bmatrix} e^{i\lambda\tau} = \begin{Bmatrix} 0 \\ 0 \end{Bmatrix} \qquad (2.20)$$

Solving the characteristic equation, the following expressions for the mass parameter, $\overline{M}$ and the whirl ratio, λ are arrived at:

$$\lambda^2\overline{M} = \frac{\overline{K}_{XX}\overline{C}_{ZZ} + \overline{K}_{ZZ}\overline{C}_{XX} - (\overline{K}_{XZ}\overline{C}_{ZX} + \overline{K}_{ZX}\overline{C}_{XZ})}{\overline{C}_{XX} + \overline{C}_{ZZ}} = k_0 \qquad (2.21)$$

So, $\lambda^2 = \dfrac{(\overline{K}_{XX} - k_0)(\overline{K}_{ZZ} - k_0) - \overline{K}_{XZ}\overline{K}_{ZX}}{\overline{C}_{XX}\overline{C}_{ZZ} - \overline{C}_{XZ}\overline{C}_{ZX}}$ and $\overline{M} = \dfrac{k_0}{\lambda^2}$ (2.22)

For a chosen static equilibrium position, the values of dynamic coefficients are determined. These values are used to calculate the value of $\overline{M}$ and λ . When the mass parameter

of a rotor bearing system exceeds the value calculated by the above method, the instability occurs in the system. The value of mass parameter at the threshold of instability is known as the critical mass parameter $(\overline{M}_{crit})$ and corresponding whirl ratio is known as critical whirl ratio (λ_{crit}).

2.1.8 Stability parameters:

Stiffness and damping coefficients are used in the equations of motion to obtain the following equations for getting non-dimensional mass parameter:

$$\overline{M} = \frac{1}{\lambda^2\left(\overline{D}_{\phi\phi} + \overline{D}_{rr}\right)}\left[\begin{array}{c}\left(\overline{K}_{rr}\overline{D}_{\phi\phi} + \overline{D}_{rr}\overline{K}_{\phi\phi}\right) - \left(\overline{K}_{\phi r}\overline{D}_{r\phi} + \overline{D}_{\phi r}\overline{K}_{r\phi}\right) \\ + \frac{\overline{W}}{\varepsilon_0}\left(\overline{D}_{rr}\cos\phi_0 - \overline{D}_{\phi r}\sin\phi_0\right)\end{array}\right] \qquad (2.23)$$

$$\overline{M}^2\lambda^4 - \lambda^2\left[\overline{M}\left(\frac{\overline{W}\cos\phi_0}{\varepsilon_0} + \overline{K}_{\phi\phi} + \overline{K}_{rr}\right) + \left(\overline{D}_{rr}\overline{D}_{\phi\phi} - \overline{D}_{\phi r}\overline{D}_{r\phi}\right)\right]$$
$$+\left(\overline{K}_{rr}\overline{K}_{\phi\phi} - \overline{K}_{\phi r}\overline{K}_{r\phi}\right) + \frac{\overline{W}}{\varepsilon_0}\left(\overline{K}_{rr}\cos\phi_0 - \overline{K}_{\phi r}\sin\phi_0\right) = 0 \qquad (2.24)$$

Equations (2.23) and (2.24) are linear algebraic equations in $\overline{M}$ and λ. Solution of these will give $\overline{M}$ and λ.

2.1.9 Solution scheme:

Equation (2.2) has been solved numerically in a finite difference grid. Gauss-Siedel method with over relaxation has been used for solving the discretized Reynolds equation satisfying the boundary conditions. As the dimples are very small, it has been observed that finite difference grid needs to be very fine for convergence. A grid size of 350 x 50 in the present work has been found to give grid-independent pressure distribution.

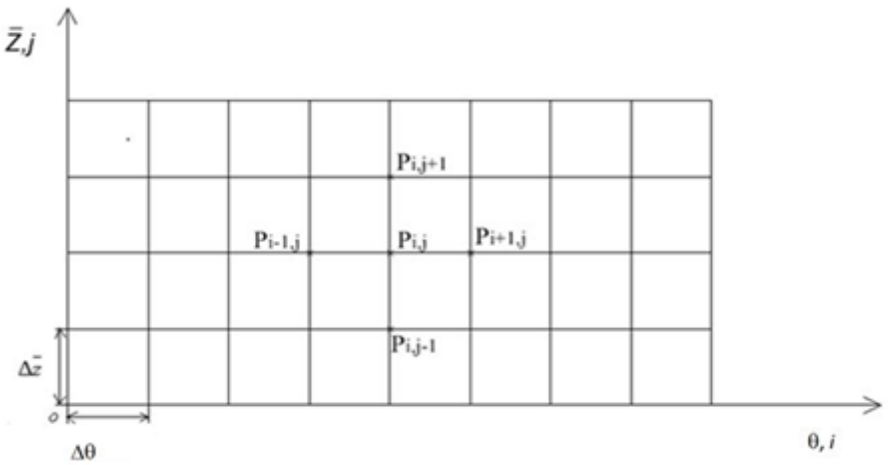

Fig: 2.3 A developed view of a bearing showing the meshes of size $\left(\Delta\theta \times \Delta\bar{Z}\right)$

$P_{i,j}$ = Pressure at any point (i, j)

Now using central difference approach

$$\frac{\partial \bar{P}}{\partial \theta} = \frac{\bar{P}_{i+1,j} - \bar{P}_{i-1,j}}{2(\Delta\theta)}$$

$$\frac{\partial \bar{P}}{\partial \theta^2} = \frac{\bar{P}_{i+1,j} - 2\bar{P}_{i,j} + \bar{P}_{i-1,j}}{(\Delta\theta)^2}$$

$$\frac{\partial P}{\partial Z} = \frac{P_{i,j+1} - P_{i,j-1}}{2(\Delta\bar{Z})}$$

$$\frac{\partial \bar{P}}{\partial \bar{Z}^2} = \frac{\bar{P}_{i,j+1} - 2\bar{P}_{i,j} + \bar{P}_{i,j-1}}{(\Delta\bar{Z})^2}$$

$$\bar{P}_{i,j} = \frac{C1 + C2 + C3 + C4}{C5} \qquad (2.25)$$

It is seen that the pressure at any point (i, j) is expressed in terms of pressure of four adjacent points. The non-dimensional pressure $\overline{P}_{i,j}$ at all mesh points are assumed to be zero to start with the iteration process. Gauss-Seidel method has been used for solving the equations of pressure at each node satisfying the boundary conditions. The method has been described briefly as follows.

The error at point (i, j) is

$$Error = R.H.S \text{ of equation (2.25)} - \overline{P}_{i,j} \qquad (2.26)$$

The new pressure can be calculated using a successive over relaxation scheme (SOR) as

$$\left(\overline{P}_{i,j}\right)_{new} = \left(\overline{P}_{i,j}\right)_{old} + \left(error\right)_{i,j} \times orf \qquad (2.27)$$

Where orf is the over relaxation factor. It accelerates the convergence of the numerical process. The pressure convergence condition used is $\left|\frac{\Sigma\left(\overline{P}^{old}_{i,j} - \overline{P}^{new}_{i,j}\right)}{\Sigma\overline{P}^{new}_{i,j}}\right| \le 0.0001.$

After carrying out linear perturbation of the unsteady Reynolds equation, one arrives at Eqns. (2.13), (2.14) and (2.15). Eqn. (2.13) is the same as Eqn. (2.2), whereas Eqns. (2.14) and (2.15) are perturbed equations and these are solved following the same procedure as explained above. The perturbed pressures are then utilized to estimate the dynamic coefficients as given in Eqn (2.16). The stability parameters, namely, mass parameter and whirl ratio are estimated utilizing the dynamic coefficients in Eqns. (2.23) and (2.24).

2.2 Summary:

In the present chapter, the basic formulations are provided. The governing equation for journal bearing, i.e., Reynolds equation is non-dimensionalized; the film thickness equations for cylindrical and elliptical bearings and boundary conditions are presented. Further, the expressions for three performance parameters are presented, linear perturbation of Reynolds equation is carried out to estimate the dynamic coefficients followed by equations for estimation of stability parameters are provided. The solution scheme has been explained at the end.

CHAPTER 3

CYLINDRICAL TEXTURED JOURNAL BEARING

3.0 Introduction:

A theoretical analysis has been carried out to study the steady-state performance characteristics of cylindrical textured journal bearing in this chapter. Performance characteristics are load carrying capacity, flow and friction variable. For validation, the present results are compared with available results. The effects of different parameters like texture depth, texture portion in circumferential and axial directions, and eccentricity ratio on the performance characteristics are analyzed.

3.1 Cylindrical texture:

It is possible to texture either sides of the bearing surface as shown in Fig. 3.1. The figure has been reproduced from chapter 2 for ease of reference. If texturing produces asperities on the surface is considered as positive texturing, the dimples produced on inside the surface may be termed as negative texturing. The negative type of texturing can be produced by laser surface texturing, when positive type can be produced by sputtering, photolithography. It has been observed that performance characteristics of hydrodynamic journal bearing with negative cylindrical textured area were estimated [1]. However, characterization of bearings with positive cylindrical textured surface has not been reported. The present work aims to find the performance characteristics of positive cylindrical textured journal bearing, i.e. the effect of texturing on performance characteristics like load capacity, flow coefficient and friction variable. The results presented are in non-dimensional form which enables one to utilize them for a wide range of operating parameters.

The distribution of texture on the bearing surface in both the cases has been shown in Fig. 3.2. The geometry of cylindrical texture has been shown in Fig. 3.3 in an imaginary square cell containing one cylindrical texture. The texture distribution is uniform as shown in Figure 3.2. When r_p represents the radius of cylindrical dimple, $2r_1$ is the length of the imaginary square cell as shown in the figure.

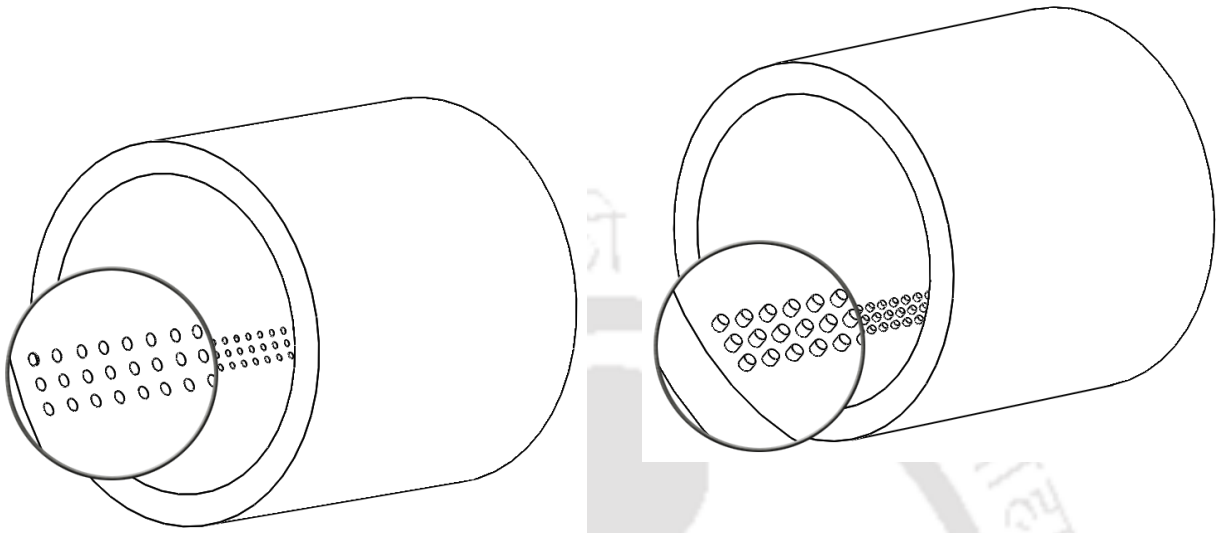

(a) (b)

Figure 3.1: Cylindrical textured journal bearing: (a) Outward dimples (negative)

(b) Inward dimples (positive)

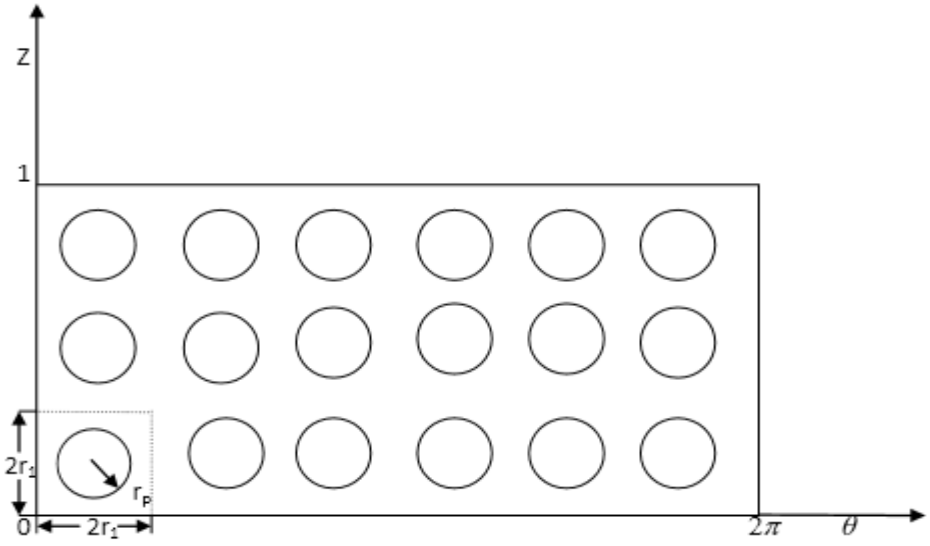

Figure 3.2: Distribution of textures on the bearing surface

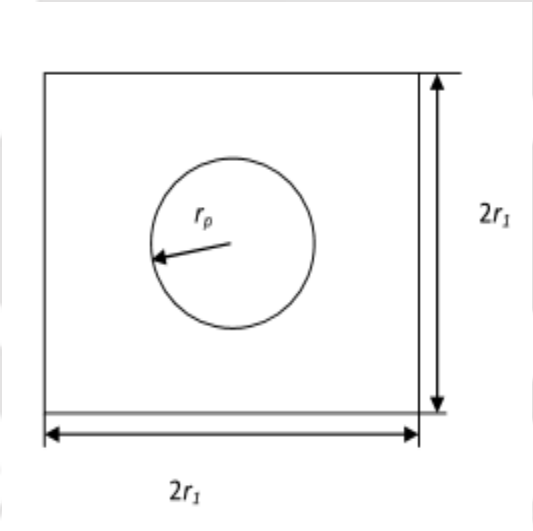

Figure 3.3: Geometry of cylindrical texture

3.1.1 Numerical formulation

In hydrodynamic lubrication problem, the governing equations can be expressed by the well-known Reynolds equation [27].

$$\frac{\partial}{\partial x}\left(h^3\frac{\partial p}{\partial x}\right)+\frac{\partial}{\partial z}\left(h^3\frac{\partial p}{\partial z}\right)=6\eta U\left(\frac{\partial h}{\partial x}\right) \qquad (3.1)$$

For non-dimensional solution, the substitutions are

$$x=R\theta,\quad \bar{z}=\frac{z}{L/2},\quad \bar{h}=\frac{h}{C},\quad \bar{p}=\frac{pC^2}{6\eta UR} \qquad (3.2)$$

Non Dimensional Reynolds equation becomes:

$$\frac{\partial}{\partial\theta}\left(\bar{h}^3\frac{\partial\bar{p}}{\partial\theta}\right)+\left(\frac{D}{L}\right)^2\frac{\partial}{\partial\bar{z}}\left(\bar{h}^3\frac{\partial\bar{p}}{\partial\bar{z}}\right)=\frac{\partial\bar{h}}{\partial\theta} \qquad (3.3)$$

The film thickness for textured journal bearing, *h*, can be written as follows:

$$h=h_{smooth}(\theta)+\Delta h(\theta,z) \qquad (3.4a)$$
$$h=h_{smooth}(\theta)-\Delta h(\theta,z) \qquad (3.4b)$$

The lubricant film thickness $h_{smooth}=C(1+\varepsilon\cos\theta)$ for smooth bearing (without textures) is dependent upon radial clearance *C*, eccentricity ratio ε and the angular coordinate θ. In the above equation $\Delta h(\theta,z)$ is the film thickness variation due to the textured surface.

Film thickness equations are provided in [1]. These equations are converted to non dimensional form as

$$\left.\begin{aligned}\bar{h}&=1+\varepsilon\cos\theta\pm\overline{\Delta h} \quad if\ \bar{x}_1^{\,2}+\bar{z}_1^{\,2}\le 1\\ \bar{h}&=1+\varepsilon\cos\theta \quad if\ \bar{x}_1^{\,2}+\bar{z}_1^{\,2}>1\end{aligned}\right\} \qquad (3.5)$$

$\bar{x}_1$ and $\bar{z}_1$ are the non-dimensional local coordinates. Film thickness at the textured location is determined using the first equation, whereas the second equation gives the film thickness of un-textured location.

The boundary conditions are $\bar{p}(\theta,0) = \bar{p}(\theta,L) = 0$, $\bar{p}\left(0,\bar{z}\right) = \bar{p}\left(2\pi,\bar{z}\right)$

The boundary conditions shown above should be complemented by the conditions at the boundaries of possible cavitation regions associated with each individual dimple. The Reynolds boundary condition (also known as the Swift-Stieber boundary condition) implies that the pressure gradient with respect to the direction normal to the boundary of the cavitation zone is zero and the dimensionless pressure inside the cavitation zone is also zero. Using an iterative solution, it is simple to apply this condition to the Reynolds Eq. (3.3). If negative, i.e., sub-ambient pressures are changed to zero in each iterative cycle, the process converges, by numerical diffusion, to the required Reynolds condition [37].

Equation (3.3) has been solved numerically in a finite difference grid. Gauss-Siedel method with over relaxation has been used for solving the discretized Reynolds equation satisfying the boundary conditions. As the dimples or asperities are very small, it has been observed that finite difference grid needs to be very fine for convergence. Grids in increasing orders have been tried and the pressure distributions have been compared until it has been found that the results remain the same even if the grid size is increased. In this way, a grid size of 350 x 50 in the present work has been found to give grid-independent pressure distribution.

3.2 Validation

The present results are non-dimensional; however, non-dimensional analysis of micro-cylindrical textured bearing is not available. Therefore, to validate the code developed, it is proposed to take the operating conditions of Tala-Ighil *et.al*. [1], to compare the present results with those in Tala-Ighil *et.al.* [1]. The numerical results on performance characteristics of journal bearing are generated for the journal bearing length to diameter ratio, 1.0 and then the results are converted to dimensional form using the operating conditions mentioned below.

Operating conditions of journal bearing

Shaft speed ω = 625.4 rad/s

Shaft radius R = 0.0315m.

Bearing length L = 0.063m.

Radial clearance C = 0.00003m.

Lubricant viscosity η = 0.0035Pas.

Table 3.1: Comparison of present results with available results for negative textured journal bearing

Case	θ	$\overline{Z}$	$h_{\min}(\mu m)$ (Ref [1])	$Q\times10^{-5}\ m^3/s$ (Ref [1])	ϕ (Ref[1])	$P_{\max}(MPa)$ (Ref [1])	θ_m (Ref[1])
1	Non-texture	Non-texture	11.61 (11.97)	1.67 (1.743)	50.1 (50.5)	7.81 (7.71)	148.0 (148.0)
2	0-360	0-1	8.22 (8.71)	1.55 (1.422)	45.7 (46.1)	7.76 (8.26)	152.0 (152.5)

Table 3.1 presents the comparison of negative texture results $(h_{\min}, Q, \phi, P_{\max}, \theta_m)$ with those of [1]. Two cases have been considered here. In case 1, un-textured surface is considered in both the directions, when in case 2, full texturing has been taken in θ direction and $\overline{Z}$ direction. In this load capacity has been kept constant and minimum film thickness is varied. A fairly good agreement has been observed while comparing the present results with those of [1]. Therefore, the present code is used to estimate the non-dimensional performance characteristics of cylindrical textured bearing.

Variation of friction variable with Sommerfeld number of cylindrical textured journal bearing is presented in Fig.3.4 for L/D = 1, ε = 0.6, S_p = 0.6, α = 1, β = 1. Since friction variable has been increasing linearly with increase in Sommerfeld number, therefore, it is beyond doubt that the bearing operates in the hydrodynamic lubrication regime.

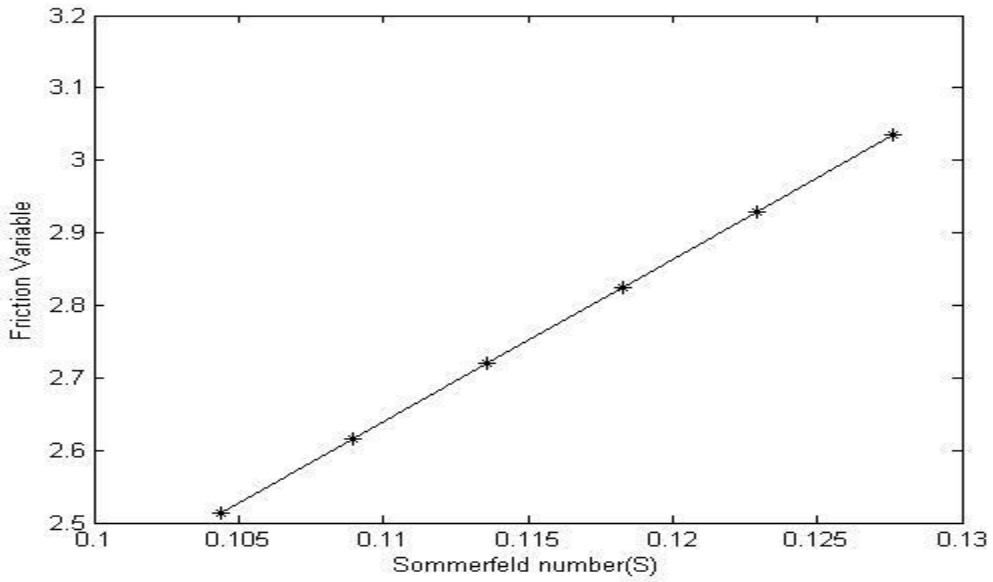

Figure 3.4: Variation of friction variable with sommerfeld number of cylindrical textured journal bearing ($L/D = 1,\ \varepsilon = 0.6,\ S_p = 0.6,\ \alpha = 1,\ \beta = 1$)

3.3 Results and discussions:

3.3.1 Positive cylindrical texture:

3.3.1.1 Effect of texture depth:

Load carrying capacity, flow coefficient and friction variable of positive cylindrical textured journal bearing are plotted against textured depth in Figs. 3.5 to 3.7 respectively for $L/D = 1$, $S_p = 0.6,\ \alpha = 1,\ \beta = 1$. Non dimensional texture depth is varied from 0 to 0.06. It is observed that the load carrying capacity increases slightly with increase in texture depth for $\varepsilon = 0.8$ only, when it remains more or less same for other eccentricity ratios considered as seen in Fig. 3.5. Flow coefficient increases little with the increase in texture depth for all the eccentricity ratios considered as has been seen in fig. 3.6. Figure 3.7 shows that there is no effect of texture depth on friction variable as it remains almost constant for the range of texture depth considered.

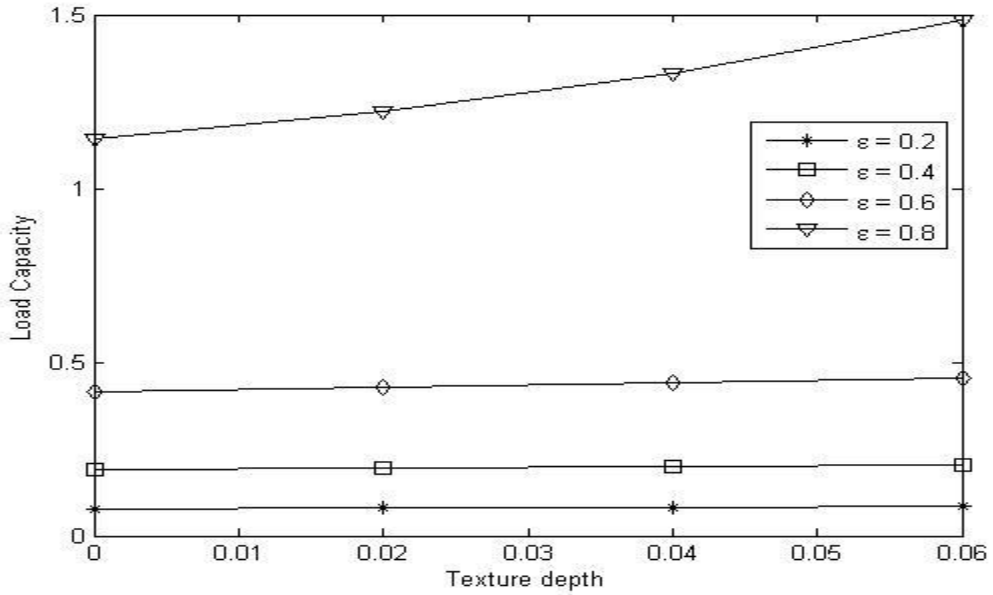

Figure 3.5: Variation of load carrying capacity with texture depth

$(L/D = 1,\ S_p = 0.6,\ \alpha = 1,\ \beta = 1)$

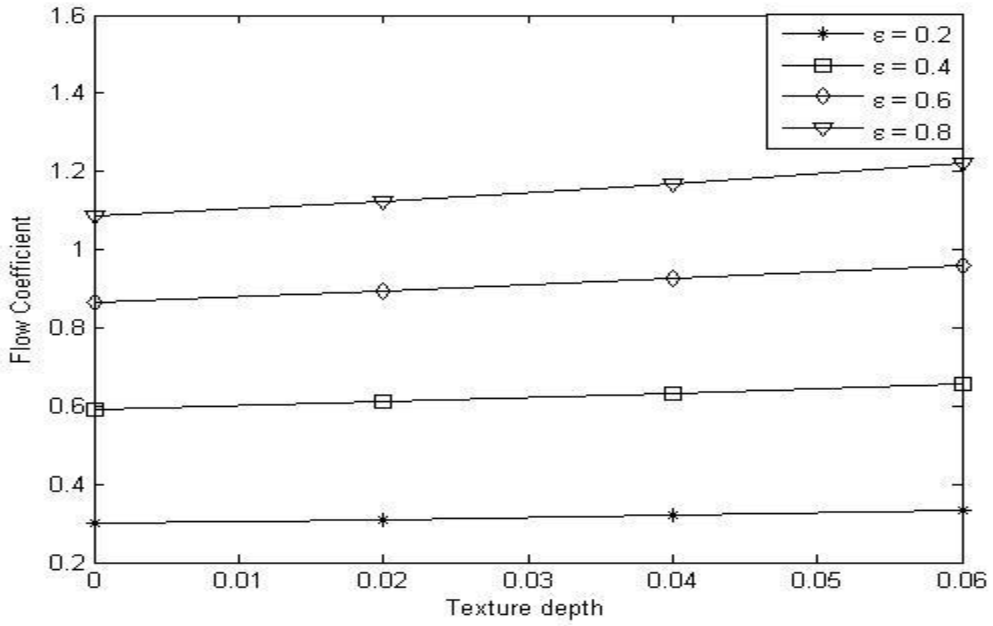

Figure 3.6: Variation of flow coefficient with texture depth

$(L/D = 1,\ S_p = 0.6,\ \alpha = 1,\ \beta = 1)$

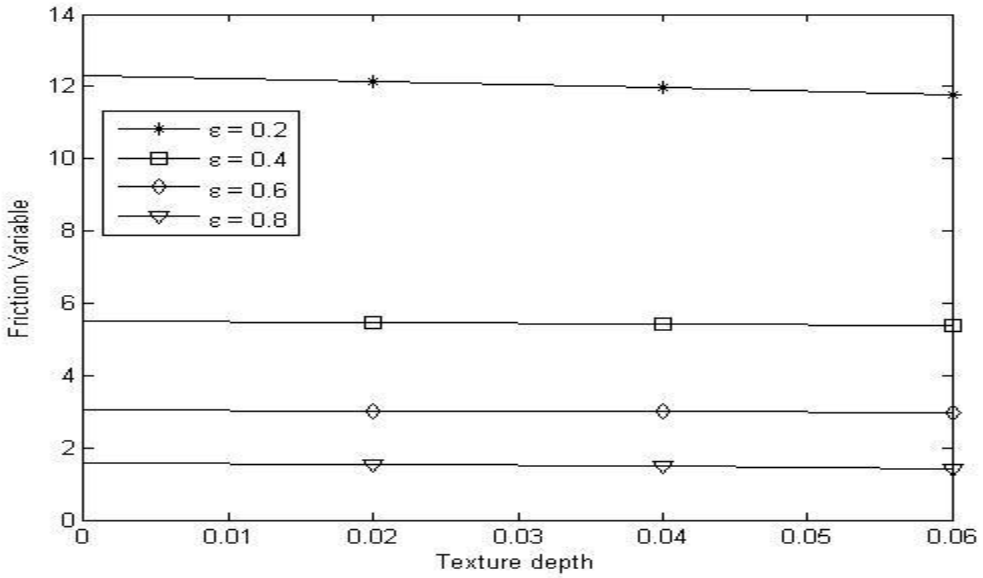

Figure 3.7: Variation of friction variable with texture depth

$(L/D = 1,\ S_p = 0.6,\ \alpha = 1,\ \beta = 1)$

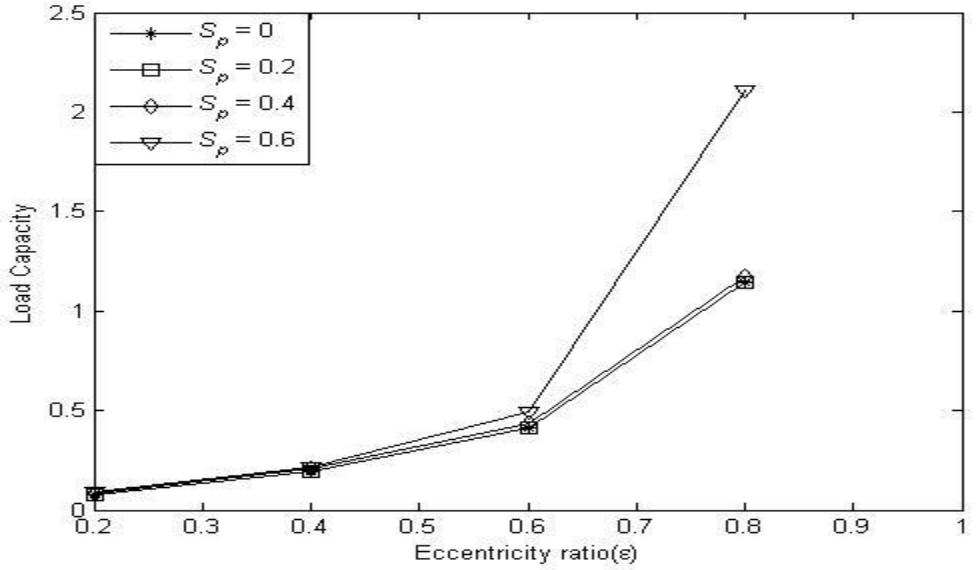

Figure 3.8: Variation of load carrying capacity with eccentricity ratio of textured journal bearing

$(L/D = 1,\ \Delta\bar{h} = 0.1,\ \alpha = 1,\ \beta = 1)$

3.3.1.2 Effect of eccentricity ratio and textured area density

Figure 3.8 represents variation of load carrying capacity with eccentricity ratio of cylindrical textured bearing for $L/D = 1$, $\Delta\bar{h} = 0.1$, $\alpha = 1$, $\beta = 1$ and textured area density 0, 0.2, 0.4, 0.6. Eccentricity ratio is varied from 0.2 to 0.8. The load carrying capacity is observed to be increasing with increase in eccentricity ratio for all values of textured area density. However, the effect of textured area density has been observed only at higher eccentricity ratios, i.e., load carrying capacity increases with increase in textured area density.

Figure 3.9 represents variation of flow coefficient with eccentricity ratio of cylindrical textured bearing for $L/D = 1$, $\Delta\bar{h} = 0.1$, $\alpha = 1$, $\beta = 1$ and textured area density 0, 0.2, 0.4, 0.6. Flow coefficient increases with increase in eccentricity ratio. Besides effect of textured area density is also observed to be significant, i.e., flow coefficient increases with increase in texture area density for the range of eccentricity ratio considered.

Figure 3.10 represents variation of friction variable with the variation of eccentricity ratio of the textured journal bearing for $L/D = 1$, $\Delta\bar{h} = 0.1$, $\alpha = 1$, $\beta = 1$ and textured area density 0, 0.2, 0.4, 0.6... Eccentricity ratio is varied from 0.2 to 0.8. It has been observed that friction variable decreases with increase in eccentricity ratio of journal bearing. There is a minimal effect of textured area density on friction variable as it slightly decreases with increase in textured area density.

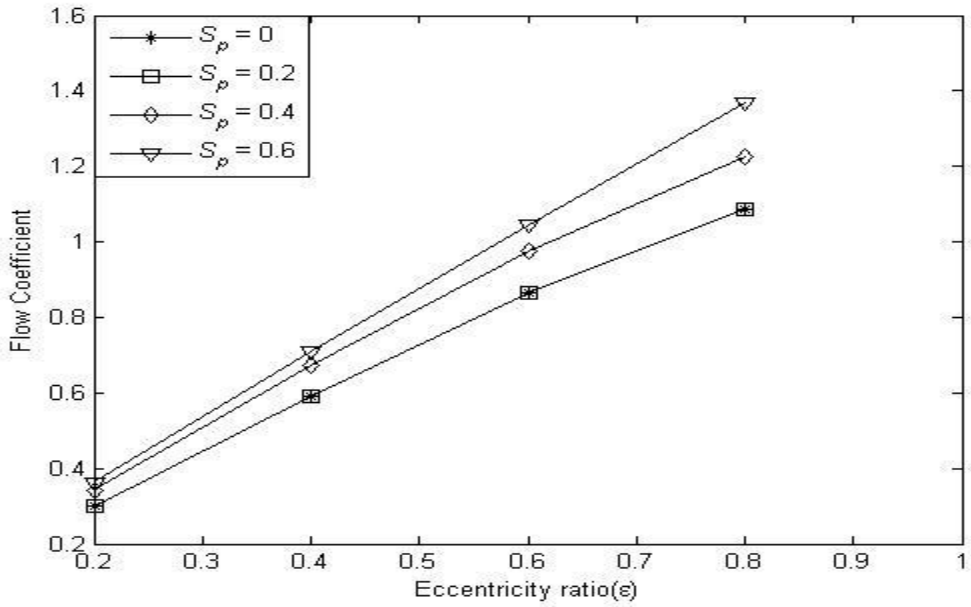

Figure 3.9: Variation of flow coefficient with eccentricity ratio of textured journal bearing

$(L/D = 1,\ \Delta\bar{h} = 0.1,\ \alpha = 1,\ \beta = 1)$

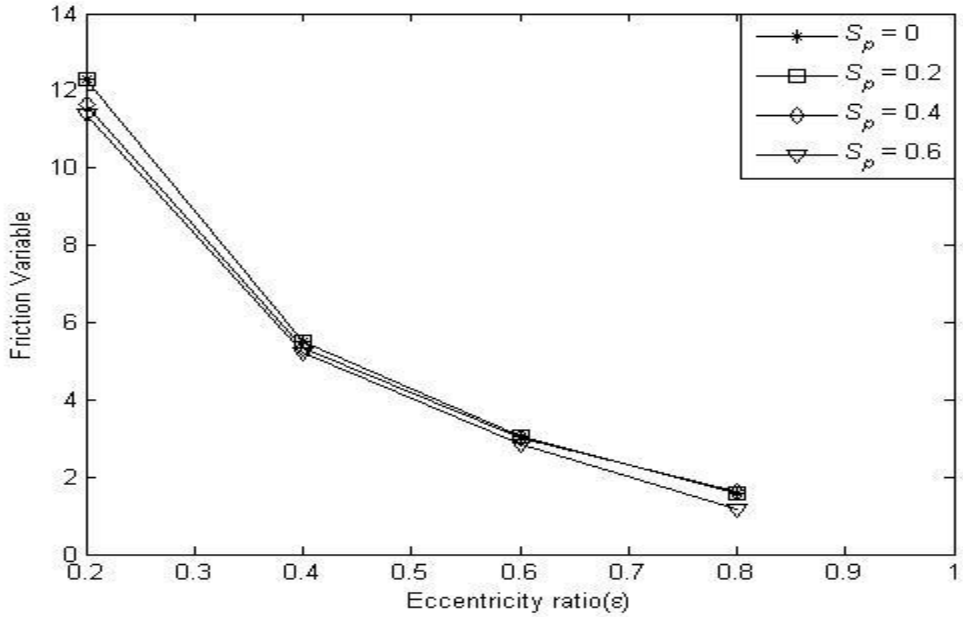

Figure 3.10: Variation of friction variable with eccentricity ratio of textured journal bearing

$(L/D = 1,\ \Delta\bar{h} = 0.1,\ \alpha = 1,\ \beta = 1)$

3.3.1.3 Effect of textured portion in circumferential direction:

Load carrying capacity, flow coefficient and friction variable are plotted against textured portion in circumferential direction in Figs. 3.11 to 3.13 respectively for. Eccentricity ratio taken is 0.2 to 0.8, Texture area density is 0.6 and dimensionless dimple height is 0.1. Full texture has been taken in axial direction and textured portion is varied in circumferential direction. Effect of textured portion on load capacity has been observed only for eccentricity ratio 0.8. Load carrying capacities at other eccentricity ratios considered are found to be more or less constant over un-textured to fully textured condition. However, load carrying capacity increases sharply from 40% to 60 % textured portion in circumferential direction and then remains constant up to fully textured condition for eccentricity ratio 0.8. Influence of textured portion in circumferential direction on flow coefficient is observed to be not very significant. There is a little increase in flow coefficient with increase in textured portion in circumferential direction up to 60 % which gradually increases with increase in eccentricity ratio. However, it remains the same beyond 60% textured portion in circumferential direction. On the other hand friction variable varies little at eccentricity ratios 0.4, 0.6 and 0.8; whereas it reduces initially up to 40% textured portion in circumferential direction for eccentricity ratio 0.2. As a whole, it may be inferred that performance of positive cylindrical textured journal bearing is not much influenced by partial texturing.

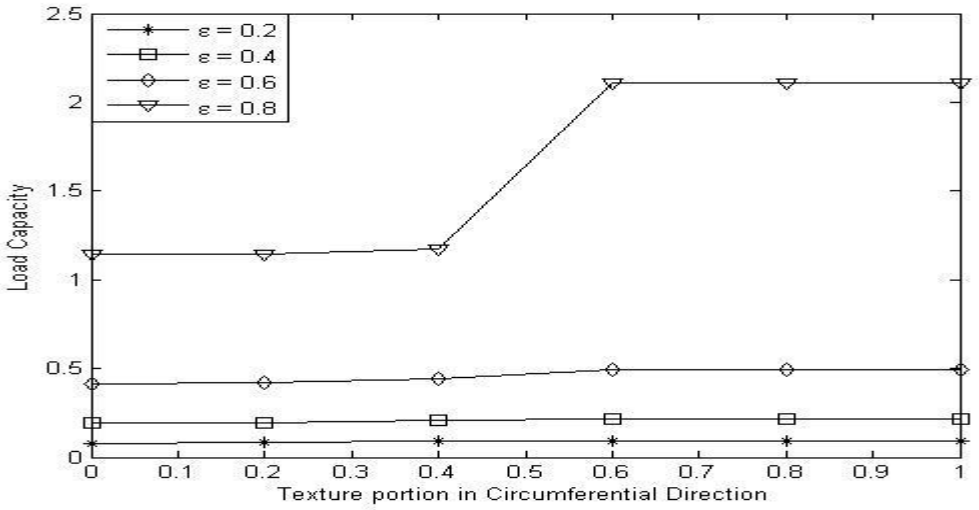

Figure 3.11: Effect of textured portion in circumferential direction on load carrying capacity of textured journal bearing ($L/D = 1,\ S_p = 0.6,\ \Delta\bar{h} = 0.1,\ \beta = 1$)

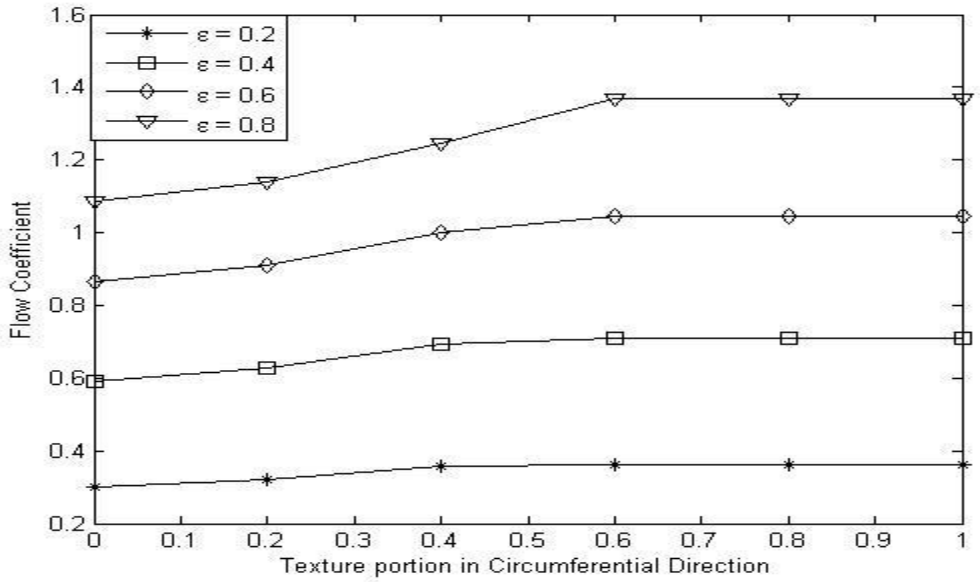

Figure 3.12: Effect of textured portion in circumferential direction on flow coefficient of textured journal bearing ($L/D = 1,\ S_p = 0.6,\ \Delta\bar{h} = 0.1,\ \beta = 1$)

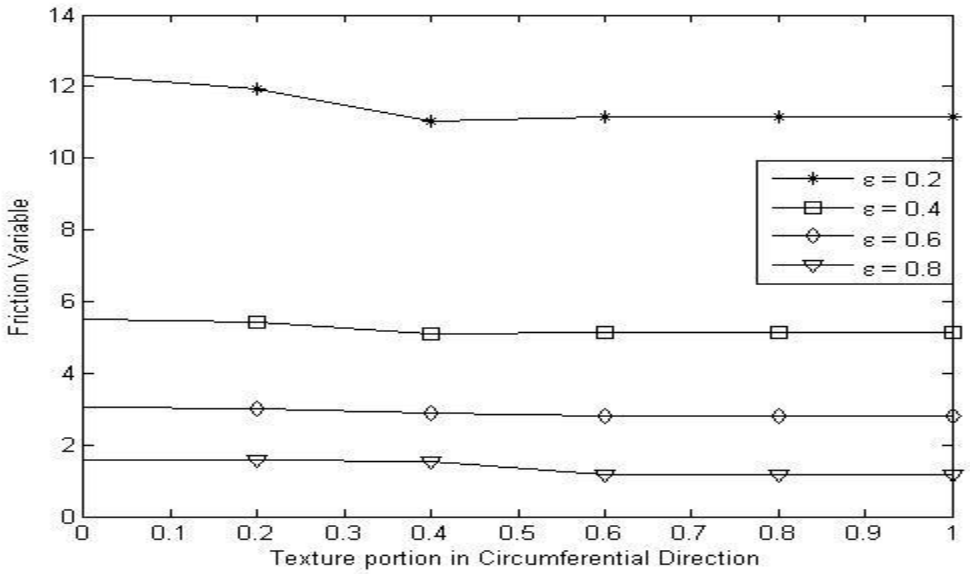

Figure 3.13: Effect of textured portion in circumferential direction friction variable of textured journal bearing ($L/D = 1,\ S_p = 0.6,\ \Delta\bar{h} = 0.1,\ \beta = 1$)

3.3.1.4 Effect of textured portion in axial direction:

Load carrying capacity, flow coefficient and friction variable are plotted against textured portion in axial direction in Figs. 3.14 to 3.16 respectively. Eccentricity ratio taken is 0.2 to 0.8, texture area density is 0.6 and dimensionless dimple height is 0.1. Full texture has been taken in circumferential direction and textured portion is varied in axial direction. It has been observed that load carrying capacity remains more or less at eccentricity ratio other than 0.8. There is a steady rise in load carrying capacity from 20% textured portion to fully textured condition as seen from Fig. 3.14. Flow coefficient increases slightly for all eccentricity ratios considered from un-textured to fully textured condition, when the increment is gradually more with increase in eccentricity ratios as depicted in Fig. 3.15. Friction variable decreases nominally with increase in textured portion in axial direction for all the eccentricity ratios considered. However, the decrease is more prominent at eccentricity ratio 0.2 as has been observed from Fig. 3.16. The effect of textured portion in axial direction on the performance of positive cylindrical textured

journal bearing is found to be much more prominent compared to the effect of textured portion in circumferential direction as has been seen from the presented results.

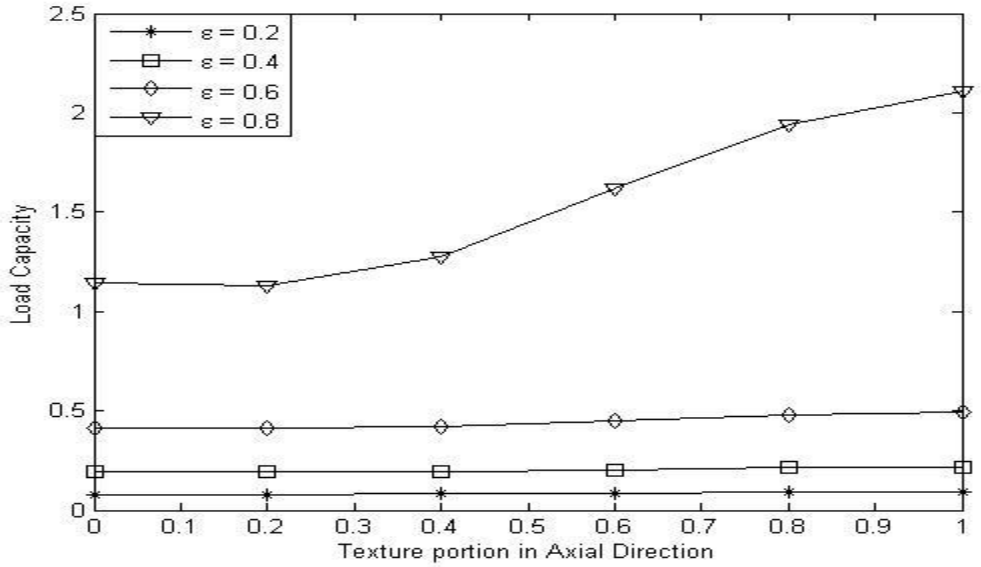

Figure 3.14: Effect of textured portion in axial direction on Load carrying capacity of textured journal bearing ($L/D = 1,\ S_p = 0.6,\ \Delta\bar{h} = 0.1,\ \alpha = 1$)

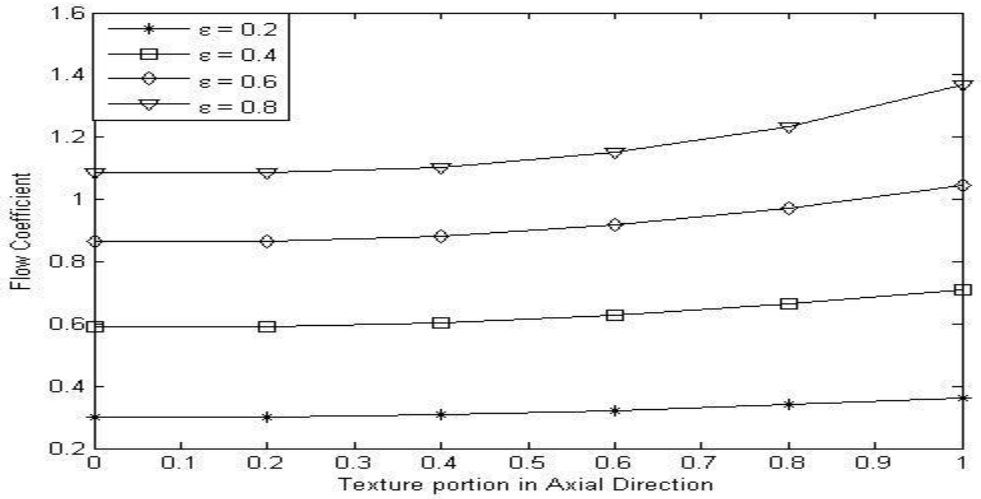

Figure 3.15: Effect of textured portion in axial direction on flow coefficient of textured journal bearing ($L/D = 1,\ S_p = 0.6,\ \Delta\bar{h} = 0.1,\ \alpha = 1$)

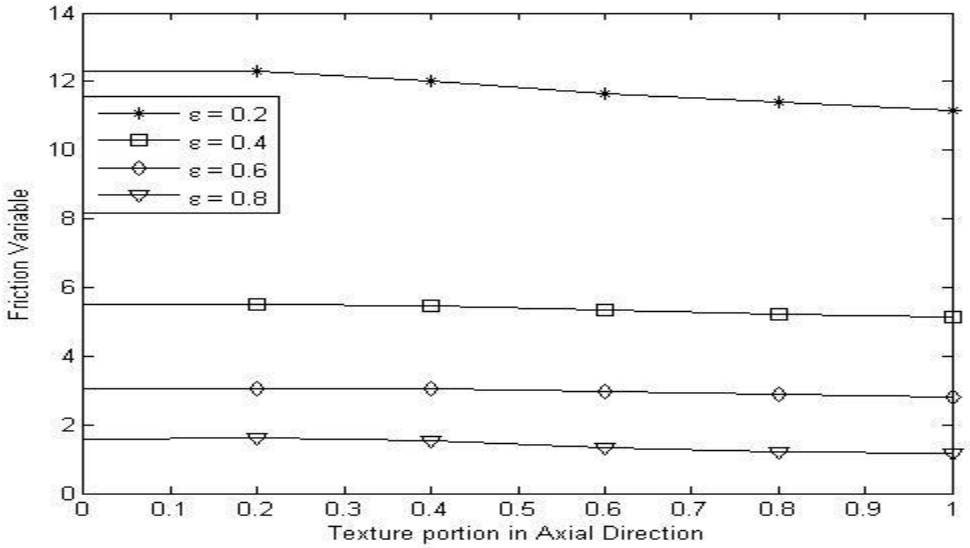

Figure 3.16: Effect of textured portion in axial direction on friction variable of textured journal bearing ($L/D = 1,\ S_p = 0.6,\ \Delta\bar{h} = 0.1,\ \alpha = 1$)

3.3.2 Negative cylindrical texture:

3.3.2.1 Effect of texture depth:

Load carrying capacity, flow coefficient and friction variable of negative cylindrical textured journal bearing are plotted against textured depth in Figs 3.17 to 3.19 respectively for $L/D = 1$, $S_p = 0.6$, $\alpha = 1$, $\beta = 1$. Non dimensional texture depth is varied from 0 to 0.06 and eccentricity ratios considered are 0.2, 0.4, 0.6 and 0.8. It is observed from Fig. 3.17 that the load carrying capacity decreases slightly at eccentricity ratio 0.8; whereas it is not much influenced by texture depth at lower eccentricity ratios. Flow coefficient is observed to be decreased with increase in texture depth as seen in Fig. 3.18. Figure 3.19 clearly shows that the effect of texture depth on friction variable is not significant; it reduces little at lower eccentricity ratio (0.2).

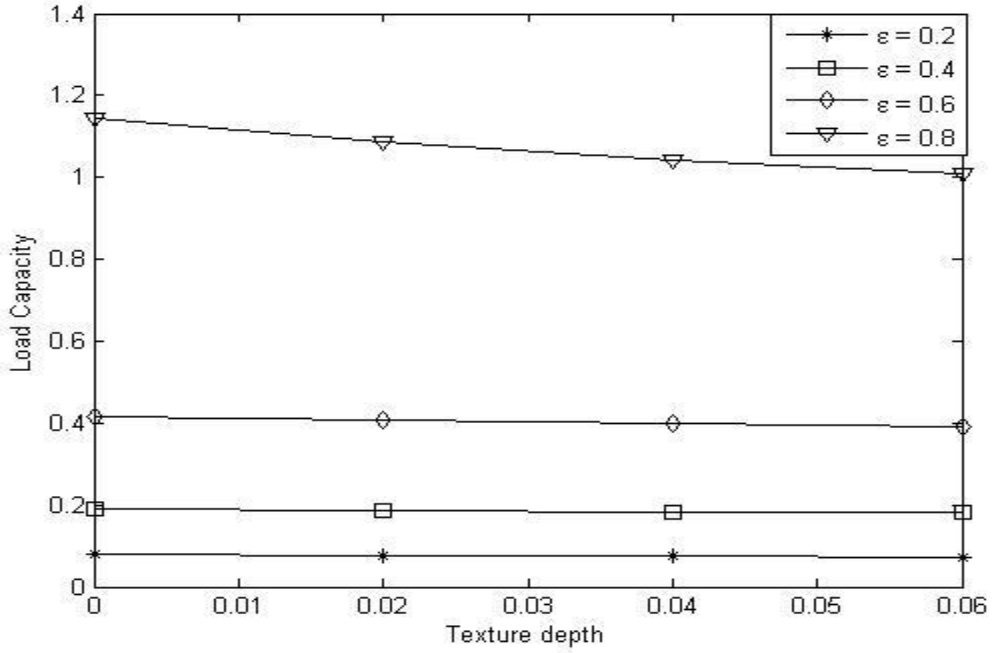

Figure 3.17: Variation of load carrying capacity with texture depth

$(L/D = 1,\ S_p = 0.6,\ \alpha = 1,\ \beta = 1)$

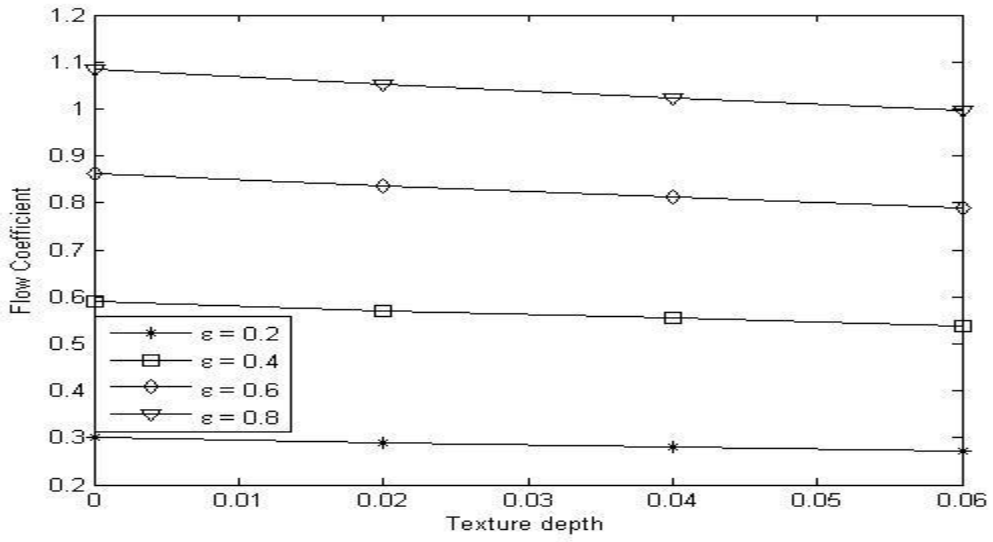

Figure 3.18: Variation of flow coefficient with texture depth

$(L/D = 1,\ S_p = 0.6,\ \alpha = 1,\ \beta = 1)$

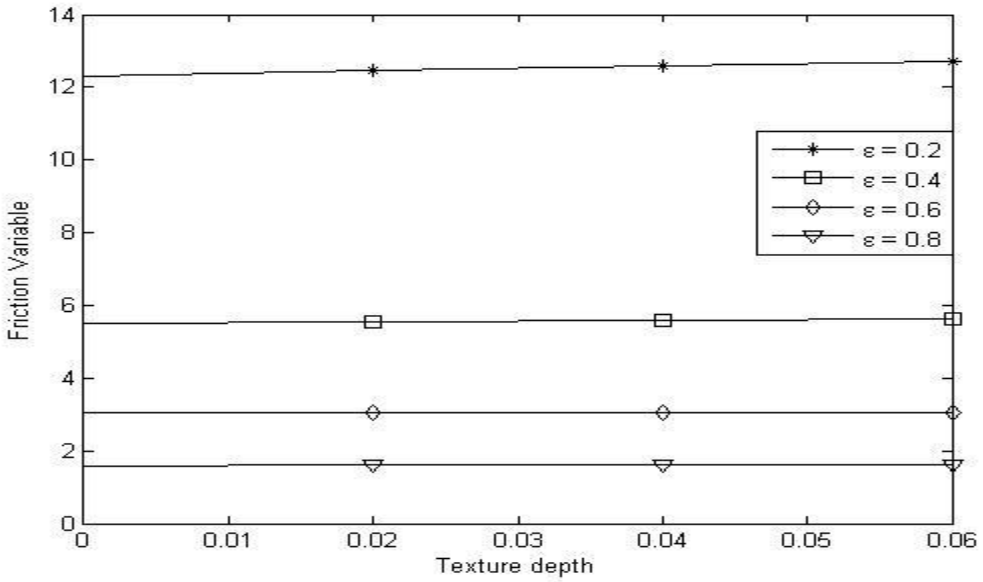

Figure 3.19: Variation of friction variable with texture depth

$(L/D = 1,\ S_p = 0.6,\ \alpha = 1,\ \beta = 1)$

3.3.2.2 Effect of eccentricity ratio and texture area density:

Load carrying capacity, flow coefficient and friction variable of negative cylindrical textured bearing are plotted against eccentricity ratio for texture area density of 0, 0.2, 0.4 and 0.6 in Figs. 3.20 through 3.22 for $L/D = 1,\ \Delta\bar{h} = 0.1,\ \alpha = 1,\ \beta = 1$. It has been observed from Fig. 3.20 that load carrying capacity increases with increase in eccentricity ratio, which is obvious. However, load carrying capacity decreases little for texture area density 0.6 at higher eccentricity ratio only. On the other hand flow coefficient decreases with increase in texture area density for all eccentricity ratios as seen from Fig. 3.21. Effect of texture area density on friction variable is also observed to be insignificant except at lower eccentricity ratio as depicted in Fig. 3.22.

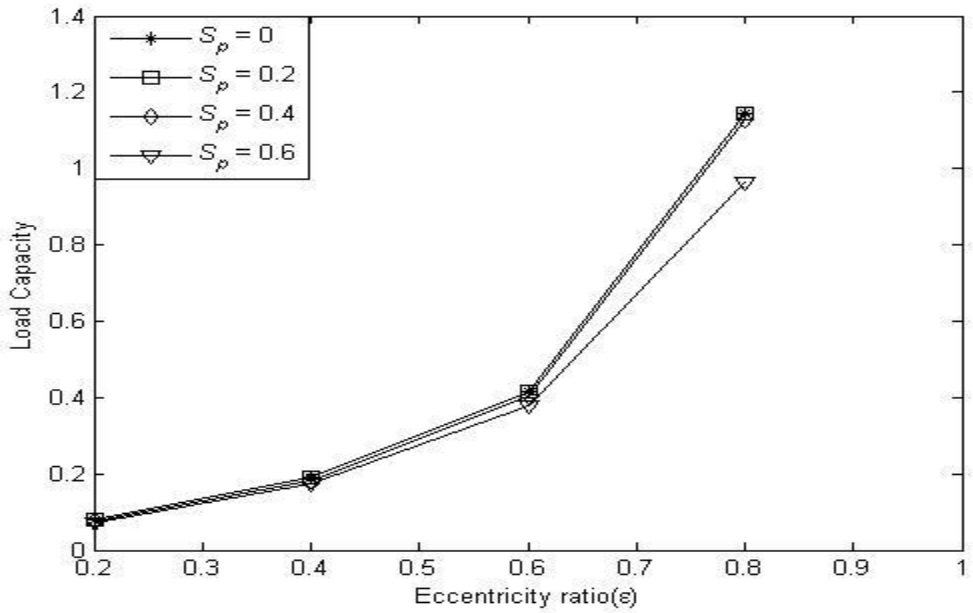

Figure 3.20: Variation of load carrying capacity with eccentricity ratio of textured journal bearing ($L/D = 1,\ \Delta\bar{h} = 0.1,\ \alpha = 1,\ \beta = 1$)

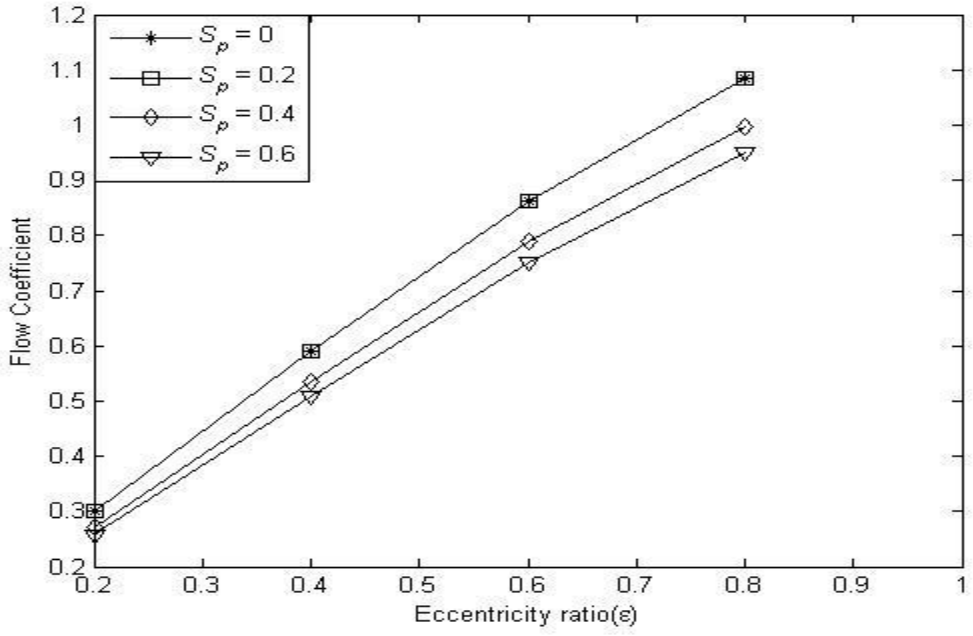

Figure 3.21: Variation of flow coefficient with eccentricity ratio of textured journal bearing

($L/D = 1,\ \Delta\bar{h} = 0.1,\ \alpha = 1,\ \beta = 1$)

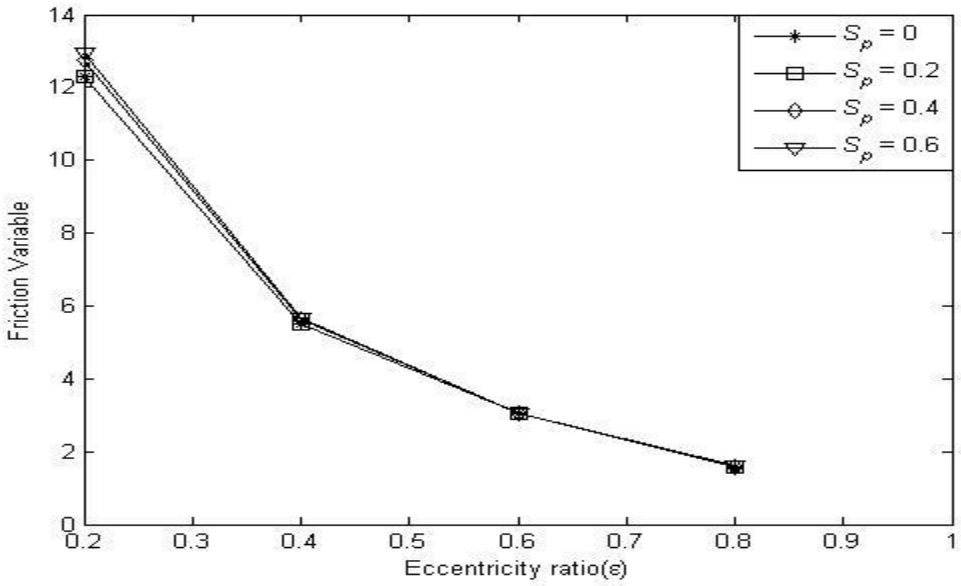

Figure 3.22: Variation of friction variable with eccentricity ratio of textured journal bearing

$$(L/D = 1,\ \Delta\bar{h} = 0.1,\ \alpha = 1,\ \beta = 1)$$

3.3.2.3 Effect of textured portion in circumferential direction:

Load carrying capacity, flow coefficient and friction variable are plotted against textured portion in circumferential direction in Figs. 3.23 to 3.25 respectively. Eccentricity ratio taken is 0.2 to 0.8, Texture area density is 0.6 and dimensionless dimple height is 0.1. Full texture has been taken in axial direction and textured portion is varied in circumferential direction. Load carrying capacity decreases with increase in textured portion from 40% to 60% in circumferential direction for eccentricity ratio 0.8 only. The effect of textured portion in circumferential direction on load carrying capacity is not at all significant for all other cases considered as seen from Fig. 323. Flow coefficient decreases slightly with increase in textured portion up to 60% in circumferential direction for all eccentricity ratios considered. However, it remains the same beyond 60% textured portion up to fully textured condition. Effect of textured portion in circumferential direction on friction variable is prominent only for eccentricity ratio 0.2. Friction variable increases slightly from un-textured to also have a similar trend like load carrying capacity. Friction increases considerably from un-textured to 40 % textured portion in circumferential direction for eccentricity ratio 0.2.

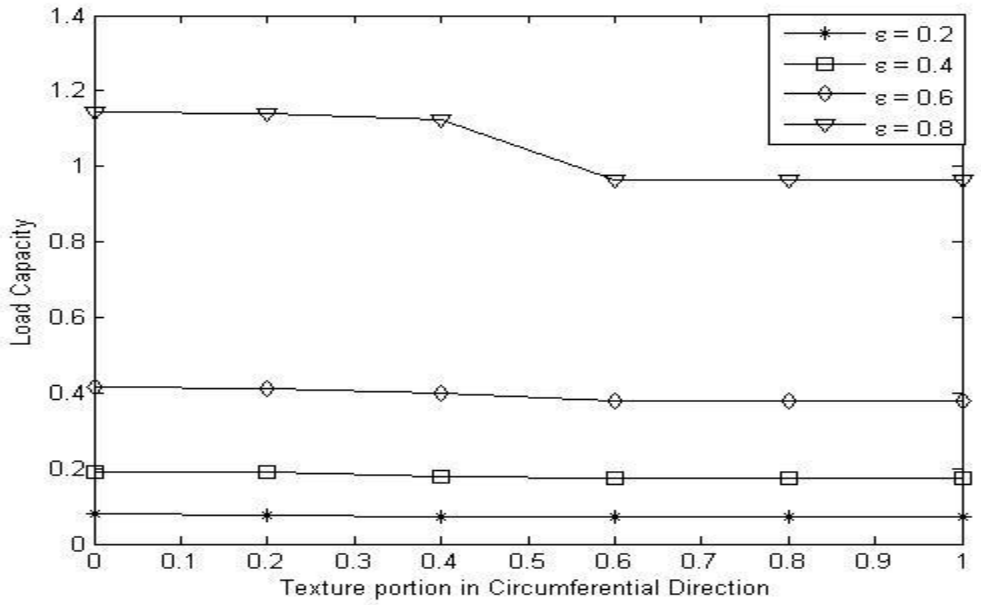

Figure 3.23: Effect of textured portion in circumferential direction on load carrying capacity of textured journal bearing ($L/D = 1,\ S_p = 0.6,\ \Delta\bar{h} = 0.1,\ \beta = 1$)

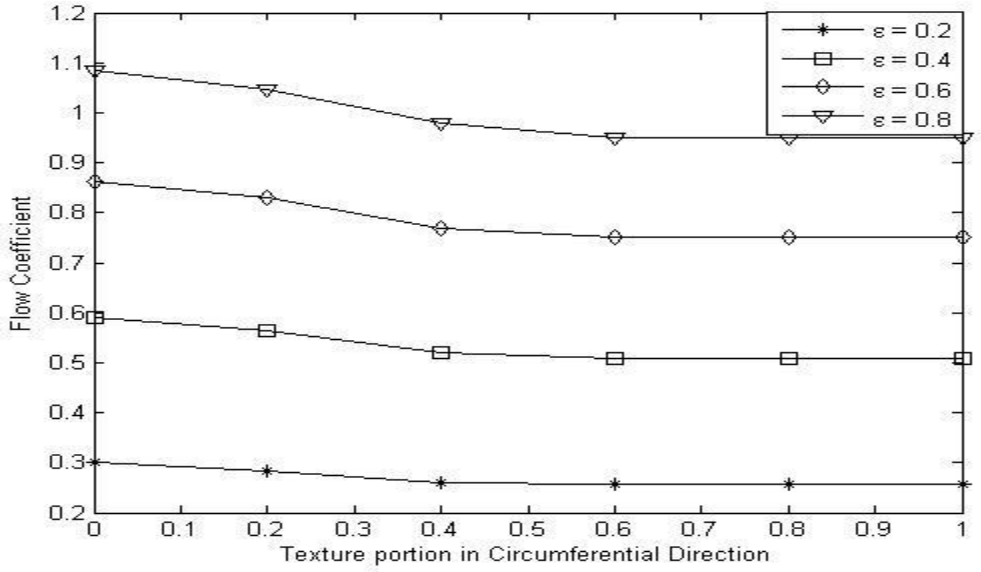

Figure 3.24: Effect of textured portion in circumferential direction on flow coefficient of textured journal bearing ($L/D = 1,\ S_p = 0.6,\ \Delta\bar{h} = 0.1,\ \beta = 1$)

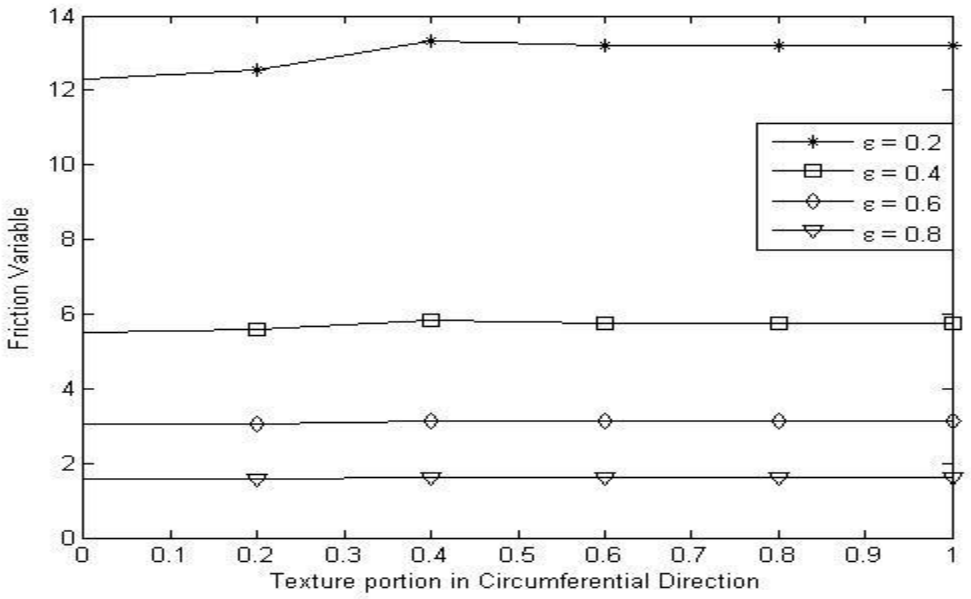

Figure 3.25: Effect of textured portion in circumferential direction friction variable of textured journal bearing ($L/D = 1,\ S_p = 0.6,\ \Delta\bar{h} = 0.1,\ \beta = 1$)

3.3.2.4 Effect of textured portion in axial direction:

Load carrying capacity, flow coefficient and friction variable are plotted against textured portion in axial direction in Figs. 3.26 to 3.28 respectively. Eccentricity ratios considered are 0.2, 0.4, 0.6 and 0.8, Texture area density is 0.6 and dimensionless dimple height is 0.1. Full texture has been taken in circumferential direction and textured portion is varied in axial direction. It has been observed that load carrying capacity and flow coefficient decreases, when friction variable increases with increase in textured portion in axial direction. However, the variations of all the performance parameters considered here are very small.

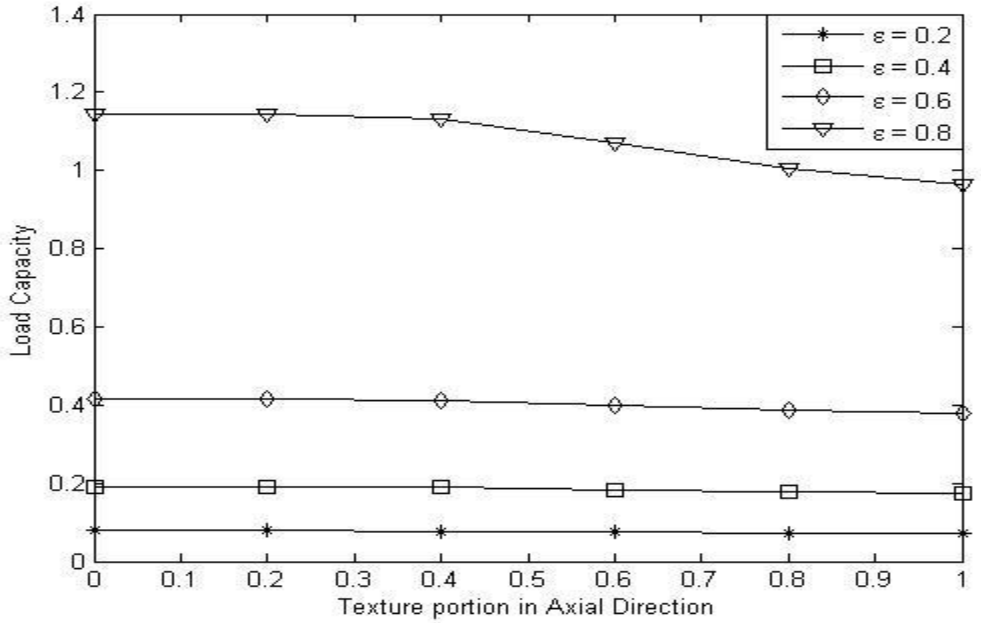

Figure 3.26: Effect of textured portion in axial direction on load carrying capacity of textured journal bearing ($L/D = 1,\ S_p = 0.6,\ \Delta\bar{h} = 0.1,\ \alpha = 1$)

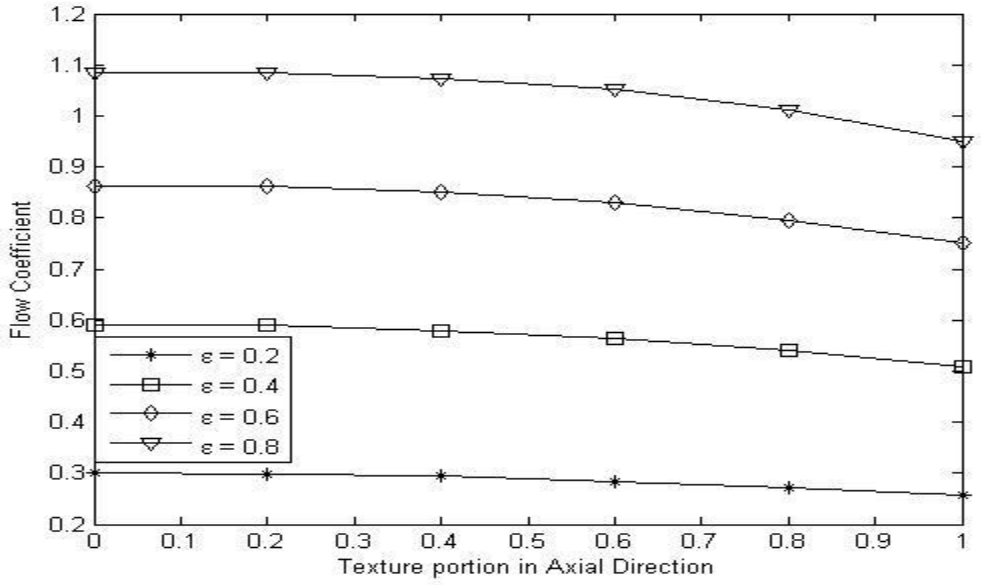

Figure 3.27: Effect of textured portion in axial direction on flow coefficient of textured journal bearing ($L/D = 1,\ S_p = 0.6,\ \Delta\bar{h} = 0.1,\ \alpha = 1$)

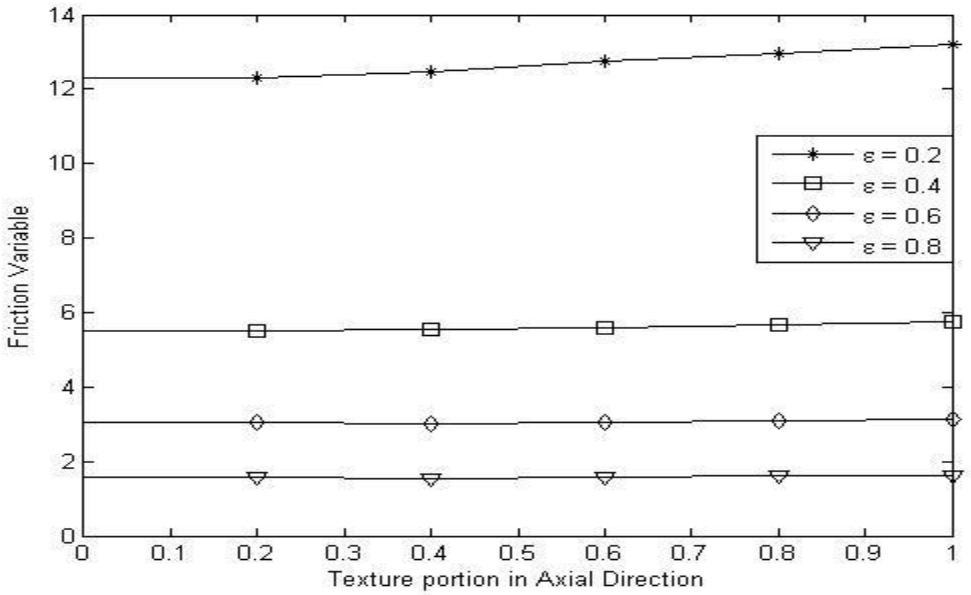

Figure 3.28: Effect of textured portion in axial direction on friction variable of textured journal bearing ($L/D = 1,\ S_p = 0.6,\ \Delta\bar{h} = 0.1,\ \alpha = 1$)

3.4 Summary:

A steady state analysis has been presented for positive and negative cylindrical textured journal bearing. As a whole, it may be inferred that performance of negative cylindrical textured journal bearing does not improve compared to un-textured bearing, whereas the performance of positive cylindrical textured bearing is improved in certain conditions, e.g., load carrying capacity and flow coefficient improve particularly at higher eccentricity ratios and friction variable decreases at lower eccentricity ratios. In view of the above analysis, use of positive cylindrical textured bearing may be recommended, whereas negative cylindrical textured bearing cannot be recommended for use.

CHAPTER 4

ELLIPTICAL TEXTURED JOURNAL BEARING

4.0 Introduction:

The steady-state characteristics of cylindrical textured journal bearing have been presented in the previous chapter. Elliptical texturing has been considered here in this chapter and a theoretical analysis has been carried out to study the steady-state performance characteristics of elliptical textured journal bearing. Performance characteristics are load carrying capacity, flow coefficient and friction variable. The effects of different parameters like Texture density, Texture portion in circumferential and axial directions on the performance characteristics are analyzed. Unlike cylindrical textured bearings, published results are not available for elliptical textured bearings. Therefore, there has been no scope to compare the presented results in this chapter.

4.1 Elliptical texture:

It is possible to texture either sides of the bearing surface as shown in Fig. 4.1. The figure has been reproduced from chapter 2 for ease of reference. If texturing produces asperities on the surface is considered as positive texturing, the dimples produced on inside the surface may be termed as negative texturing. The negative type of texturing can be produced by laser surface texturing, when positive type can be produced by Sputtering, photolithography [7-8]. Figure 4.1 represents the block diagram of positive and negative elliptical textured journal bearing. Figure 4.2 represents geometry of elliptical texture. Here *a* and *b* are half length of ellipse axis in *x*- and *z*-direction.

4.1.1 Numerical formulation:

Non Dimensional Reynolds equation can be written as [40]:

$$\frac{\partial}{\partial\theta}\left(\bar{h}^{-3}\frac{\partial\bar{p}}{\partial\theta}\right)+\left(\frac{D}{L}\right)^{2}\frac{\partial}{\partial\bar{z}}\left(\bar{h}^{-3}\frac{\partial\bar{p}}{\partial\bar{z}}\right)=\frac{\partial\bar{h}}{\partial\theta} \qquad (4.1)$$

Non dimensional film thickness for negative and positive elliptical texture can be written as [38]

$$\left.\begin{aligned} \overline{h} &= 1+\varepsilon\cos\theta \pm \frac{\sqrt{\xi_1\xi_2}}{\delta} \quad if \quad \frac{\xi_1}{\xi_2}x_1^{\,2} + \frac{\xi_2}{\xi_1}y_1^{\,2} \le 1 \\ \overline{h} &= 1+\varepsilon\cos\theta \quad if \quad \frac{\xi_1}{\xi_2}x_1^{\,2} + \frac{\xi_2}{\xi_1}y_1^{\,2} > 1 \end{aligned}\right\} \qquad (4.2)$$

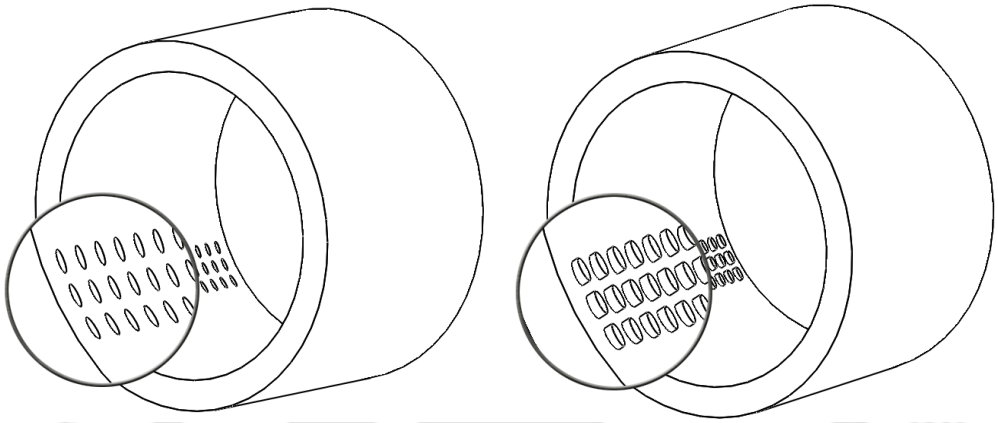

Figure 4.1: Negative and positive elliptical textured journal bearing

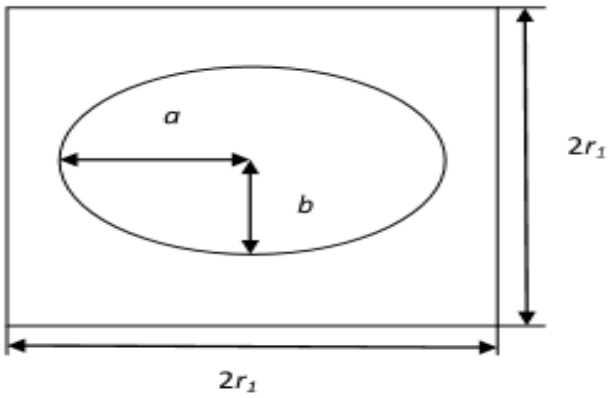

Figure 4.2: Geometry of elliptical texture

4.2 Results and discussion:

Since no benchmark results are available, the steady-state characteristics are estimated by modifying the code developed for cylindrical textured bearing (Chapter 3) by incorporating the film thickness equation as given in Eqn. 4.2 for positive and negative texturing.

4.2.1 Positive elliptical textured journal bearing:

4.2.1.1 Effect of eccentricity ratio and textured area density:

Figures 4.3 through 4.5 represent variation of load carrying capacity, flow coefficient and friction variable with eccentricity ratio of positive elliptical textured bearing for $L/D = 1$, $S_p = 0$ to 0.6, $\Delta\bar{h} = 0.03$, $\alpha = 1$, $\beta = 1$. Eccentricity ratio is varied from 0.2 to 0.8 and textured area densities considered are 0, 0.2, 0.4 and 0.6. The load carrying capacity and flow coefficient increase whereas friction variable decreases with the increase in eccentricity ratios as seen in the Figs. 4.3 to 4.5. The effect of textured area density has been observed to be prominent above eccentricity ratio 0.6 for load carrying capacity as it is more for textured area density of 0.6 compared to 0, 0.2 and o.4. Flow coefficient is marginally more for textured area density 0.6 for the entire range of eccentricity ratio than other textured area density considered here. Effect of textured area density on friction variable is found to be insignificant for all the cases considered.

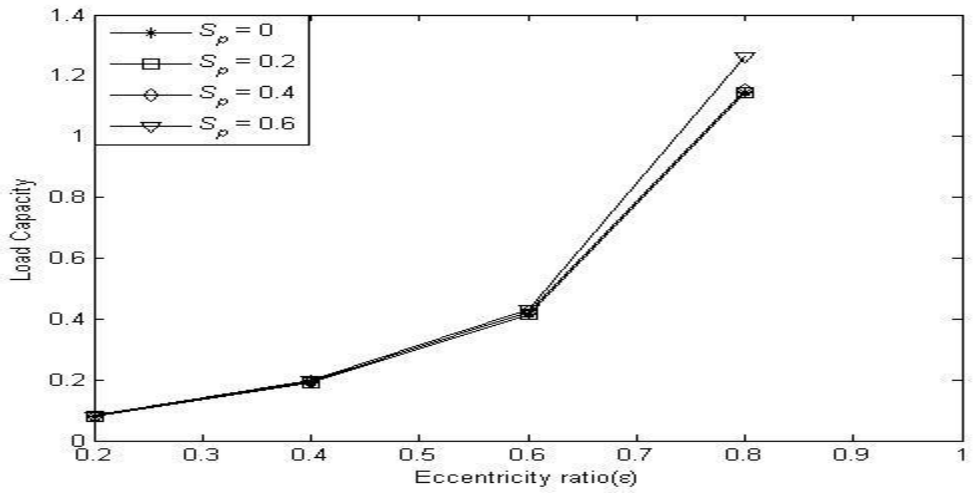

Figure 4.3: Variation of load carrying capacity with eccentricity ratio of elliptical textured journal bearing ($L/D = 1$, $\Delta\bar{h} = 0.03$, $\alpha = 1$, $\beta = 1$)

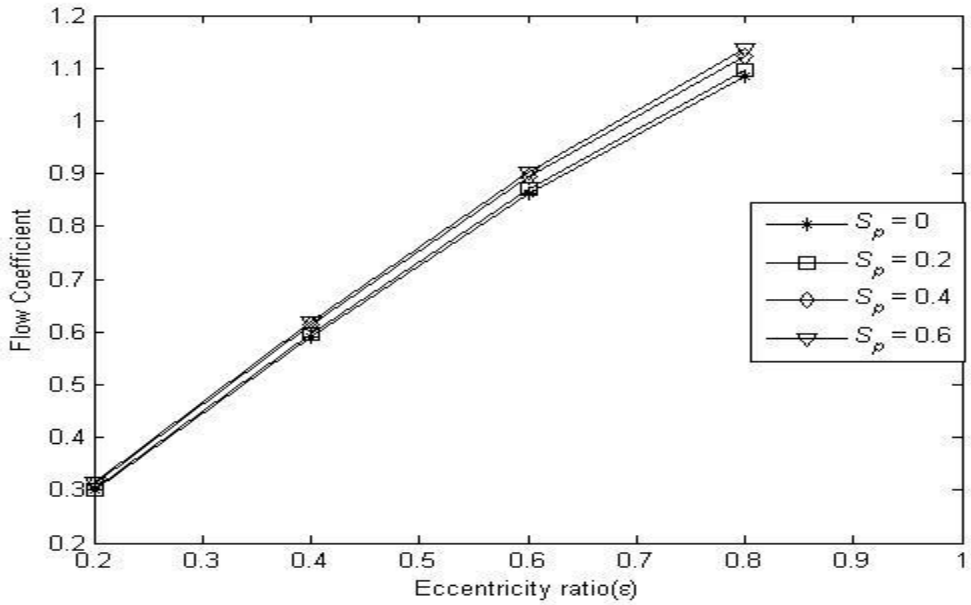

Figure 4.4: Variation of flow coefficient with eccentricity ratio of elliptical textured journal bearing ($L/D = 1,\ \Delta\bar{h} = 0.03,\ \alpha = 1,\ \beta = 1$)

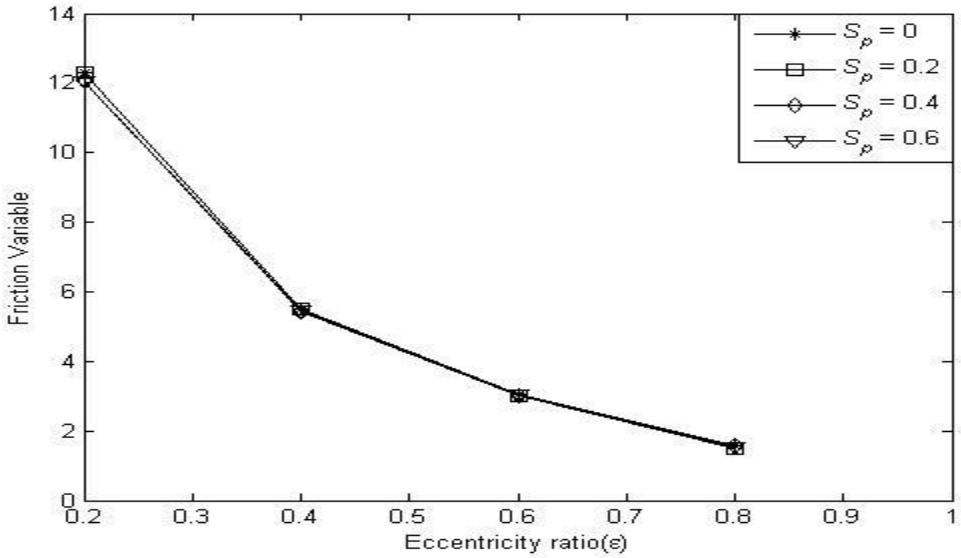

Figure 4.5: Variation of friction variable with eccentricity ratio of elliptical textured journal bearing ($L/D = 1,\ \Delta\bar{h} = 0.03,\ \alpha = 1,\ \beta = 1$)

4.2.1.2 Effect of textured portion in circumferential direction:

Figures 4.6 through 4.8 represent the effect of textured portion in circumferential direction on load carrying capacity, flow coefficient and friction variable of Elliptical Textured journal bearing. It has been observed that the load carrying capacity remains the same from un-textured condition to 40% textured portion in circumferential direction and then it increases up to 60% and finally remains more or less constant up to fully textured condition for eccentricity ratio 0.8 as seen in Fig. 4.6. The effect of textured portion in circumferential direction is not significant on load carrying capacity in all other cases considered. Flow coefficient increases slightly for all the eccentricity ratios considered with the increase in textured portion in circumferential direction as seen in Fig. 4.7. The effect of textured portion in circumferential direction on friction variable is also found to be insignificant except for eccentricity ratio 0.2 as observed from Fig. 4.8. .

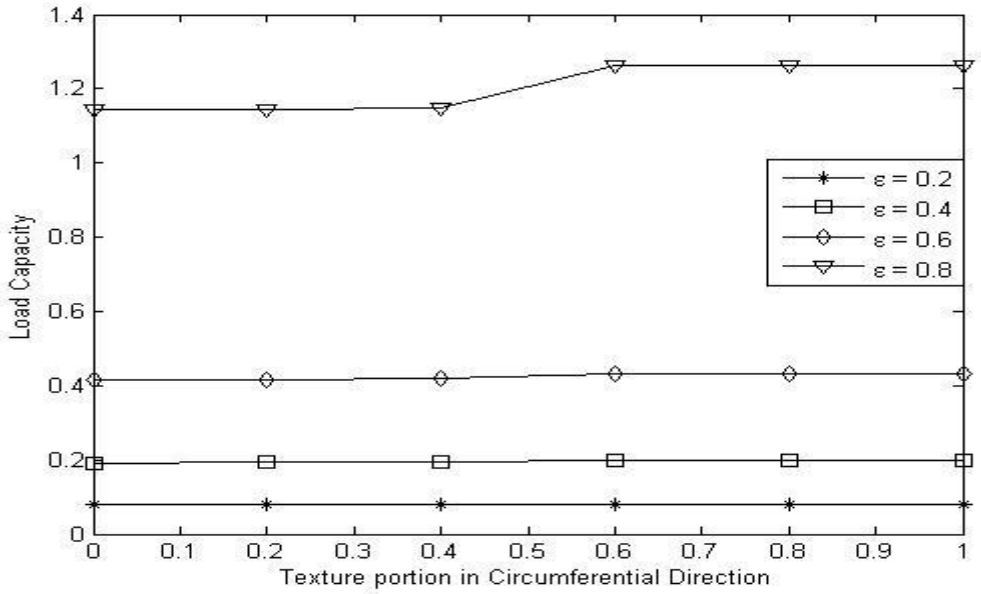

Figure 4.6: Effect of textured portion in circumferential direction on load carrying capacity of elliptical textured journal bearing ($L/D = 1,\ S_p = 0.6,\ \Delta\bar{h} = 0.03,\ \beta = 1$)

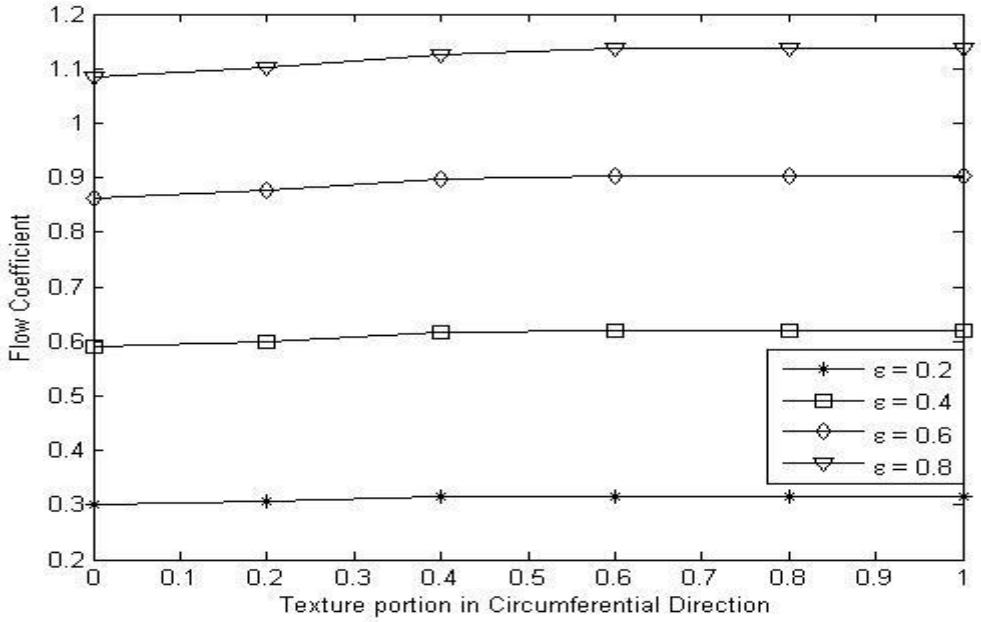

Figure 4.7: Effect of textured portion in circumferential direction on flow coefficient of elliptical textured journal bearing ($L/D = 1,\ S_p = 0.6,\ \Delta\bar{h} = 0.03,\ \beta = 1$)

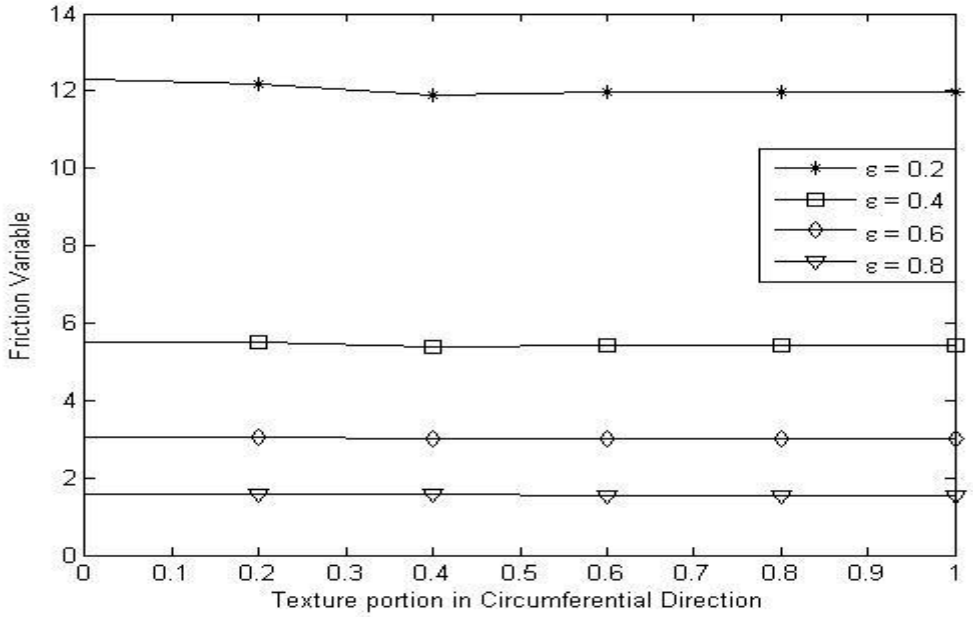

Figure 4.8: Effect of textured portion in circumferential direction on friction variable of elliptical textured journal bearing ($L/D = 1,\ S_p = 0.6,\ \Delta\bar{h} = 0.03,\ \beta = 1$)

4.2.1.3 Effect of textured portion in axial direction:

Load carrying capacity, flow coefficient and friction variable are plotted against textured portion in axial direction in Figures 4.9 through 4.11 respectively. Texture area density is 0.6 and dimensionless dimple height is 0.03. Full texture has been taken in circumferential direction and textured portion is varied in axial direction. It has been observed that load carrying capacity increases only for eccentricity ratio 0.8 with the increase in textured portion in axial direction as seen in Fig. 4.9. Flow coefficient increases slightly with increase in textured portion in axial direction for all the eccentricity ratios considered as evident in Fig. 4.10. The effect of textured portion in axial direction is very minimal in case of friction variable; it has been observed from Fig. 4.11 that there is only little decrease of friction variable at eccentricity ratio 0.2 from un-textured condition to fully textured condition.

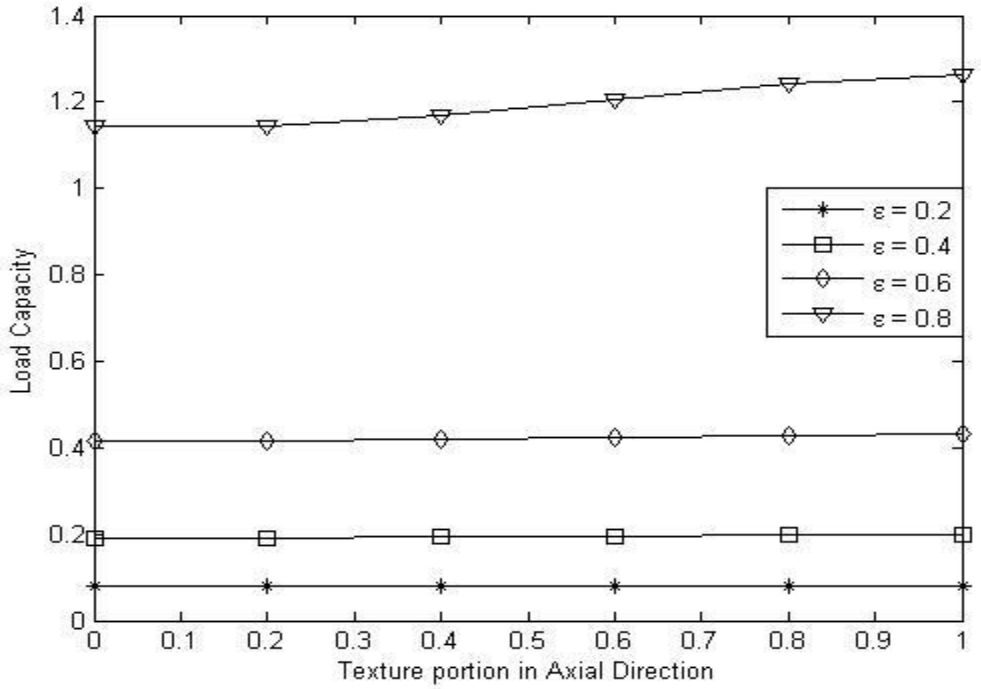

Figure 4.9: Effect of textured portion in axial direction on load carrying capacity of elliptical textured journal bearing ($L/D = 1,\ S_p = 0.6,\ \Delta\bar{h} = 0.03,\ \alpha = 1$)

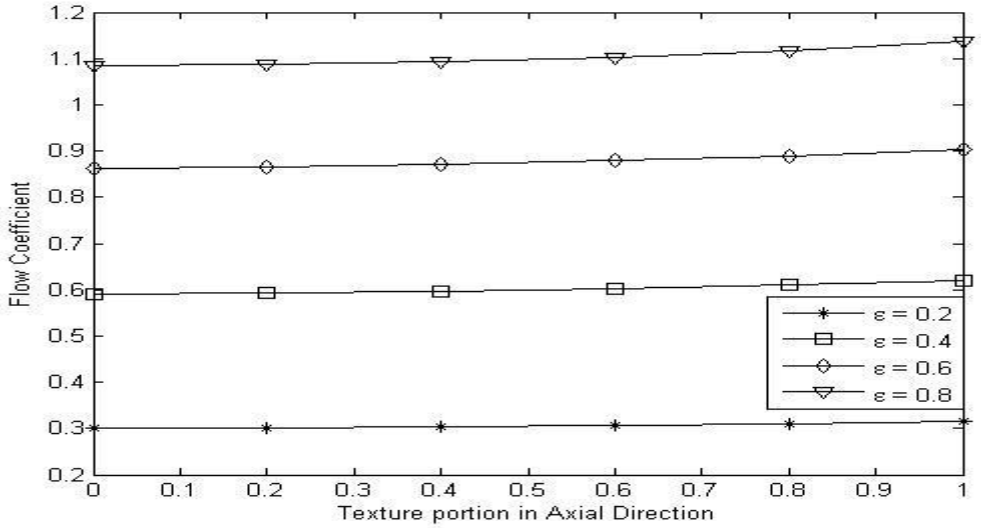

Figure 4.10: Effect of textured portion in axial direction on flow coefficient of elliptical textured journal bearing ($L/D = 1,\ S_p = 0.6,\ \Delta\bar{h} = 0.03,\ \alpha = 1$)

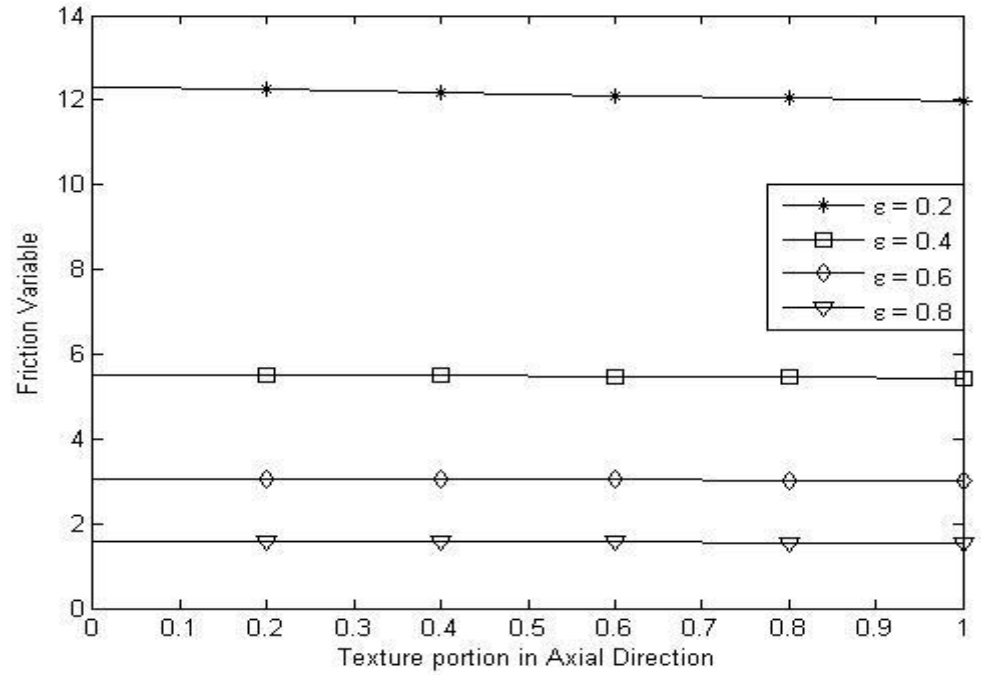

Figure 4.11: Effect of textured portion in axial direction on friction variable of elliptical textured journal bearing ($L/D = 1,\ S_p = 0.6,\ \Delta\bar{h} = 0.03,\ \alpha = 1$)

4.2.2 Negative elliptical textured journal bearing:

4.2.2.1 Effect of eccentricity ratio and textured area density:

Load carrying capacity, flow coefficient and friction variable are presented for different operating conditions (ε) for a particular set of geometry ($L/D = 1,\ \Delta\bar{h} = 0.03,\ \alpha = 1,\ \beta = 1$) and textured area density of 0, 0.2, 0.4 and 0.6 in Figures 4.12 through 4.14. Load carrying capacity and flow coefficient increase when friction variable decreases with increase in eccentricity ratio. Figure 4.12 depicts that there is little decrease in load carrying capacity at higher eccentricity ratios only for textured area density 0.6 compared to other cases considered. Flow coefficient has been observed to be slightly less at textured area density 0.6 for the whole range of eccentricity ratios compared to with lower values of textured area density as seen in Fig. 4.13. It is evident from Fig. 4.14 that effect of textured area density on friction variable is insignificant.

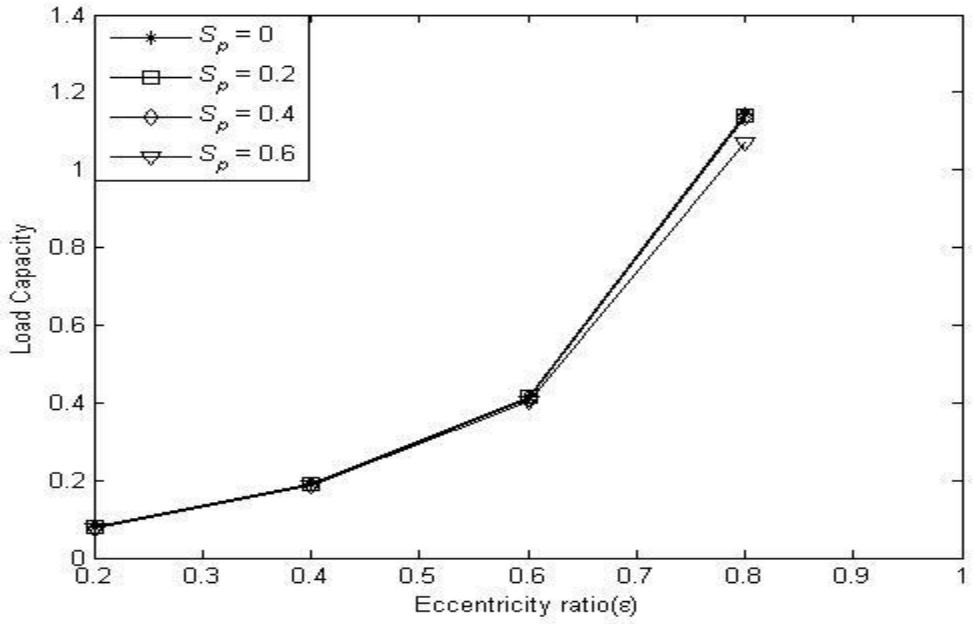

Figure 4.12: Variation of load carrying capacity with eccentricity ratio of elliptical textured journal bearing ($L/D = 1,\ \Delta\bar{h} = 0.03,\ \alpha = 1,\ \beta = 1$)

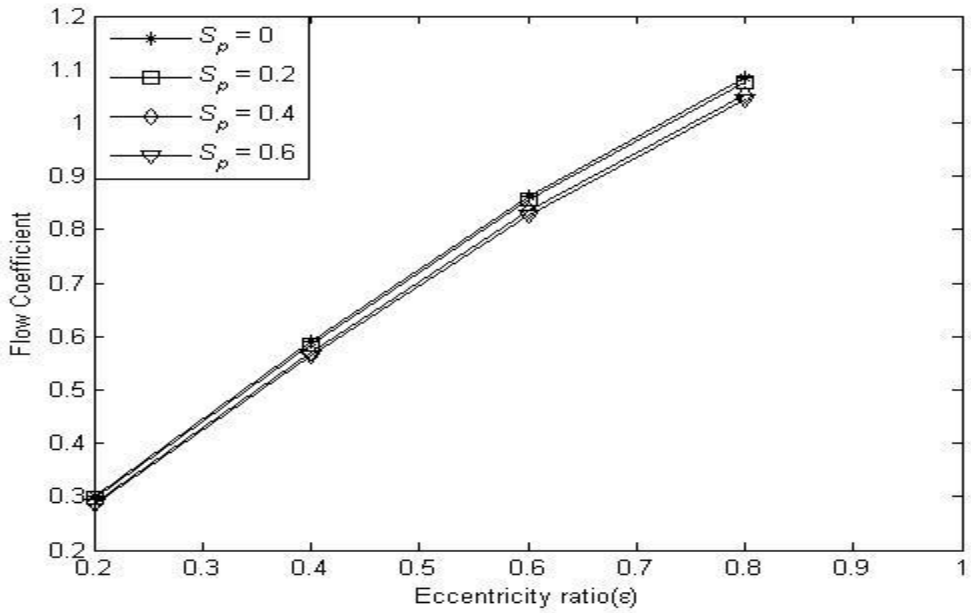

Figure 4.13: Variation of flow coefficient with eccentricity ratio of elliptical textured journal bearing ($L/D = 1,\ \Delta\bar{h} = 0.03,\ \alpha = 1,\ \beta = 1$)

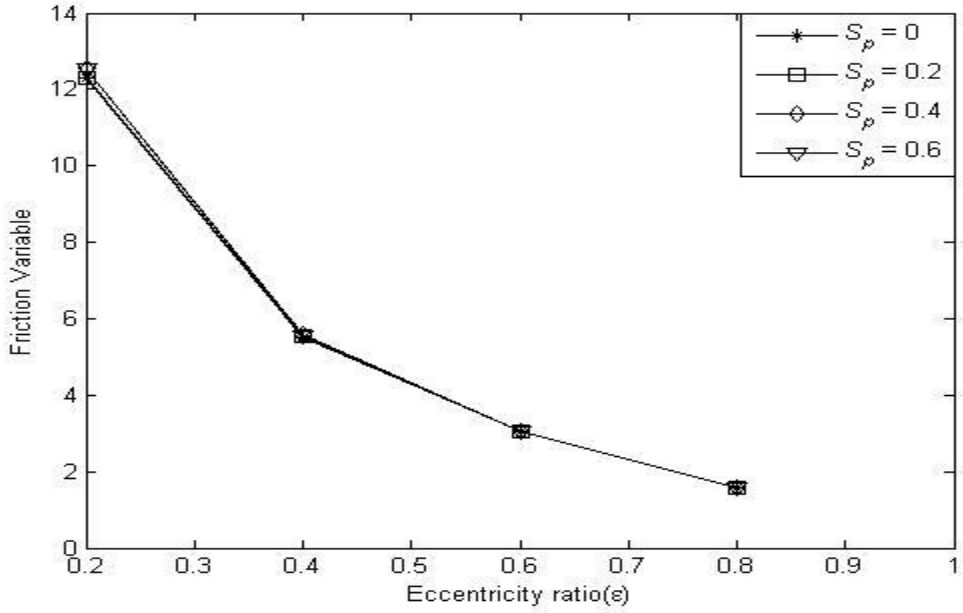

Figure 4.14: Variation of friction variable with eccentricity ratio of elliptical textured journal bearing ($L/D = 1,\ \Delta\bar{h} = 0.03,\ \alpha = 1,\ \beta = 1$)

4.2.2.2 Effect of textured portion in circumferential direction:

Load carrying capacity, flow coefficient and friction variable are plotted against textured portion in circumferential direction in Figures 4.15 through 4.17 respectively for $L/D = 1$, $S_p = 0.6$, $\Delta\bar{h} = 0.03$, $\beta = 1$. Full texture has been taken in axial direction and textured portion is varied in circumferential direction. Load carrying capacity decreases from 40% to 60% textured portion in circumferential direction and then remains constant only for eccentricity ratio 0.8 as depicted in Fig. 4.15. It remains more or less the same for all other eccentricity ratios considered. There is a slight decrease in flow coefficient from un-textured to fully textured condition for all eccentricity ratios considered as observed from Fig. 4.16. The effect of textured portion in circumferential direction on friction variable has been observed from Fig. 4.17 to be not noteworthy except for a small increase in the parameter for eccentricity ratio 0.2.

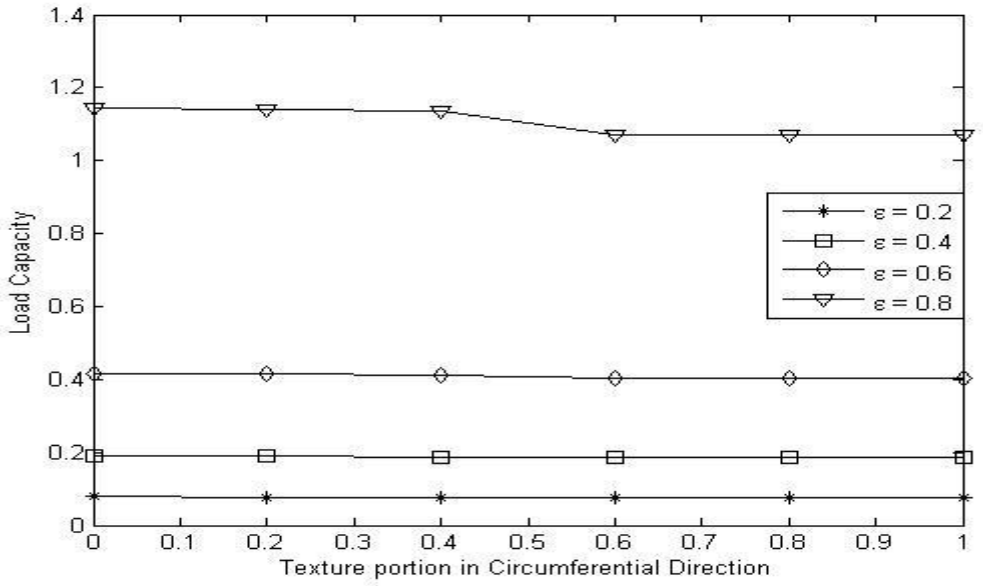

Figure 4.15: Effect of textured portion in circumferential direction on load carrying capacity of elliptical textured journal bearing ($L/D = 1$, $S_p = 0.6$, $\Delta\bar{h} = 0.03$, $\beta = 1$)

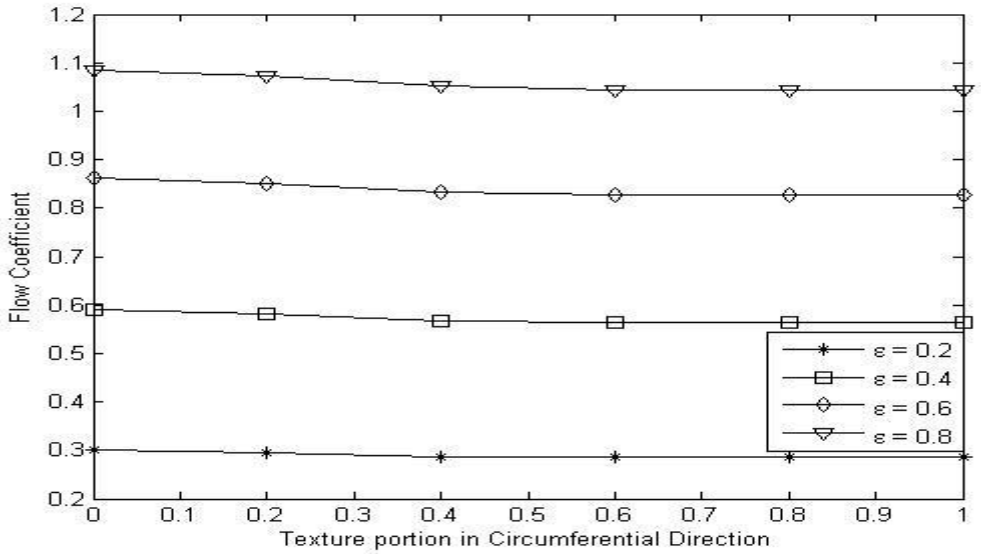

Figure 4.16: Effect of textured portion in circumferential direction on flow coefficient of elliptical textured journal bearing ($L/D = 1,\ S_p = 0.6,\ \Delta\bar{h} = 0.03,\ \beta = 1$)

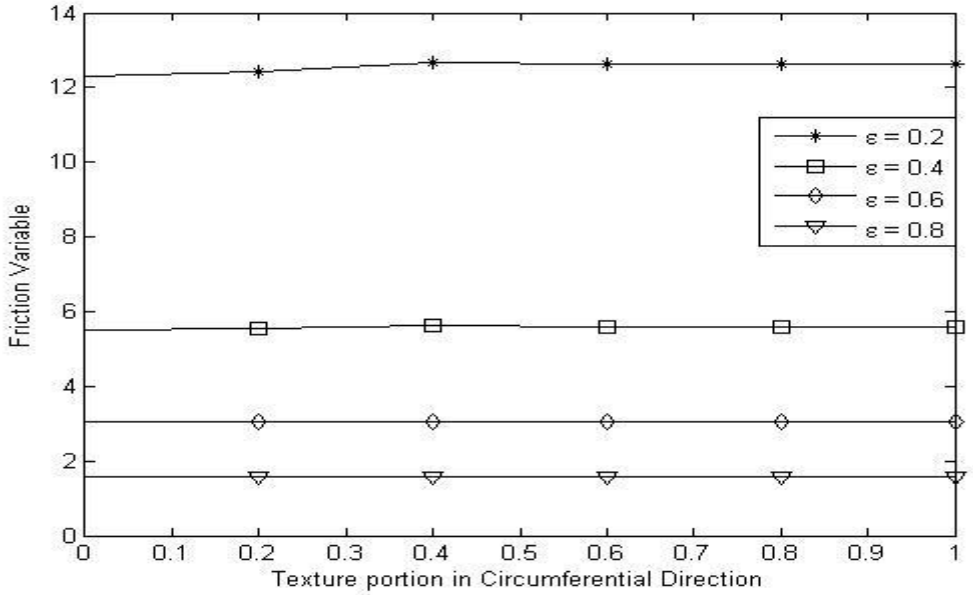

Figure 4.17: Effect of textured portion in circumferential direction on friction variable of elliptical textured journal bearing ($L/D = 1,\ S_p = 0.6,\ \Delta\bar{h} = 0.03,\ \beta = 1$)

4.2.2.3 Effect of textured portion in axial direction:

Load carrying capacity, flow coefficient and friction variable are plotted against textured portion in axial direction in Figures 4.18 through 4.20 respectively for $L/D = 1$, $S_p = 0.6$, $\Delta\bar{h} = 0.03$, $\alpha = 1$. Full texture has been taken in circumferential direction and textured portion is varied in axial direction. It has been observed from Fig. 4.18 that load carrying capacity decreases slightly at eccentricity ratio 0.8 and remains unaffected at other eccentricity ratios with the increase in textured portion in axial direction. Flow coefficient decreases slightly for all eccentricity ratios considered with the increase in textured portion in axial direction as observed from Fig. 4.19. Friction variable has been observed to be unaffected by variation of texturing in axial direction for all the cases considered, which can be seen in Fig. 4.20.

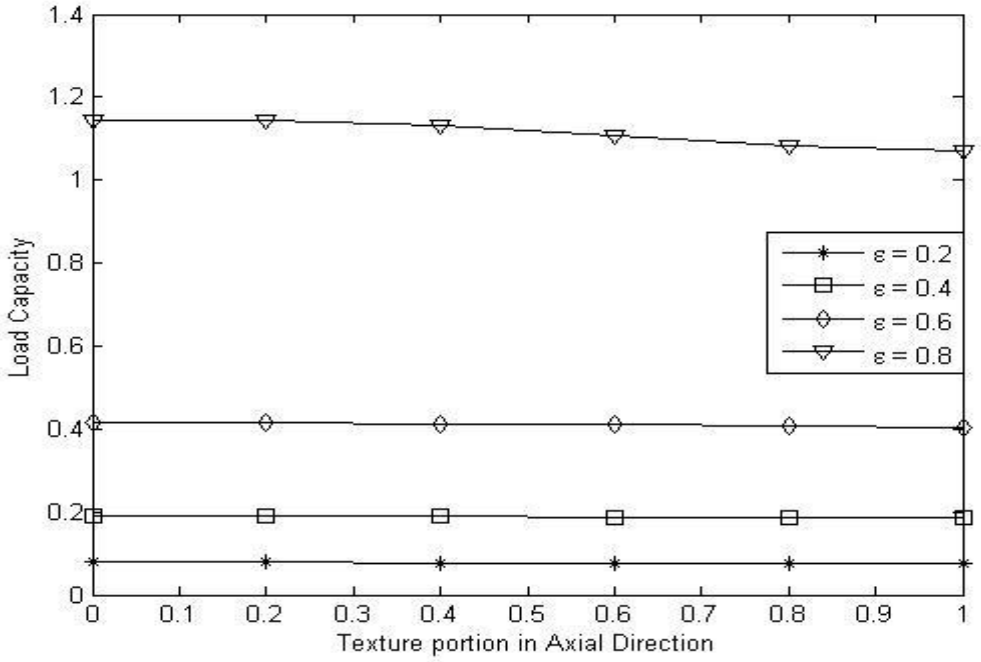

Figure 4.18: Effect of textured portion in axial direction on load carrying capacity of elliptical textured journal bearing ($L/D = 1$, $S_p = 0.6$, $\Delta\bar{h} = 0.03$, $\alpha = 1$)

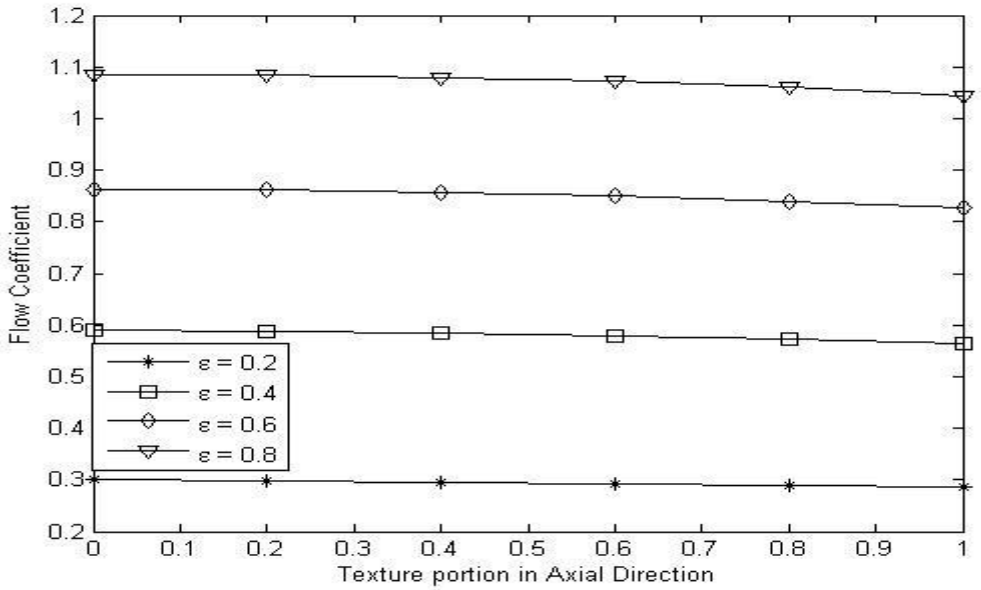

Figure 4.19: Effect of textured portion in axial direction on flow coefficient of elliptical textured journal bearing ($L/D = 1,\ S_p = 0.6,\ \Delta\bar{h} = 0.03,\ \alpha = 1$)

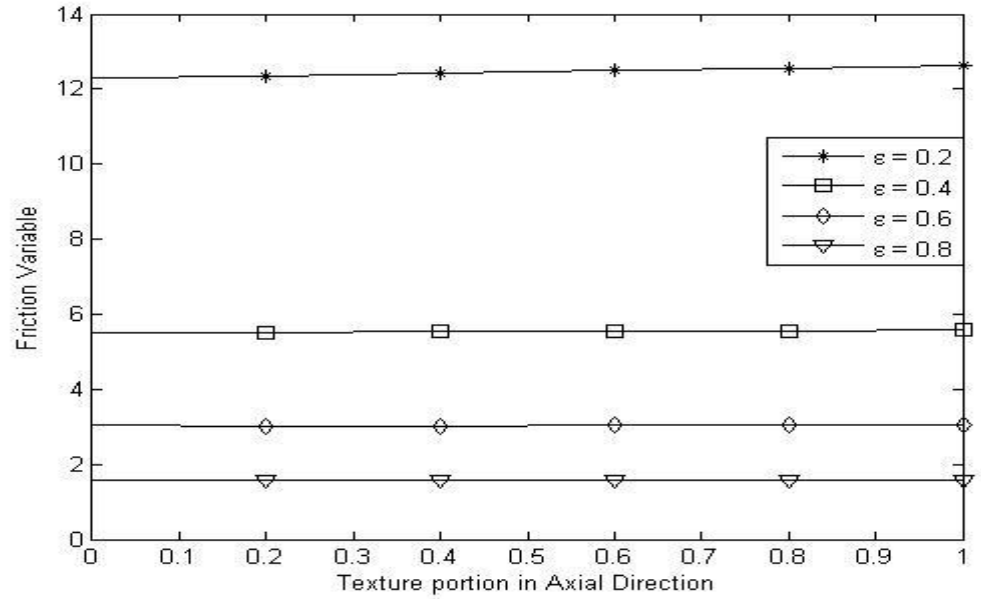

Figure 4.20: Effect of textured portion in axial direction on flow coefficient of elliptical textured journal bearing ($L/D = 1,\ S_p = 0.6,\ \Delta\bar{h} = 0.03,\ \alpha = 1$)

4.3 Summary:

An analysis has been carried out to study the steady-state performance of positive and negative elliptical textured journal bearing. It has been observed that load carrying capacity and flow coefficient improve at certain conditions for positive elliptical textured bearing, when friction variable does not get affected much. However, in the case of negative elliptical textured bearing performance parameters never improve but load carrying capacity and flow coefficient rather deteriorates at certain conditions. Therefore, use of negative elliptical bearing cannot be recommended, when positive elliptical bearings may be recommended for improved performance.

CHAPTER 5

DYNAMIC CHARACTERISTICS AND STABILITY OF POSITIVE CYLINDRICAL TEXTURED JOURNAL BEARING

5.0 Introduction:

Steady state characterization of both positive and negative cylindrical textured bearing was carried out in Chapter 3. Since performance characteristics of negative cylindrical textured bearing were not found suitable, a theoretical analysis has been carried out to study the dynamic characteristics and stability characteristics of positive cylindrical textured journal bearing only. The dynamic characteristics i.e., stiffness, damping coefficients and stability parameters, i.e., mass parameter and whirl ratio are presented in this chapter. Different plots are plotted by varying texture depth and texture portion etc.

5.1.1 Effect of texture depth on stiffness and damping coefficients:

Dynamic characteristics of hydrodynamic bearings include two direct stiffness coefficients and two cross-coupled stiffness coefficients, two direct damping coefficients and two cross-coupled damping coefficients as discussed in Chapter 2. The effect of texture depth on these dynamic coefficients are presented for positive cylindrical textured bearing in this section Direct stiffness coefficients for increasing texture depth are presented in Fig.5.1 and Fig. 5.2 for $L/D = 1$, $S_p = 0.6$, $\alpha = 1$, $\beta = 1$. It may be observed from Fig. 5.1 that the non-dimensional direct stiffness coefficients $\overline{K}_{\phi\phi}$, increases significantly with increase in texture depth for eccentricity ratio 0.8, increase slightly for eccentricity ratio 0.6 and it remains more or less constant at other eccentricity ratios considered. Fig. 5.2 depicts the effect of texture depth on $\overline{K}_{rr}$. It has been observed from the results that $\overline{K}_{rr}$ increases rapidly with increase in texture depth for eccentricity ratio 0.2, increases slightly for eccentricity ratio 0.4, whereas it decreases for eccentricity ratios 0.6 and 0.8. When decrease in $\overline{K}_{rr}$ is rapid at eccentricity ratio 0.8, it

decreases relatively slowly with increase in texture depth. Effect of texture depth on cross-coupled stiffness coefficients are presented in Figs. 5.3 and 5.4 for $L/D = 1$, $S_p = 0.6$, $\alpha = 1$, $\beta = 1$. It has been observed from Fig. 5.3 that with increase in texture depth $\overline{K}_{\phi r}$ increases slightly for all eccentricity ratios. The effect of texture depth on $\overline{K}_{r\phi}$ is observed to be interesting as it remains more or less constant for eccentricity ratios 0.2, 0.4 and 0.6, whereas it decreases for eccentricity ratio 0.8. Further the maximum value of the parameter at eccentricity ratio 0.8 is found to be less than that of eccentricity ratio 0.6 and the minimum value is even less than that of eccentricity ratio 0.4.

Variations of damping coefficients with texture depth have been presented in Figs. 5.5 through 5.8 for $L/D = 1$, $S_p = 0.6$, $\alpha = 1$, $\beta = 1$. The effect of texture depth on the non-dimensional direct damping coefficient $\overline{D}_{\phi\phi}$ can be seen in Fig. 5.5. It has been seen from the figure that $\overline{D}_{\phi\phi}$ increases significantly for eccentricity ratio 0.8, when there is a slight increase in the parameter for eccentricity ratios 0.6 and 0.4. However the parameter is more or less same for eccentricity ratio 0.2. The effect of texture depth on $\overline{D}_{rr}$ is insignificant for all the eccentricity ratios considered as seen in Fig. 5.6. Cross-coupled damping coefficient $\overline{D}_{\phi r}$ increases for eccentricity ratios 0.2, remains constant for eccentricity ratio 0.4, decreases for eccentricity ratios 0.6 and 0.8 as observed from Fig 5.7. From Fig 5.8, it has been observed that the non-dimensional cross-coupled damping coefficient $\overline{D}_{r\phi}$ decreases with increase in texture depth for eccentricity ratios 0.4 and 0.6 and 0.8, whereas it decreases for eccentricity ratio 0.2.

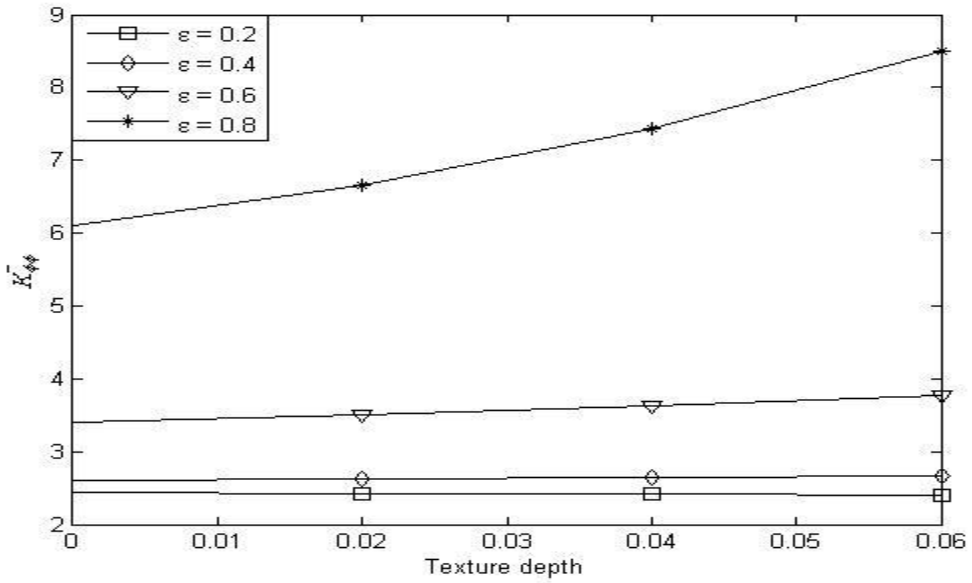

Figure 5.1: Variation of direct stiffness coefficient, $\overline{K}_{\phi\phi}$, with texture depth

$(L/D = 1,\ S_p = 0.6,\ \alpha = 1,\ \beta = 1)$

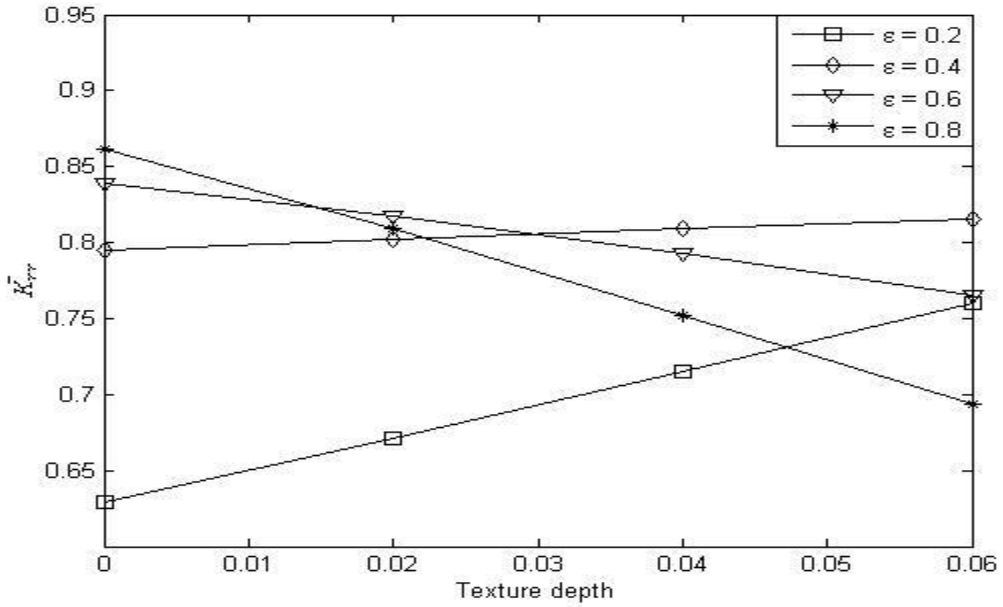

Figure 5.2: Variation of direct stiffness coefficient, $\overline{K}_{rr}$, with texture depth

$(L/D = 1,\ S_p = 0.6,\ \alpha = 1,\ \beta = 1)$

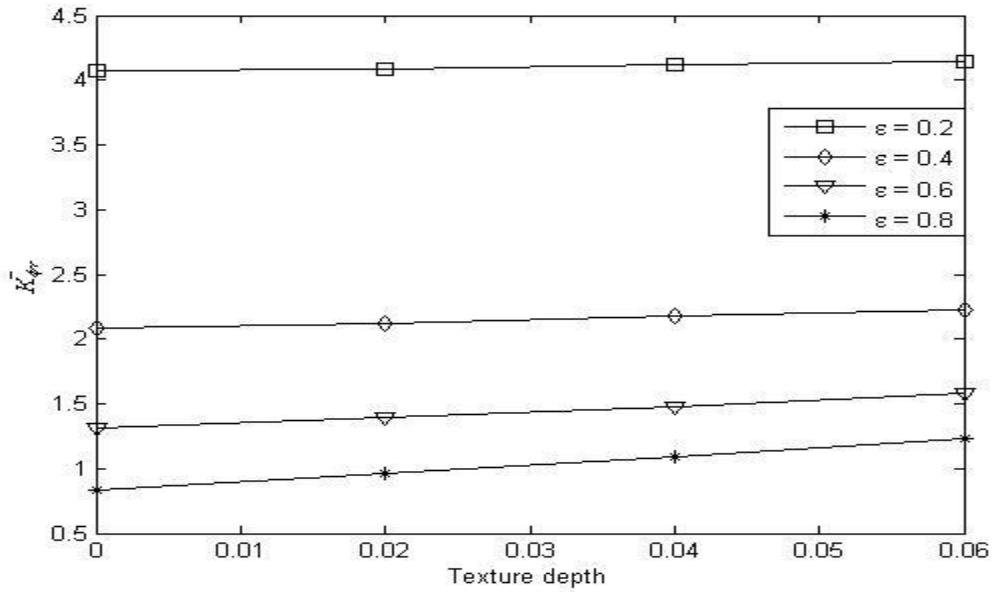

Figure 5.3: Variation of cross-coupled stiffness coefficient, $\overline{K}_{\phi r}$, with texture depth

$(L/D = 1,\ S_p = 0.6,\ \alpha = 1,\ \beta = 1)$

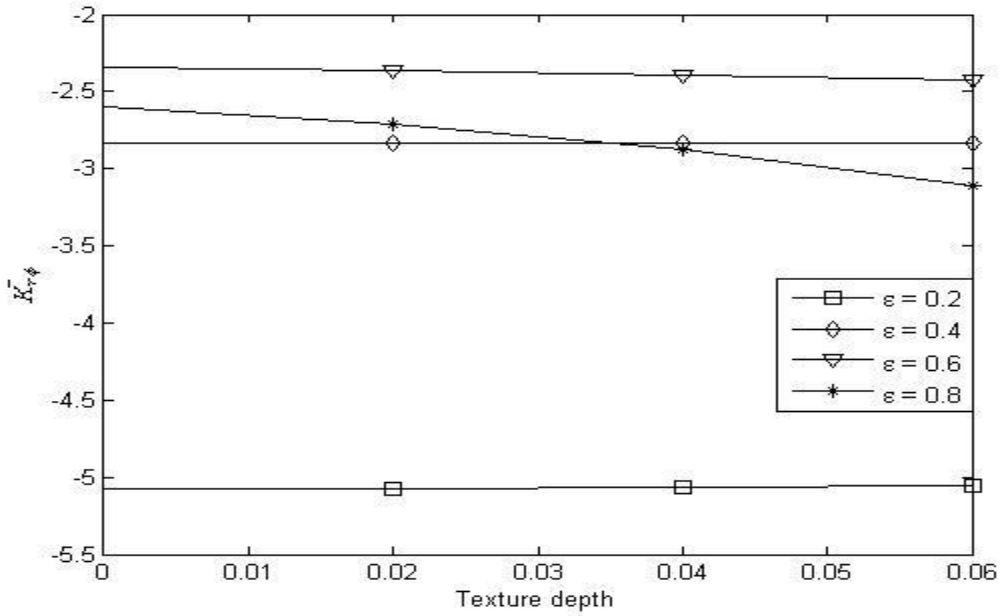

Figure 5.4: Variation of cross-coupled stiffness coefficient, $\overline{K}_{r\phi}$, with texture depth

$(L/D = 1,\ S_p = 0.6,\ \alpha = 1,\ \beta = 1)$

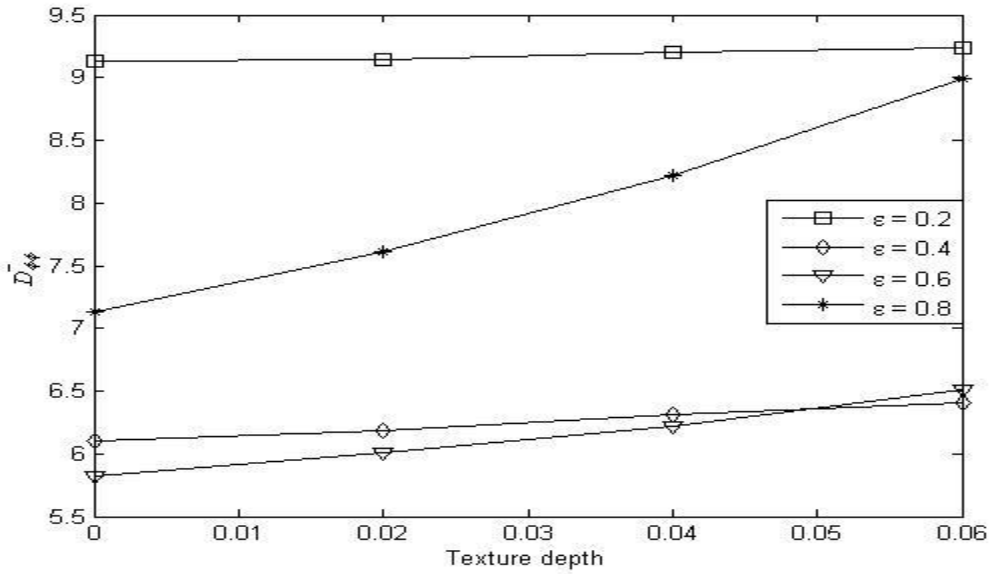

Figure 5.5: Variation of direct damping coefficient, $\bar{D}_{\phi\phi}$, with texture depth

$(L/D = 1,\ S_p = 0.6,\ \alpha = 1,\ \beta = 1)$

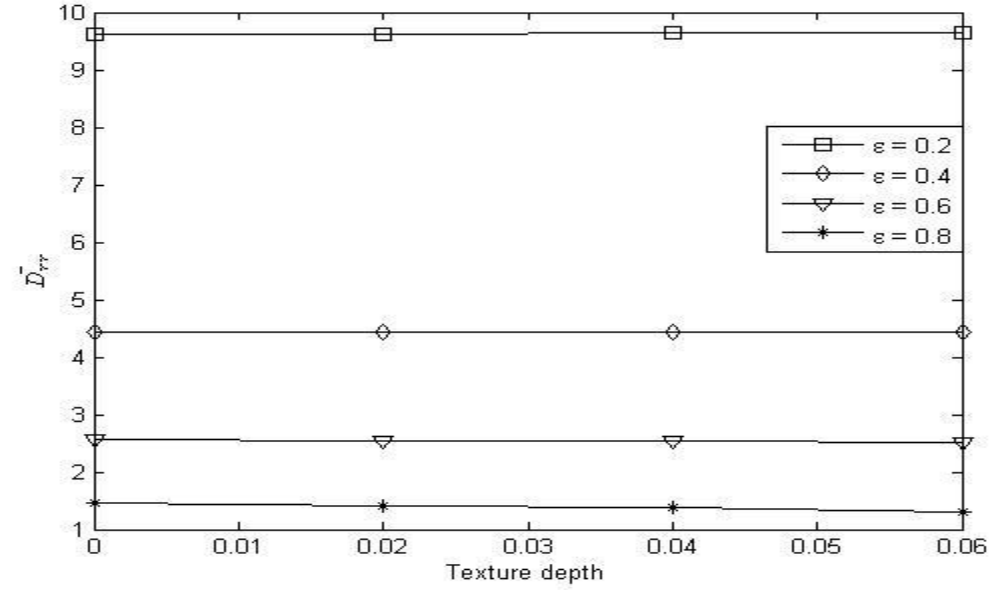

Figure 5.6: Variation of direct damping coefficient, $\bar{D}_{rr}$, with texture depth

$(L/D = 1,\ S_p = 0.6,\ \alpha = 1,\ \beta = 1)$

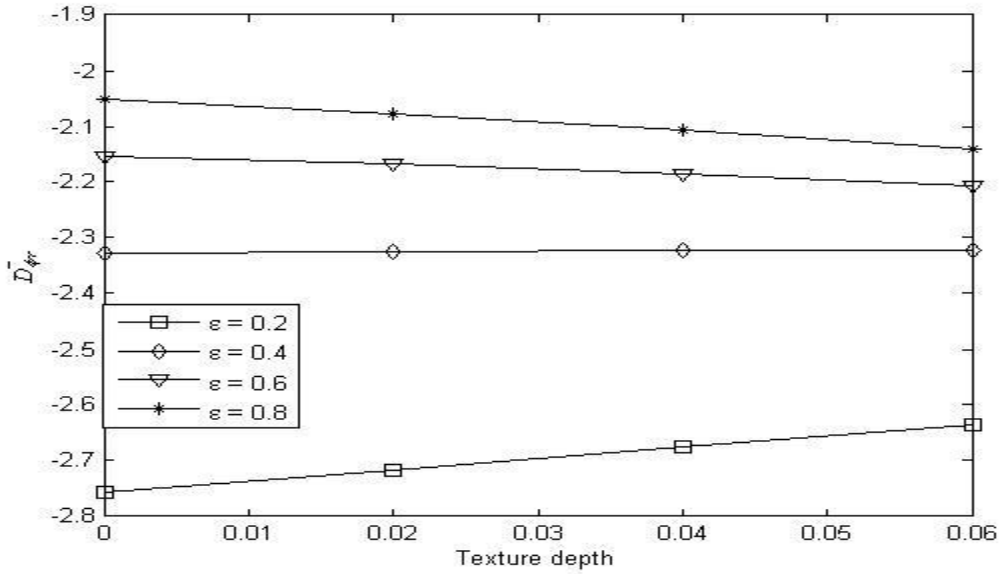

Figure 5.7: Variation of cross-coupled damping coefficient, $\overline{D}_{\phi r}$, with texture depth

$(L/D = 1,\ S_p = 0.6,\ \alpha = 1,\ \beta = 1)$

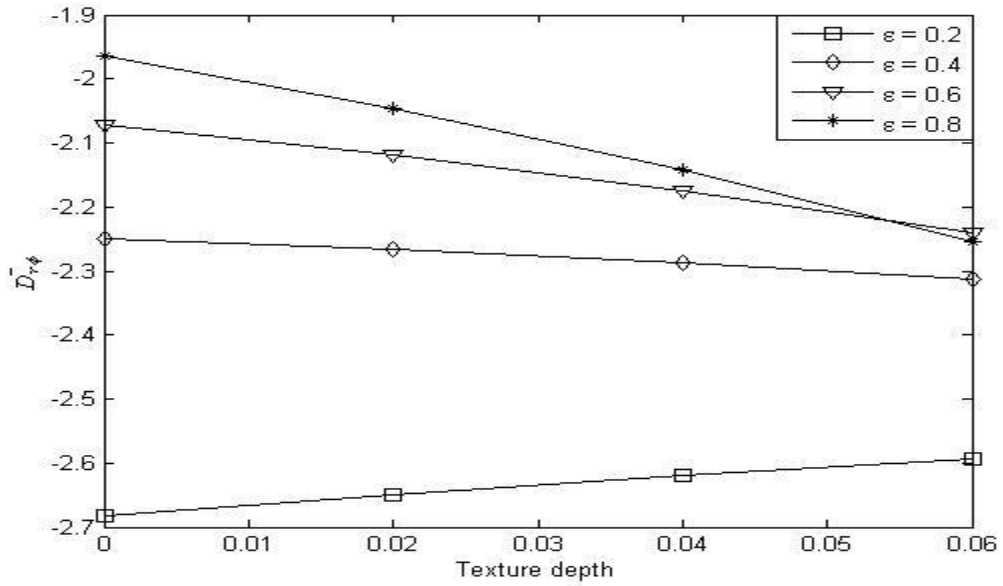

Figure 5.8: Variation of cross-coupled damping coefficient, $\overline{D}_{r\phi}$, with texture depth

$(L/D = 1,\ S_p = 0.6,\ \alpha = 1,\ \beta = 1)$

5.1.2 Effect of texture depth on stability:

The estimated dynamic coefficients at different texture depths are utilized for studying stability of positive cylindrical textured bearing. Mass parameter, a function of operating speed, is estimated along with whirl ratio following the procedure outlined in Chapter 2. The results are presented in Figs. 5.9 and 5.10. Critical mass parameter is a measure of stability. If the operating mass parameter is less than the critical than the journal is stable and if the operating mass parameter is more than the critical, then the journal is unstable. It has been observed that the critical mass parameter increases with increase in eccentricity ratio and it shoots up at higher eccentricity ratios. In view of this the critical mass parameters and corresponding whirl ratios are plotted only for eccentricity ratio up to 0.6 only. Stability improves for eccentricity ratios 0.2 and 0.4 with increase in texture depth, whereas it remains the same except a little improvement at texture depth 0.04. Corresponding whirl ratios are plotted in Fig 5.10 and it is found that whirl ratio remains below 0.5 for all the cases considered, indicating the critical mass parameter corresponds to half-frequency whirling.

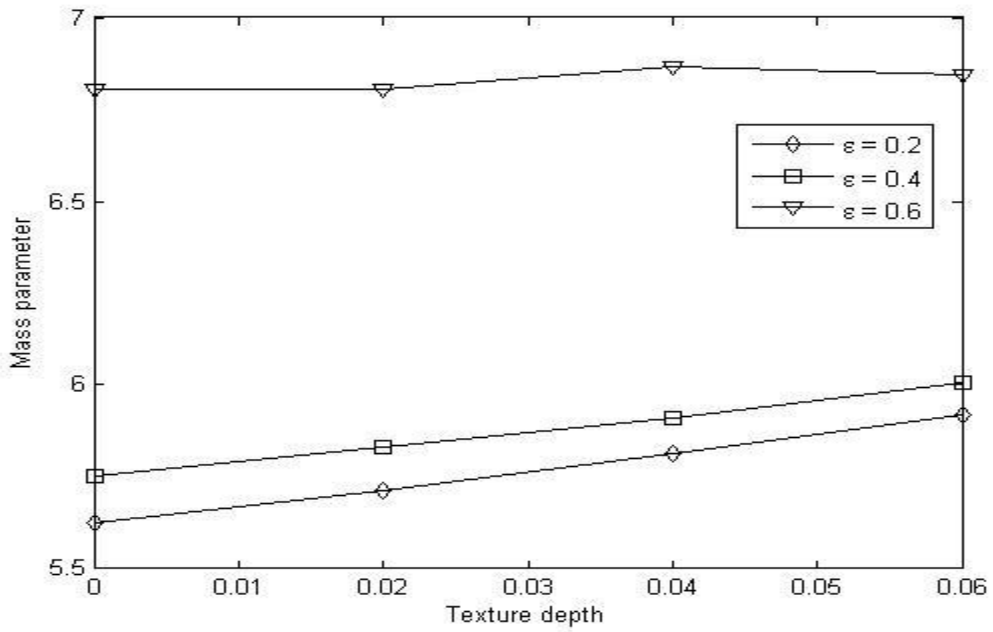

Figure 5.9: Variation of mass parameter with texture depth ($L/D = 1,\ S_p = 0.6,\ \alpha = 1,\ \beta = 1$)

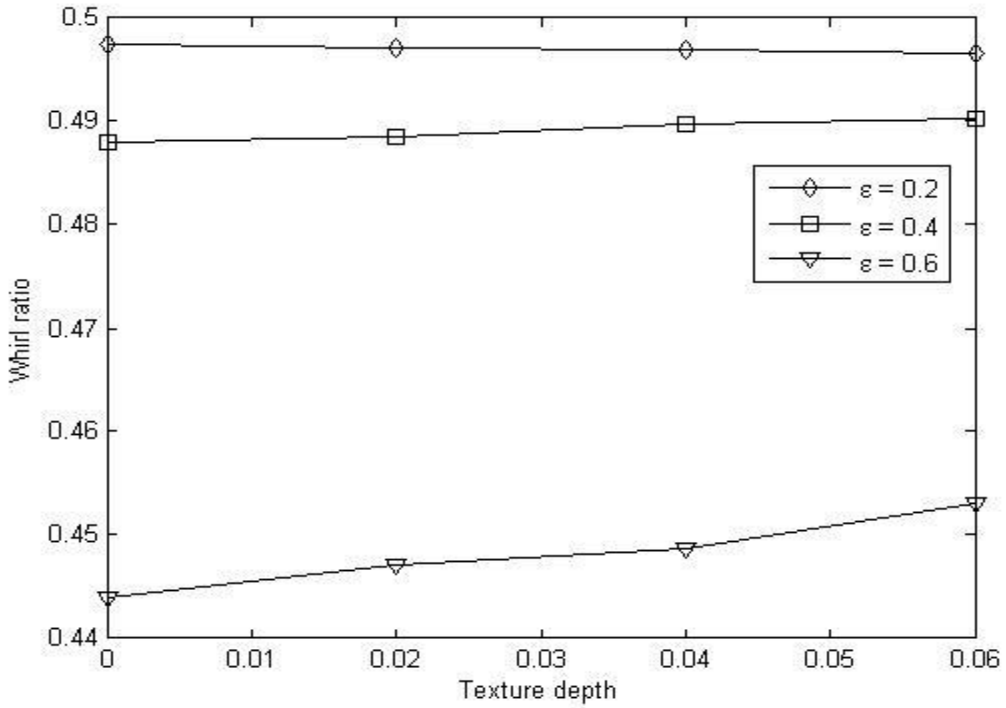

Figure 5.10: Variation of whirl ratio with texture depth ($L/D = 1,\ S_p = 0.6,\ \alpha = 1,\ \beta = 1$)

5.1.3 Effect of eccentricity ratio and texture area density on stiffness and damping coefficients:

Variation of stiffness and damping coefficients with eccentricity ratio is presented here for $L/D = 1,\ \Delta\bar{h} = 0.1,\ \alpha = 1,\ \beta = 1$ and texture area density 0, 0.2, 0.4 and 0.6 in Figs. 5.11 through 5.18. Non-dimensional direct stiffness coefficient, $\overline{K}_{\phi\phi}$ increases with increase in eccentricity ratio for all texture area density considered as seen from Fig. 5.11. However, increase in the parameter is relatively more for texture area density 0.6. On the other hand non-dimensional direct stiffness coefficient, $\overline{K}_{rr}$ behavior is observed to be interesting for different texture area density as depicted in Fig. 5.12. The parameter increases from eccentricity ratio 0.2 to 0.4 for all texture area density and then the increase is slowed down for texture area densities 0 and 0.2 up to eccentricity ratio 0.8. In case of texture area density 0.4, increase in the parameter is slowed down up to eccentricity ratio 0.6 and then remains the same up to eccentricity ratio 0.8. The most interesting result is observed in case of texture area density 0.6 as the parameter starts decreasing little bit from eccentricity ratio 0.4 to 0.8. Besides the value of the stiffness

coefficient at eccentricity ratio 0.2 is more than the values for texture area density 0 and 0.2, when it is less than the value corresponding to texture area density 0.4. Moreover, the value of the coefficient for texture area density 0.6 is the lowest at eccentricity ratio 0.8 compared to other texture area densities. It has been observed from Fig. 5.13 that the non-dimensional cross-coupled stiffness coefficient, $\overline{K}_{\phi r}$ decreases with increase in eccentricity ratio for all texture area densities considered and higher the texture area density the coefficient is also marginally higher. The non-dimensional cross-coupled stiffness, $\overline{K}_{r\phi}$, increases sharply from eccentricity ratio 0.2 to 0.4 and then increment slows down up to eccentricity ratio 0.6 and finally it dips a little up to eccentricity ratio 0.8 for all texture area density considered as evident from Fig. 5.14. The parameter remains the same for all texture area densities from eccentricity ratio 0.2 to 0.6 and it is found to be less for texture area density 0.6 from eccentricity ratio 0.6 to 0.8 compared to other texture area densities. It has been observed from Fig. 5.15 that the non-dimensional direct damping coefficient, $\overline{D}_{\phi\phi}$, initially get decreased from eccentricity ratio 0.2 to 0.4 and then rate of decrease slows down up to eccentricity ratio 0.6 and finally it increases from eccentricity ratio 0.6 to 0.8 for texture area density 0, 0.2, 0.4. When texture area density is 0.6, the parameter initially decreases from eccentricity ratio 0.2 to 0.4, but then there is an increase from eccentricity ratio 0.4 to 0.6 and finally the rate of increase is rapid from eccentricity ratio 0.6 to 0.8. On the other hand, the non-dimensional direct damping coefficient $\overline{D}_{rr}$ decreases with increase in eccentricity ratio for all texture area densities considered. However, texture area density has no effect on the parameter as observed from Fig. 5.16. The non-dimensional cross-coupled damping coefficients, $\overline{D}_{\phi r}$ and $\overline{D}_{r\phi}$ increase with increase in eccentricity ratio as seen from Figs 5.17 and 5.18. However, the effect of texture area density on the parameter is not uniform in all the cases. The sequence of largest to smallest $\overline{D}_{\phi r}$ are found to be for texture area density of 0.6 & 0.4, 0, 0.2 at eccentricity ratio 0.2, for texture area density of 0.4, 0 & 0.6, 0.2 at eccentricity ratio 0.4, for texture area density of 0.4, 0 & 0.6, 0.2 at eccentricity ratio 0.6, for texture area density of 0.4, 0 & 0.2, 0.6 at eccentricity ratio 0.8. Similarly The sequence of largest to smallest for $\overline{D}_{r\phi}$ are found to be for texture area density 0.4, 0.6, 0, 0.2 at eccentricity ratio 0.2, for texture area density 0.4, 0 & 0.2, 0.6 at eccentricity ratio 0.4, for texture area density 0.4, 0.2, 0, 0.6 at eccentricity ratio 0.6 and for texture area density 0.2, 0.4, 0, 0.6 at eccentricity ratio 0.8.

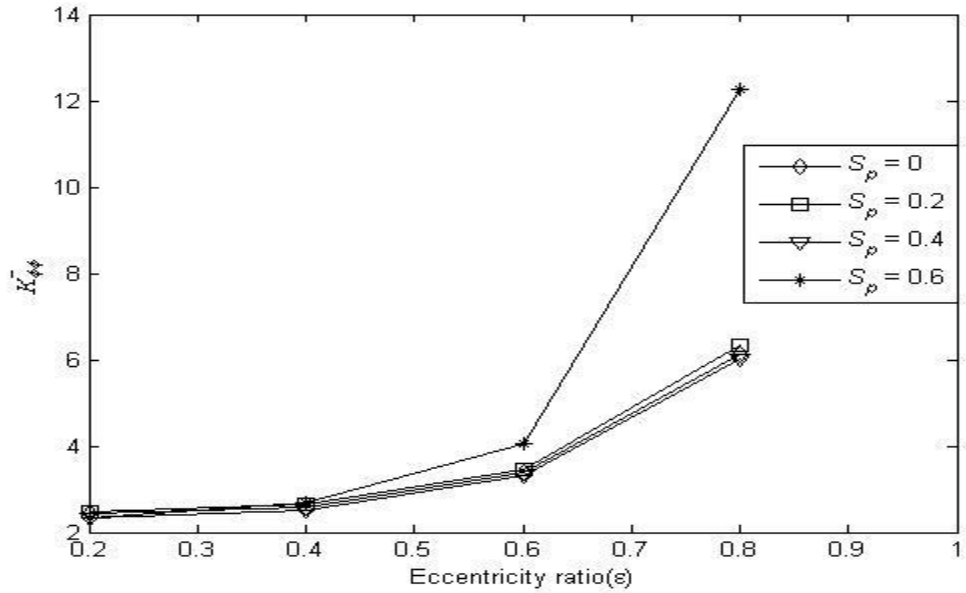

Figure 5.11: Variation of direct stiffness coefficient, $\overline{K}_{\phi\phi}$, with eccentricity ratio

$(L/D = 1,\ \Delta\bar{h} = 0.1,\ \alpha = 1,\ \beta = 1)$

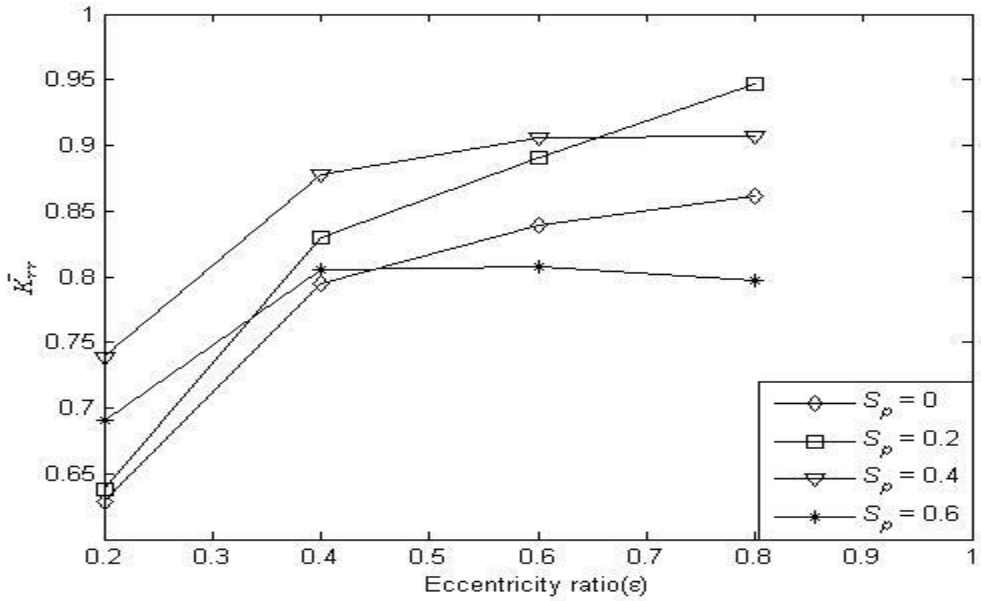

Figure 5.12: Variation of direct stiffness coefficient, $\overline{K}_{rr}$, with eccentricity ratio

$(L/D = 1,\ \Delta\bar{h} = 0.1,\ \alpha = 1,\ \beta = 1)$

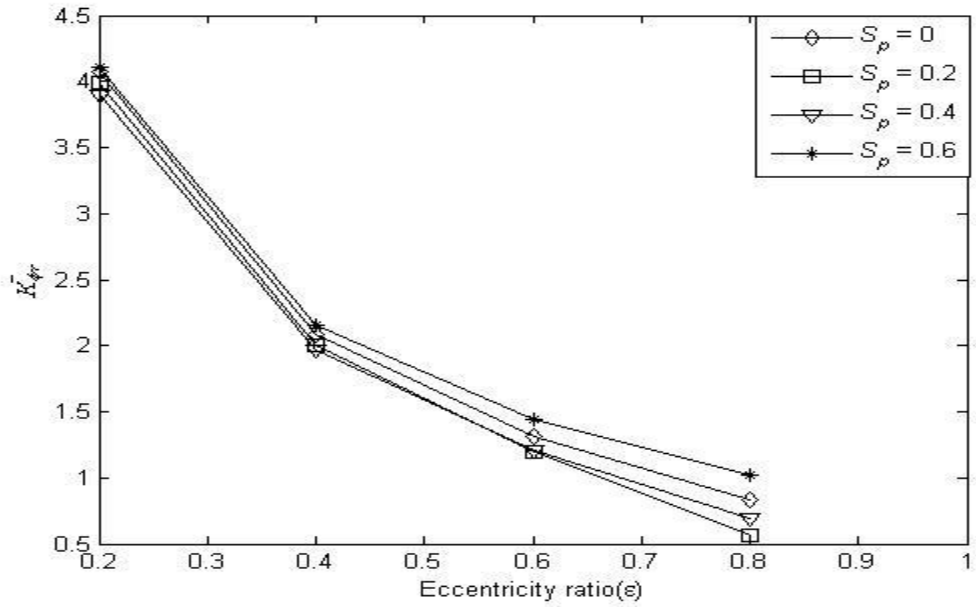

Figure 5.13: Variation of cross-coupled stiffness coefficient, $\overline{K}_{\phi r}$, with eccentricity ratio

$(L/D = 1,\ \Delta\bar{h} = 0.1,\ \alpha = 1,\ \beta = 1)$

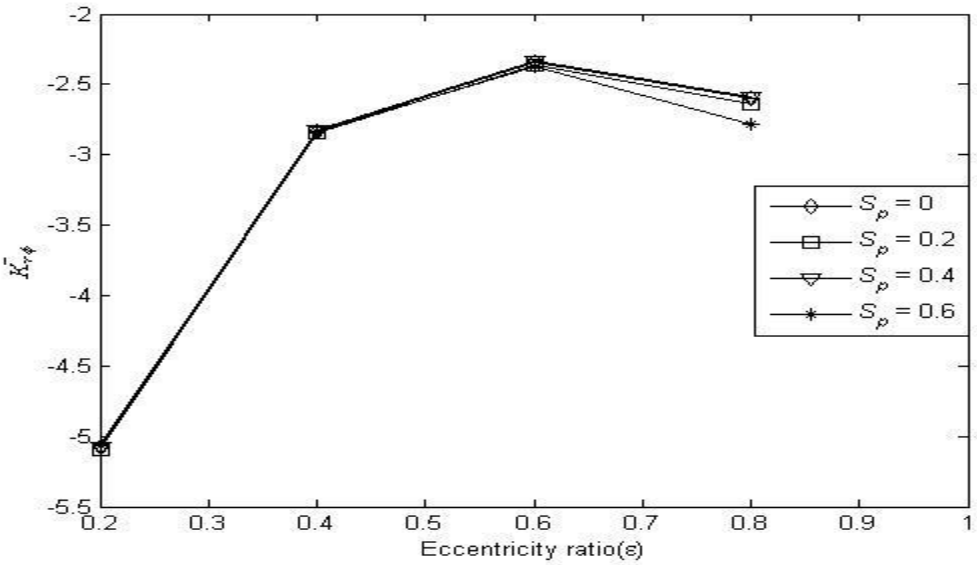

Figure 5.14: Variation of cross-coupled stiffness coefficient, $\overline{K}_{r\phi}$, with eccentricity ratio

$(L/D = 1,\ \Delta\bar{h} = 0.1,\ \alpha = 1,\ \beta = 1)$

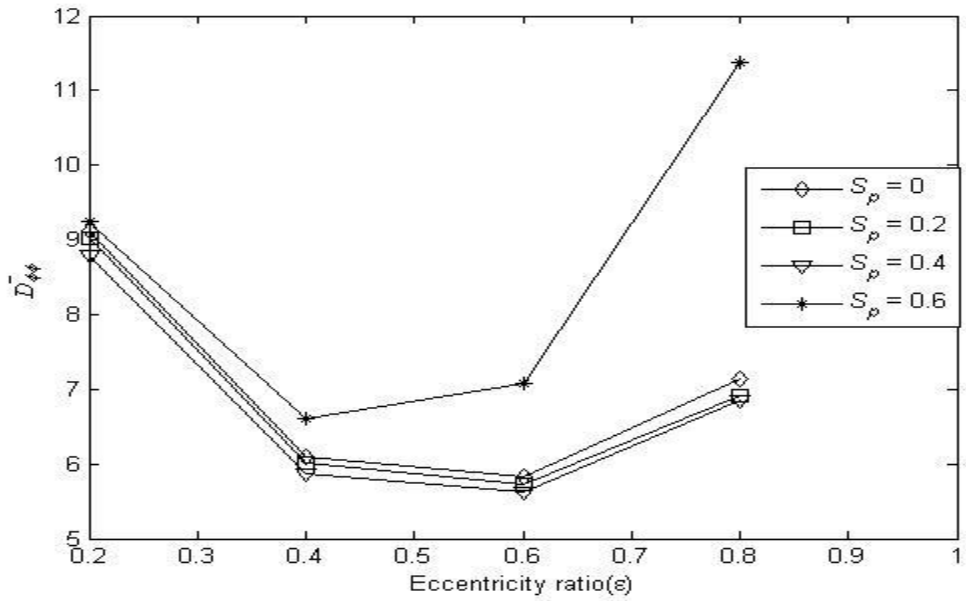

Figure 5.15: Variation of direct damping coefficient, $\bar{D}_{\phi\phi}$, with eccentricity ratio

$(L/D = 1,\ \Delta\bar{h} = 0.1,\ \alpha = 1,\ \beta = 1)$

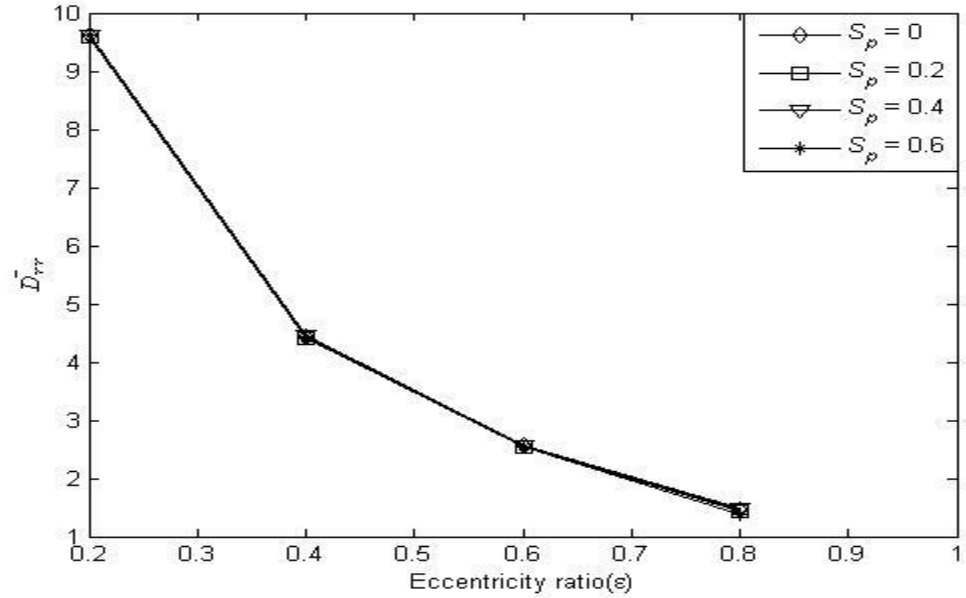

Figure 5.16: Variation of direct damping coefficient, $\bar{D}_{rr}$, with eccentricity ratio

$(L/D = 1,\ \Delta\bar{h} = 0.1,\ \alpha = 1,\ \beta = 1)$

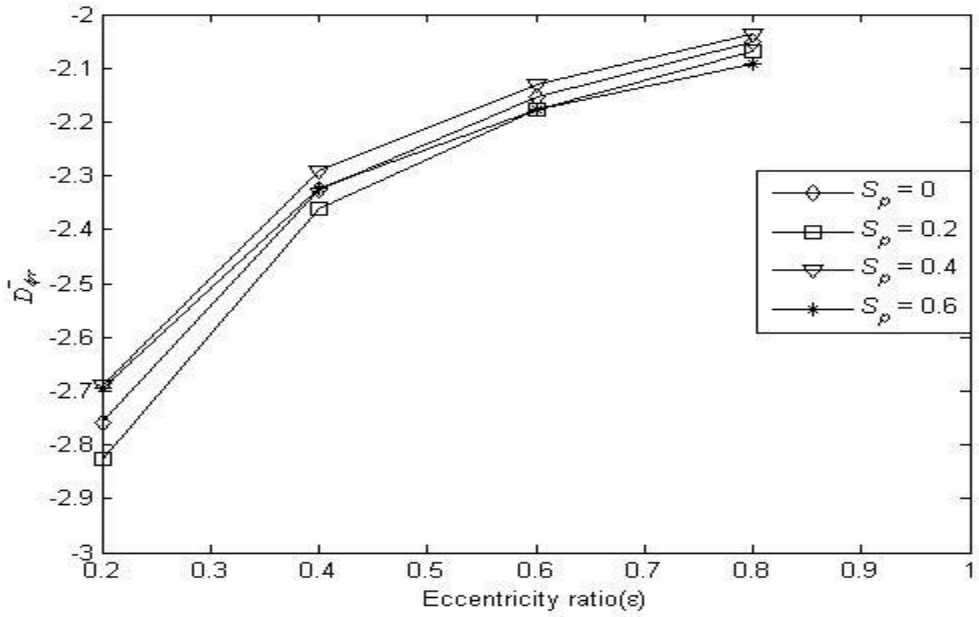

Figure 5.17: Variation of cross-coupled damping coefficient, $\bar{D}_{\phi r}$, with eccentricity ratio

$(L/D = 1,\ \Delta\bar{h} = 0.1,\ \alpha = 1,\ \beta = 1)$

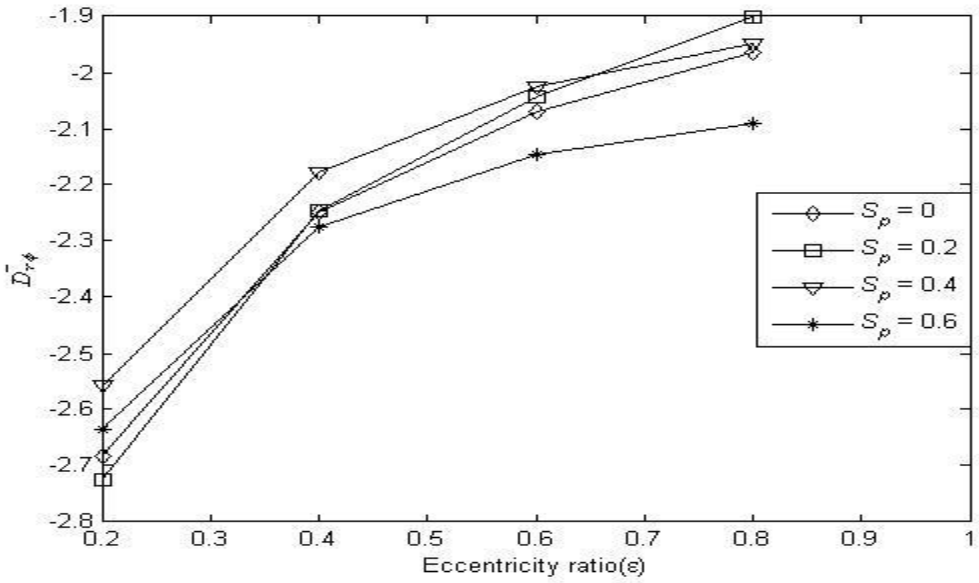

Figure 5.18: Variation of cross-coupled damping coefficient, $\bar{D}_{r\phi}$, with eccentricity ratio

$(L/D = 1,\ \Delta\bar{h} = 0.1,\ \alpha = 1,\ \beta = 1)$

5.1.4 Effect of eccentricity ratio on stability:

The estimated dynamic coefficients at different eccentricity ratios and texture area densities are utilized for estimating mass parameter and whirl ratio to study stability of positive cylindrical textured bearing following the procedure outlined in Chapter 2. The results are presented in Figs. 5.19 and 5.20. As mentioned earlier it has been observed that the critical mass parameter increases with increase in eccentricity ratio and it shoots up at higher eccentricity ratios. In view of this the critical mass parameters and corresponding whirl ratios are plotted for eccentricity ratio up to 0.6 only. It has been inferred from Fig. 5.19 that journal is better stable with texture area density 0.6 between eccentricity ratios 0.2 to 0.3, whereas stability is better for texture area density 0.4 between eccentricity ratios 0.3 to 0.5. Beyond eccentricity ratio 0.5, stability improves for texture area density 0.2. Overall, stability improves for textured bearing as stability of un-textured bearing (texture area density 0.0) is observed to be the minimum. Corresponding whirl ratios are plotted in Fig 5.20 and it is found that whirl ratio remains below 0.5 for all the cases considered, indicating the critical mass parameters correspond to half-frequency whirling.

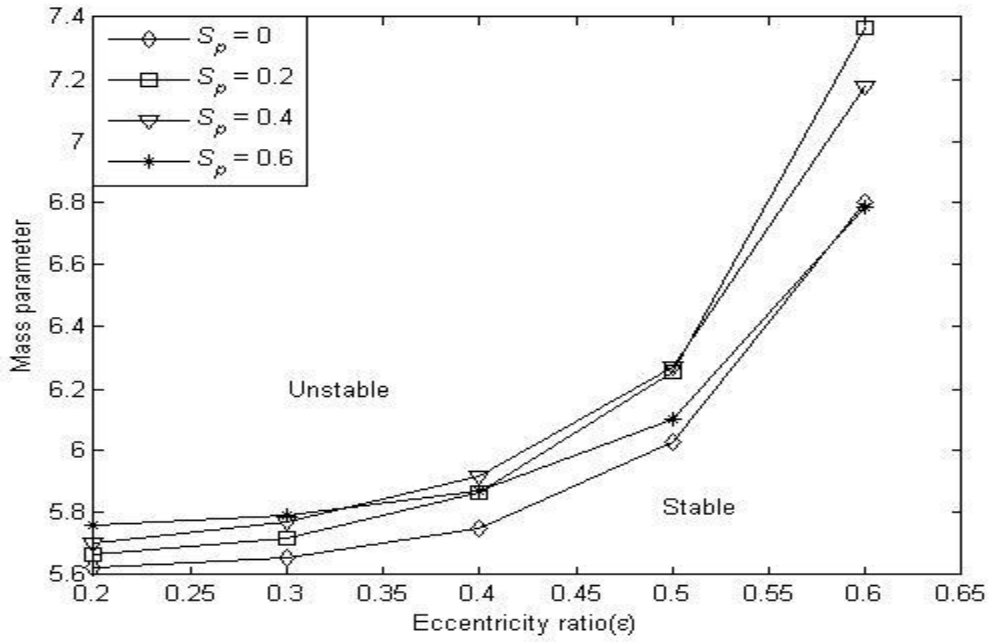

Figure 5.19: Variation of mass parameter with eccentricity ratio

$(L/D = 1,\ \Delta\bar{h} = 0.1,\ \alpha = 1,\ \beta = 1)$

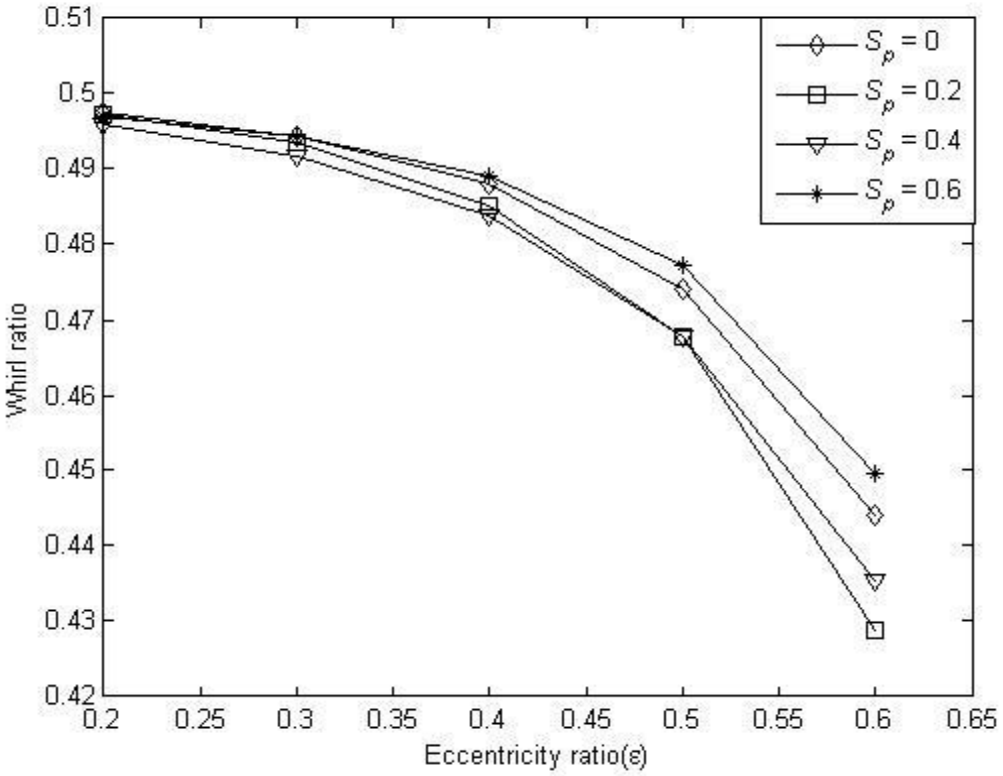

Figure 5.20: Variation of whirl ratio with eccentricity ratio ($L/D = 1,\ \Delta\bar{h} = 0.1,\ \alpha = 1,\ \beta = 1$)

5.1.5 Effect of textured portion in circumferential direction on stiffness and damping coefficients:

Textured portion in circumferential direction is varied keeping the axial direction fully textured for $L/D = 1,\ S_p = 0.6,\ \Delta\bar{h} = 0.1$ to study the effect of textured portion in the circumferential direction on dynamic characteristics. The results are presented in Figs. 5.21 through 5.28. It has been observed that the non-dimensional direct stiffness coefficient, $\overline{K}_{\phi\phi}$ increases from 40% textured portion to 60% textured portion for eccentricity ratio 0.8 and 0.6. The increase is almost double for eccentricity ratio 0.8, when the increase is not much significant at eccentricity ratio 0.6. The parameter is not at all affected due to variation of textured portion in all other cases considered. Further it has been observed from Fig. 5.22 that the non-dimensional direct stiffness coefficient, $\overline{K}_{rr}$, increases initially from un-textured condition to 40% textured portion, then it

decreases up to 60% textured condition and finally it remains constant until fully textured condition is arrived at for all eccentricity ratios considered slightly with increase texture portion. From Fig 5.23 it is observed that the non-dimensional cross-coupled stiffness coefficient $\overline{K}_{\phi r}$ decreases with increase in texture portion from 20% to 40% textured portion, then it increases up to 60% textured portion and finally remains constant up to fully textured condition in axial direction. It has been noticed from Fig 5.24 that the cross-coupled stiffness coefficient, $\overline{K}_{r\phi}$ is not affected by variation of textured portion in axial direction for eccentricity ratios 0.2 and 0.4. However, it decreases from 40% to 60% textured portion for eccentricity ratios 0.6 and 0.8. Interestingly the stiffness coefficient remains maximum for eccentricity ratio 0.6 from un-textured to fully textured condition and there is a sharp decrease in it for eccentricity ratio 0.8 from 40% to 60% textured portion. The non-dimensional direct damping coefficient, $\overline{D}_{\phi\phi}$, decreases from 20% to 40% textured condition and then increases from 40% to 60% textured condition and remains constant beyond 60% to fully textured condition in circumferential direction as seen from Fig 5.25. There is a sharp increase in the parameter from 40% to 60% textured condition for eccentricity ratio 0.8 compared to other eccentricity ratios considered. On the other hand the effect of texture portion in circumferential direction on the non-dimensional direct damping coefficient $\overline{D}_{rr}$ is not significant for all the eccentricity ratios except for 0.8. There is a slight decrease in the coefficient from 40% to 60% textured portion for eccentricity ratio 0.8 as seen in Fig.5.26. The non-dimensional cross-coupled damping coefficients are plotted in Figs. 5.27 and 5.28. $\overline{D}_{\phi r}$ and $\overline{D}_{r\phi}$ increase from un-textured condition to 40% textured condition and then decrease from 40% to 60% textured condition and finally remain constant up to fully textured condition as seen in these figures. Only difference is that when the variation of $\overline{D}_{\phi r}$ with textured portion is almost identical for all the eccentricity ratios, it is not so for $\overline{D}_{r\phi}$.

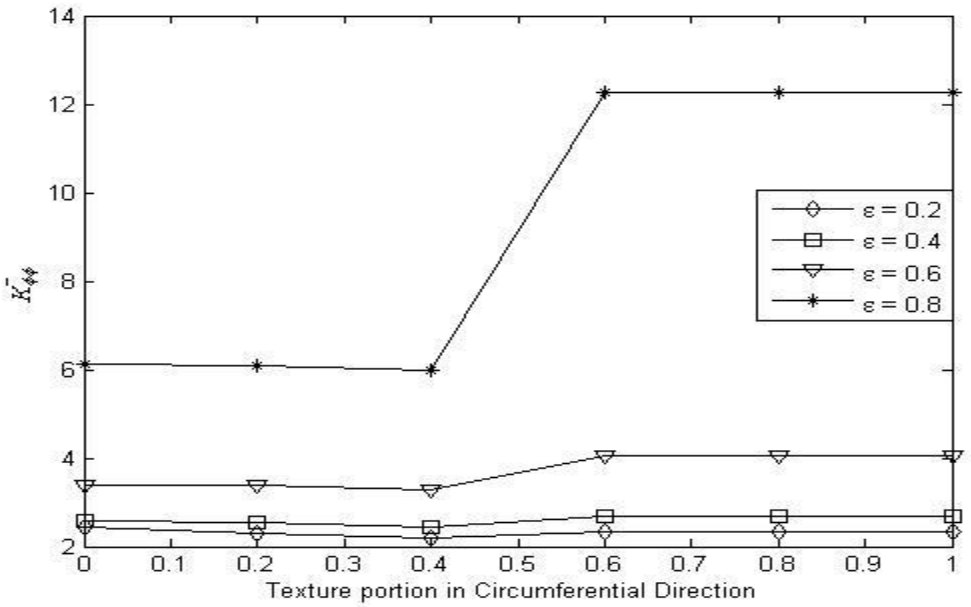

Figure 5.21: Effect of textured portion in circumferential direction on direct stiffness coefficient, $\overline{K}_{\phi\phi}$, of cylindrical textured journal bearing ($L/D = 1,\ S_p = 0.6,\ \Delta\bar{h} = 0.1,\ \beta = 1$)

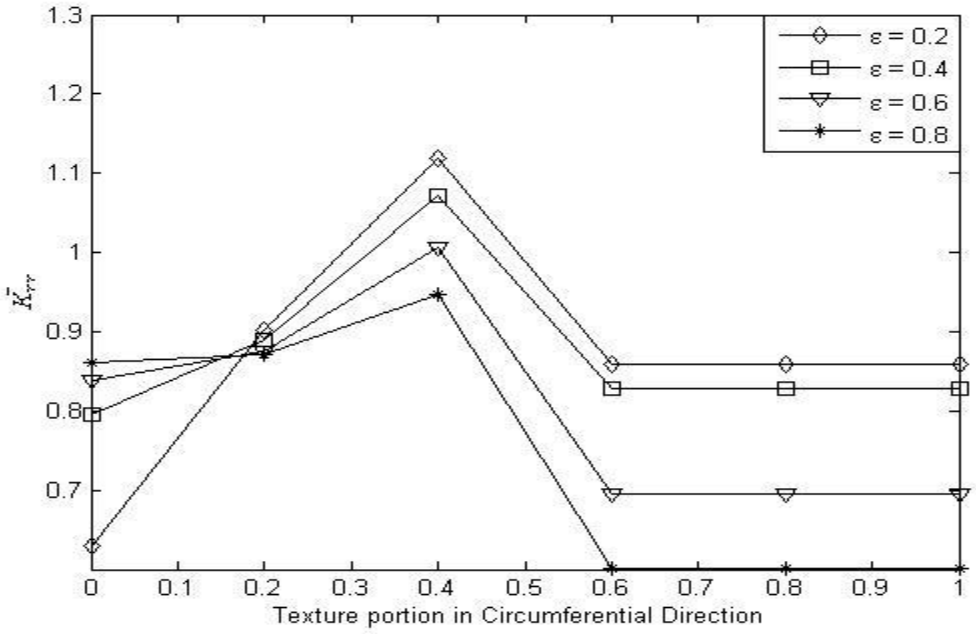

Figure 5.22: Effect of textured portion in circumferential direction on direct stiffness coefficient, $\overline{K}_{rr}$, of cylindrical textured journal bearing ($L/D = 1,\ S_p = 0.6,\ \Delta\bar{h} = 0.1,\ \beta = 1$)

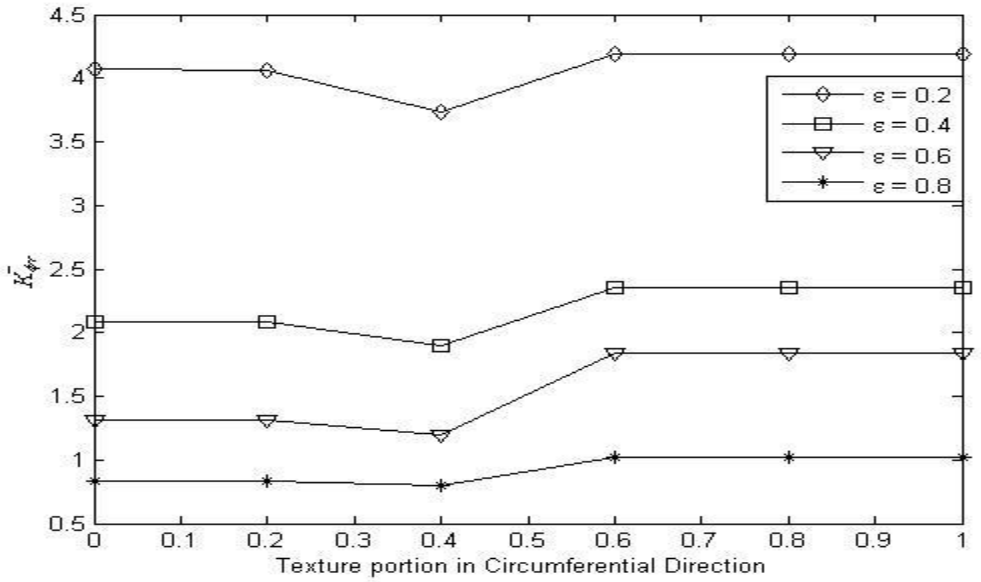

Figure 5.23: Effect of textured portion in circumferential direction on cross-coupled stiffness coefficient, $\overline{K}_{\phi r}$, of cylindrical textured journal bearing ($L/D = 1,\ S_p = 0.6,\ \Delta\overline{h} = 0.1,\ \beta = 1$)

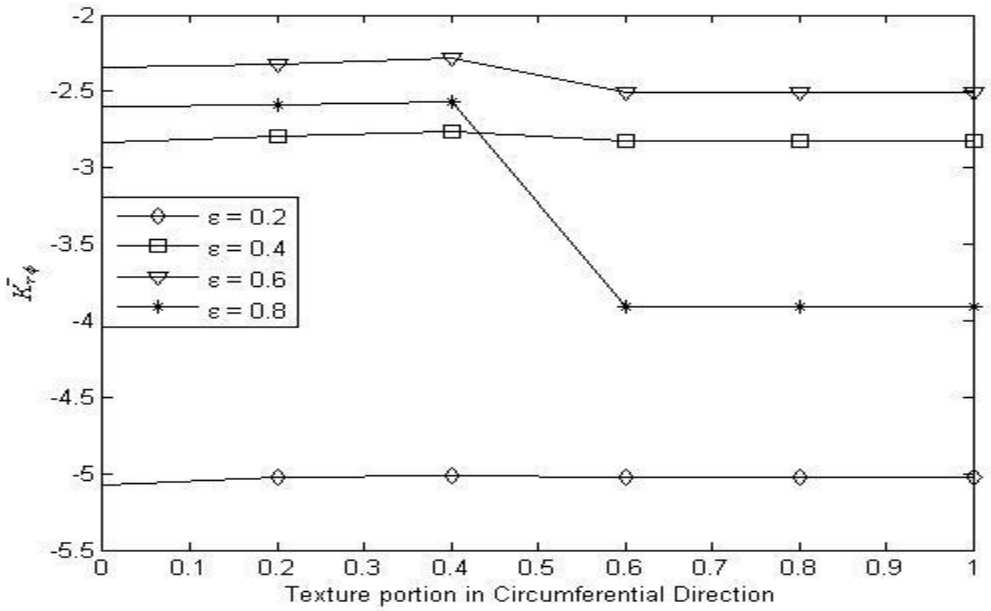

Figure 5.24: Effect of textured portion in circumferential direction on cross-coupled stiffness coefficient, $\overline{K}_{r\phi}$, of cylindrical textured journal bearing ($L/D = 1,\ S_p = 0.6,\ \Delta\overline{h} = 0.1,\ \beta = 1$)

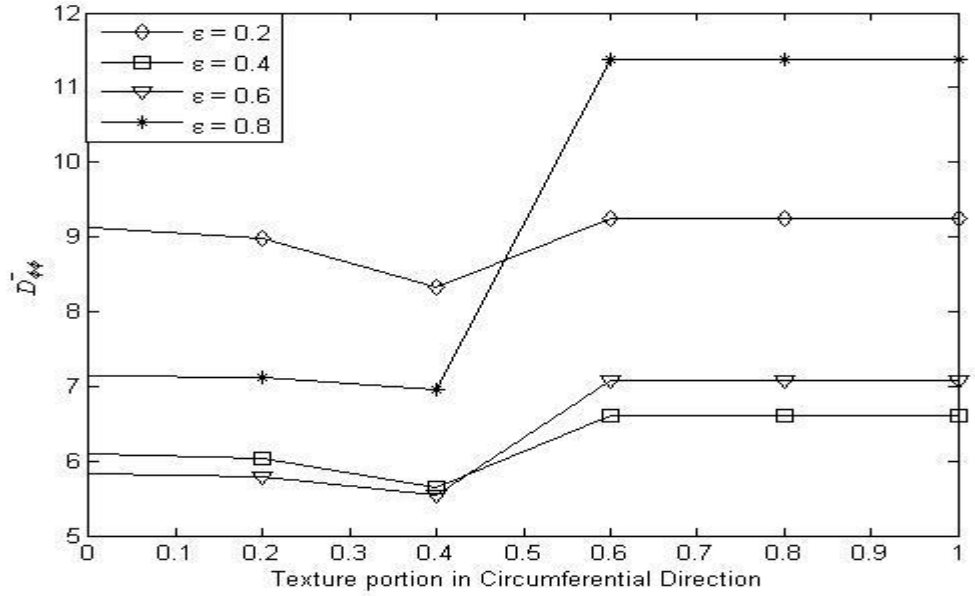

Figure 5.25: Effect of textured portion in circumferential direction on direct damping coefficient, $\overline{D}_{\phi\phi}$, of cylindrical textured journal bearing ($L/D = 1,\ S_p = 0.6,\ \Delta\bar{h} = 0.1,\ \beta = 1$)

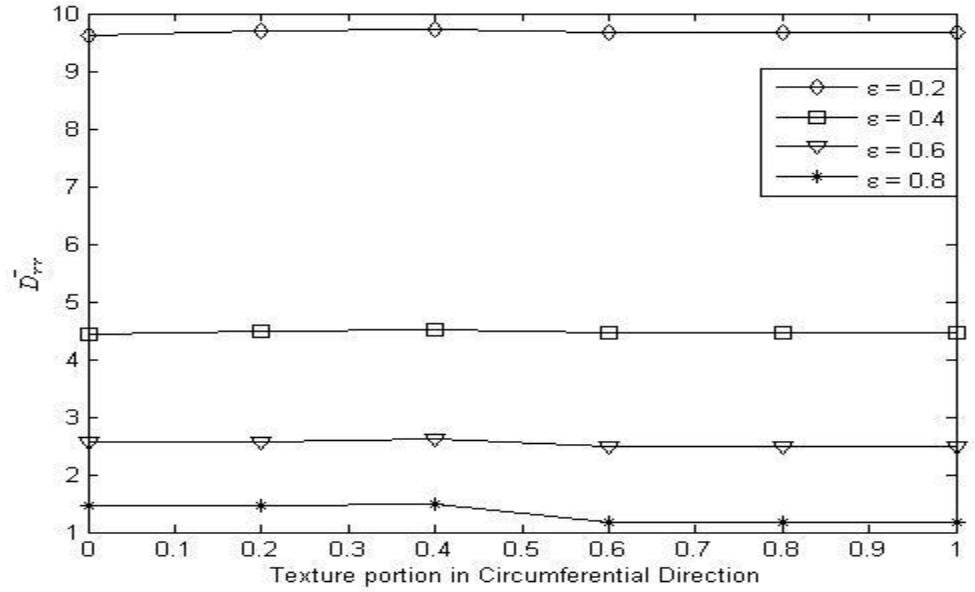

Figure 5.26: Effect of textured portion in circumferential direction on direct damping coefficient, $\overline{D}_{rr}$, of cylindrical textured journal bearing ($L/D = 1,\ S_p = 0.6,\ \Delta\bar{h} = 0.1,\ \beta = 1$)

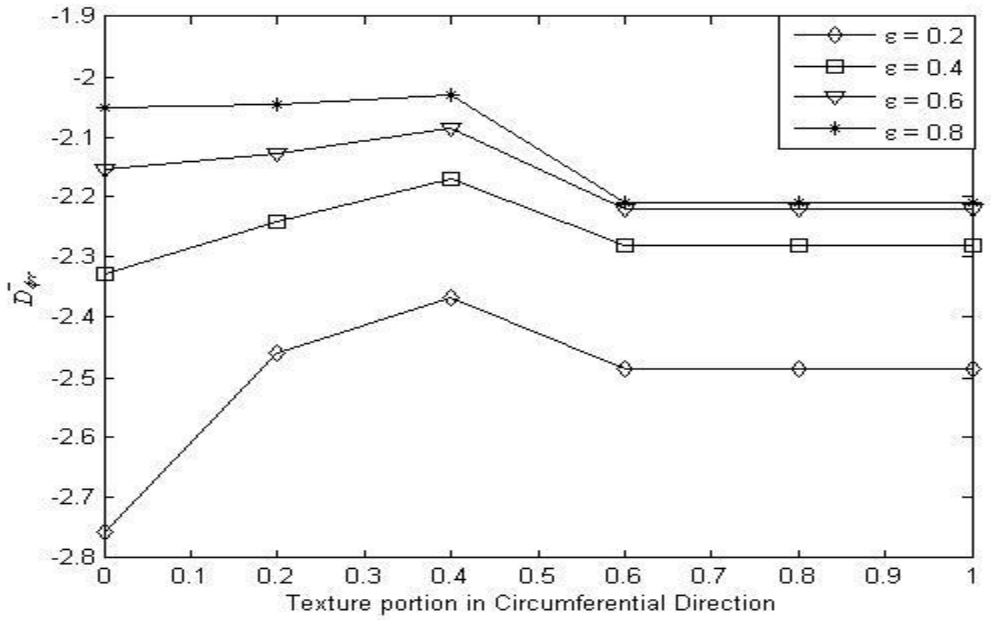

Figure 5.27: Effect of textured portion in circumferential direction on cross-coupled stiffness coefficient, $\overline{D}_{\phi r}$, of cylindrical textured journal bearing ($L/D = 1,\ S_p = 0.6,\ \Delta\bar{h} = 0.1,\ \beta = 1$)

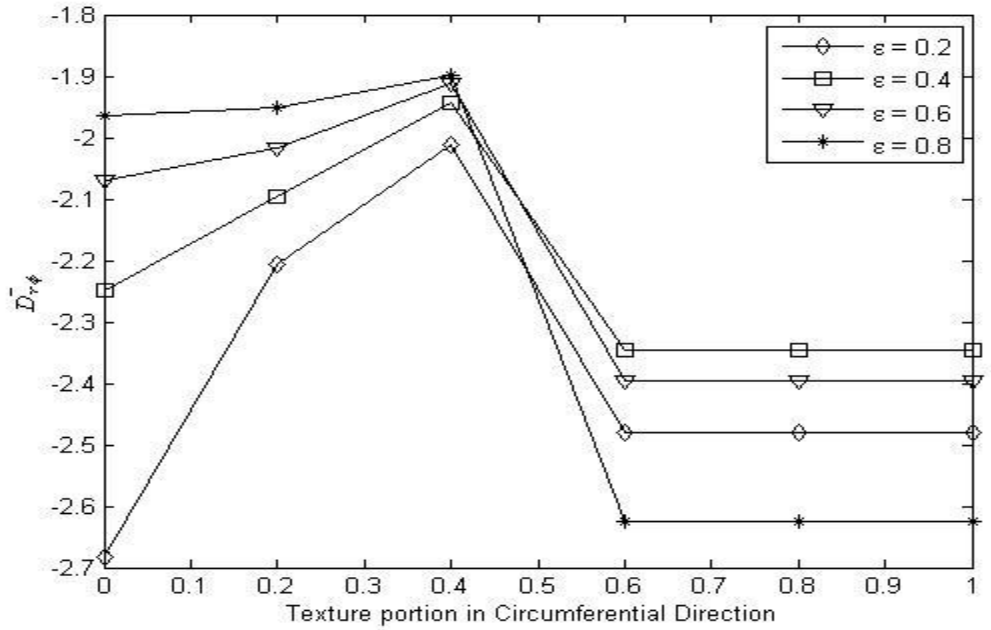

Figure 5.28: Effect of textured portion in circumferential direction on cross-coupled stiffness coefficient, $\overline{D}_{r\phi}$, of cylindrical textured journal bearing ($L/D = 1,\ S_p = 0.6,\ \Delta\bar{h} = 0.1,\ \beta = 1$)

5.1.6 Effect of textured portion in circumferential direction on stability:

From Fig 5.29 it is observed that the critical mass parameter increases with increase in texture portion from un-textured condition up to 40% textured condition, then decreases up to 60% textured condition and finally remains constant up to fully textured condition in circumferential direction. Corresponding whirl ratios are plotted in Fig 5.30 and it has been observed that all the whirl ratios are below 0.5 affirming half-frequency whirling.

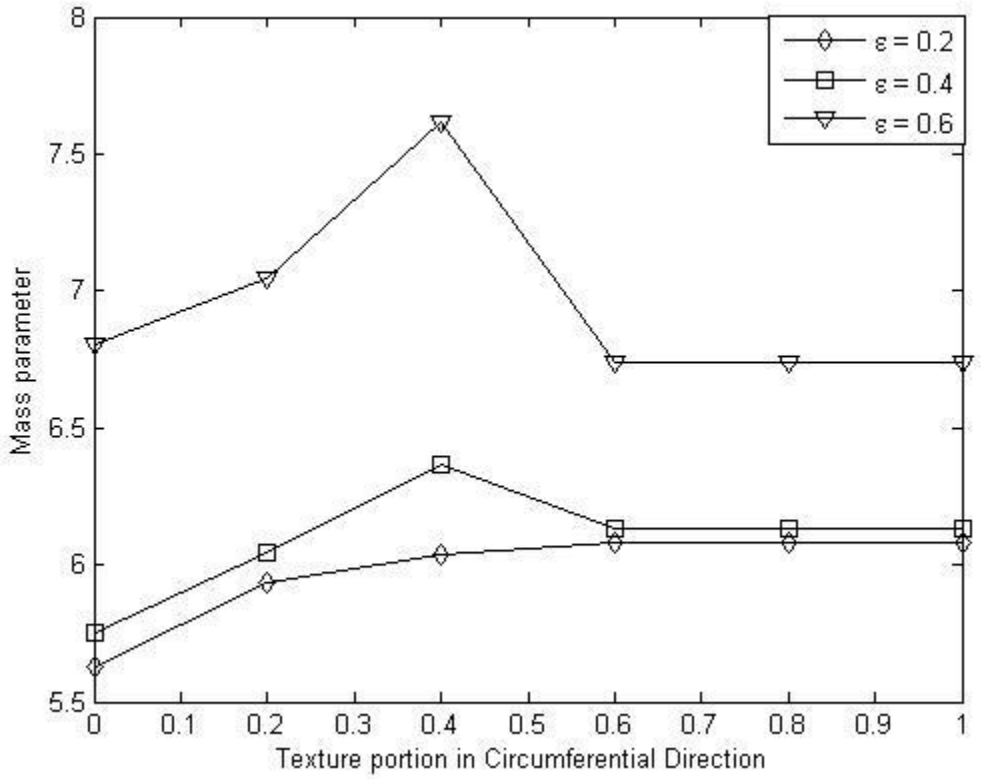

Figure 5.29: Effect of textured portion in circumferential direction on mass parameter of cylindrical textured journal bearing ($L/D = 1,\ S_p = 0.6,\ \Delta\bar{h} = 0.1,\ \beta = 1$)

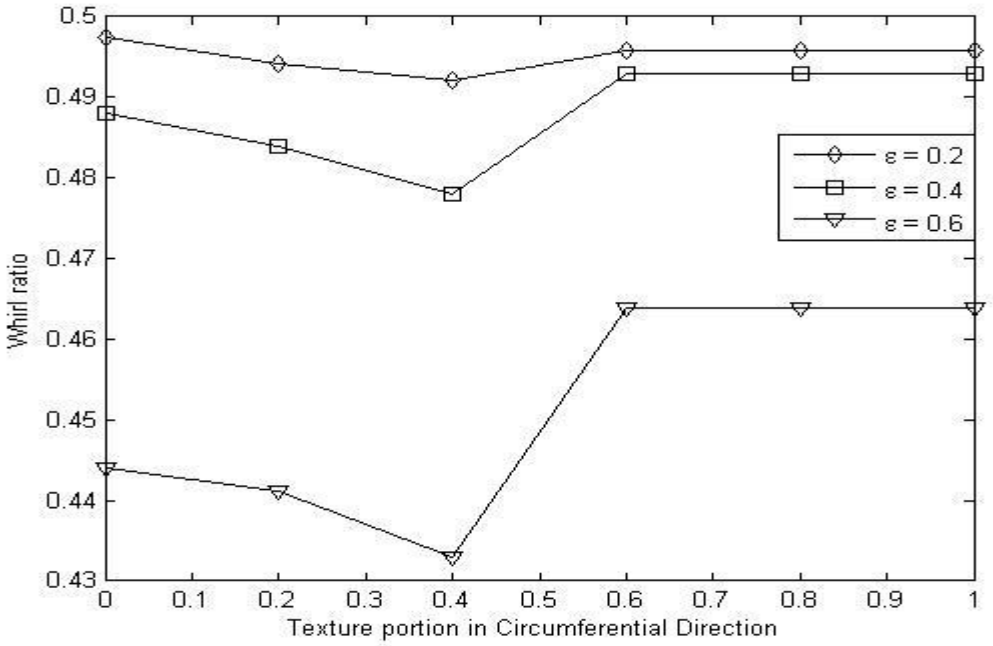

Figure 5.30: Effect of textured portion in circumferential direction on whirl ratio of cylindrical textured journal bearing ($L/D = 1,\ S_p = 0.6,\ \Delta\bar{h} = 0.1,\ \beta = 1$)

5.1.7 Effect of textured portion in axial direction on stiffness and damping coefficients:

Four stiffness and four damping coefficients are estimated by varying textured portion in axial direction and keeping the circumferential direction fully textured for $L/D = 1,\ S_p = 0.6,\ \Delta\bar{h} = 0.1$. The results are presented in Figs. 5.31 through 5.38. The non-dimensional direct stiffness coefficients, $\overline{K}_{\phi\phi}$, increases from 20% textured condition to fully textured condition in axial direction for eccentricity ratio 0.8 as seen in Fig. 5.31. However, the parameter is least affected by variation of textured portion in axial direction for other eccentricity ratios considered here. The other non-dimensional direct stiffness coefficient, $\overline{K}_{rr}$, increases for eccentricity ratio 0.2, remains almost constant for 0.4 and decrease for 0.6 and 0.8 as depicted in Fig. 5.32. The non-dimensional cross-coupled stiffness coefficient, $\overline{K}_{\phi r}$, increases slightly for eccentricity ratios 02, 04 and 0.6, when there is a sharp increase in the coefficient from 20% to 40% textured portion in axial direction for eccentricity ratio 0.8 as seen in Fig. 5.33. On the other hand, it has been seen from Fig. 5.34 that the non-dimensional cross-coupled stiffness, $\overline{K}_{r\phi}$, decreases steadily from

20% textured portion to fully textured condition in axial direction for eccentricity ratio 0.8, when the coefficient remains almost unaffected for all other eccentricity ratios considered here. The non-dimensional direct damping coefficient, $\overline{D}_{\phi\phi}$, increases slightly from 20% textured portion onward for eccentricity ratio 0.6, increases rapidly from 20% textured portion onward for eccentricity ratio 0.8 and the coefficient is not affected much for eccentricity ratios 0.2 and 0.4 as observed from Fig. 5.35. The other non-dimensional direct damping coefficient, $\overline{D}_{rr}$, has been found to be not affected by the variation of textured portion in axial direction as seen in Fig. 5.36. The non-dimensional cross-coupled damping coefficient, $\overline{D}_{\phi r}$, increases from 20% to 60% textured portion for eccentricity ratio 0.2, from 20% to 40% textured portion for eccentricity ratio 0.4, decreases slightly from 40% onward for eccentricity ratio 0.6 and decreases from 20% textured portion onward for eccentricity ratio 0.8 as depicted in Fig. 5.37. The other non-dimensional cross-coupled damping coefficient, $\overline{D}_{r\phi}$, increases from 20% to 60% textured portion for eccentricity ratio 0.2, decreases slightly from 20% textured portion onward for eccentricity ratio 0.4, decreases steadily from 20% textured portion onward for eccentricity ratio 0.6 and decreases sharply from 20% to 60% textured portion for eccentricity ratio 0.8.

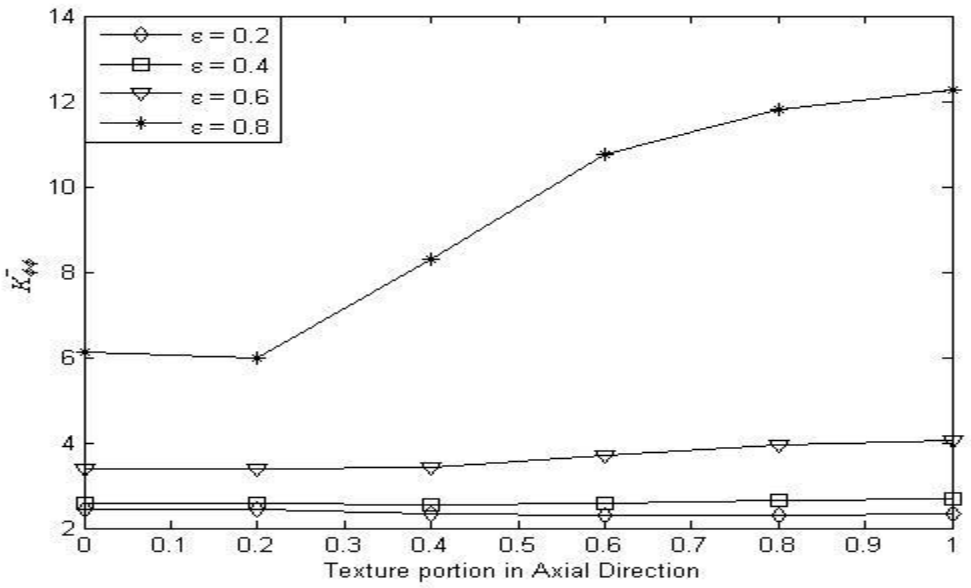

Figure 5.31: Effect of textured portion in axial direction on direct stiffness coefficient, $\overline{K}_{\phi\phi}$, of cylindrical textured journal bearing ($L/D = 1$, $S_p = 0.6$, $\Delta\bar{h} = 0.1$, $\alpha = 1$)

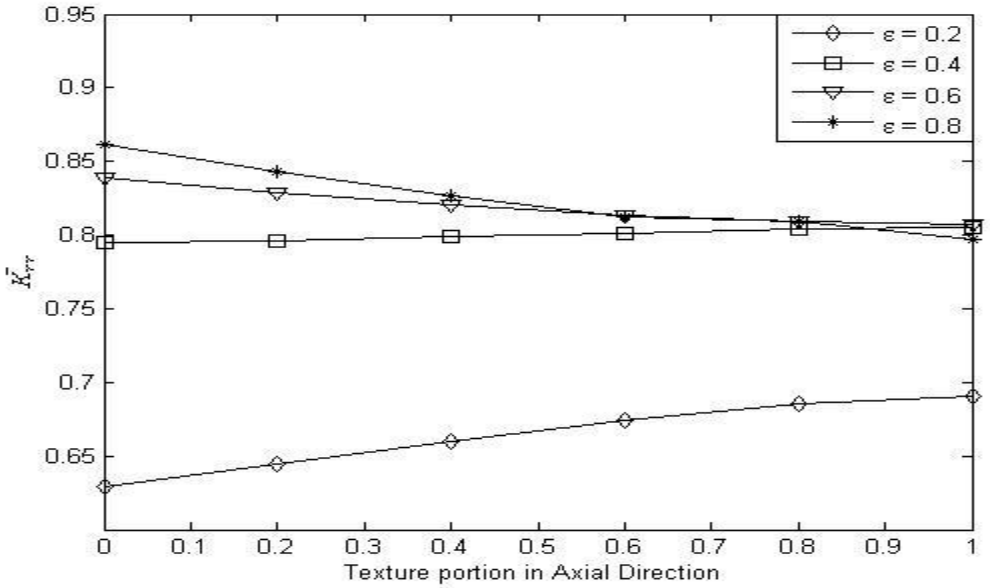

Figure 5.32: Effect of textured portion in axial direction on direct stiffness coefficient, $\overline{K}_{rr}$, of cylindrical textured journal bearing ($L/D = 1,\ S_p = 0.6,\ \Delta\bar{h} = 0.1,\ \alpha = 1$)

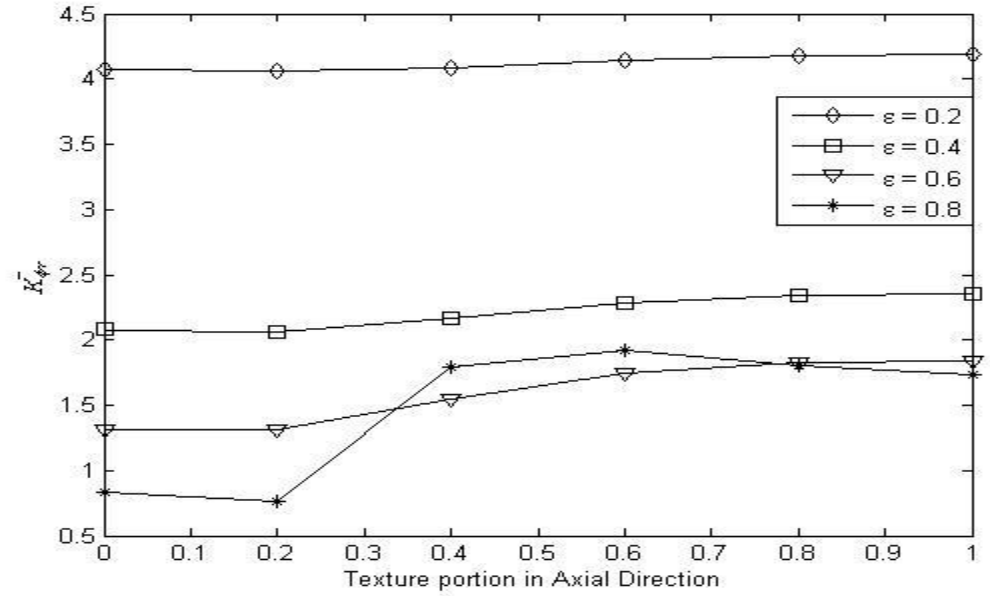

Figure 5.33: Effect of textured portion in axial direction on cross-coupled stiffness coefficient, $\overline{K}_{\phi r}$, of cylindrical textured journal bearing ($L/D = 1,\ S_p = 0.6,\ \Delta\bar{h} = 0.1,\ \alpha = 1$)

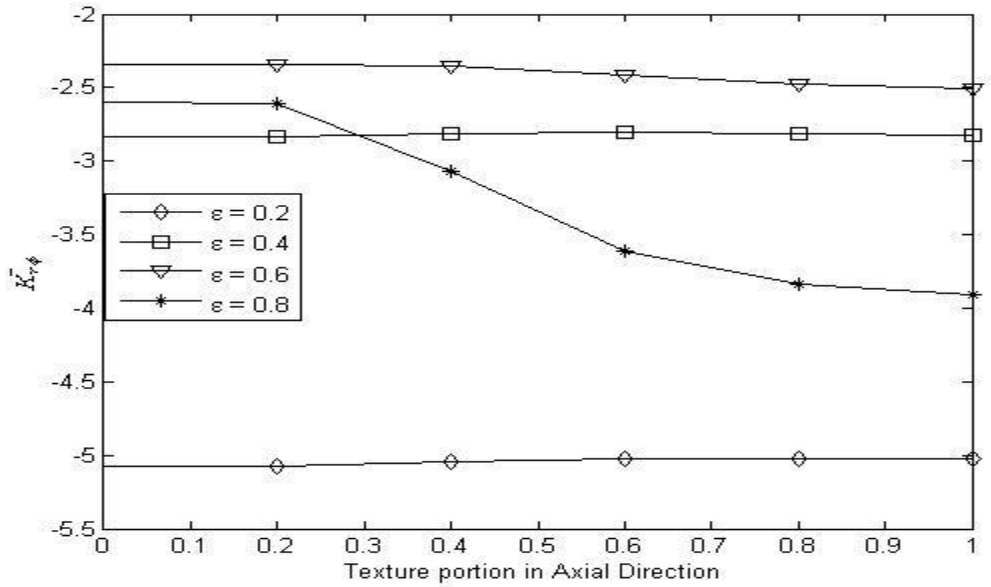

Figure 5.34: Effect of textured portion in axial direction on cross-coupled stiffness coefficient, $\overline{K}_{r\phi}$, of cylindrical textured journal bearing ($L/D = 1,\ S_p = 0.6,\ \Delta\bar{h} = 0.1,\ \alpha = 1$)

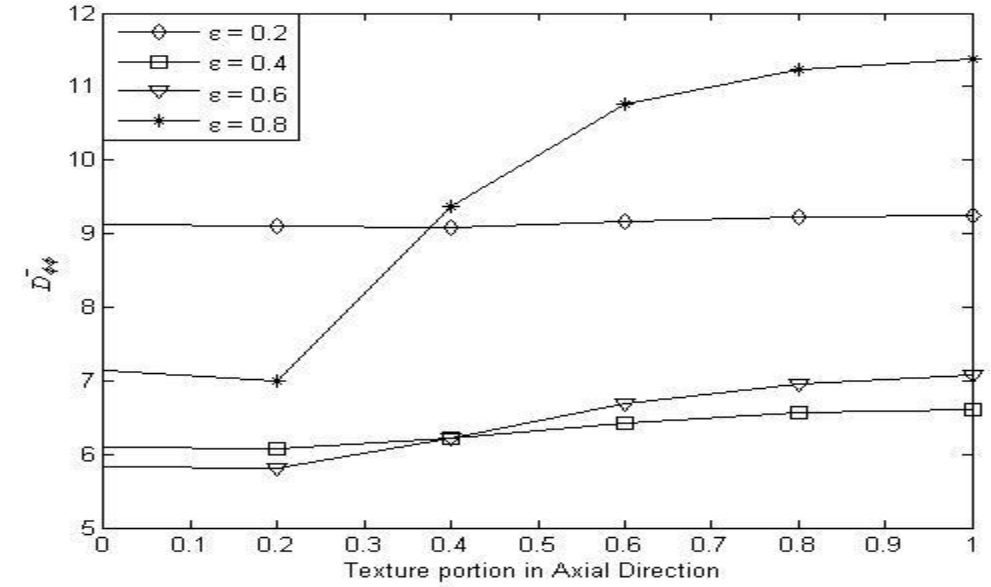

Figure 5.35: Effect of textured portion in axial direction on direct damping coefficient, $\overline{D}_{\phi\phi}$, of cylindrical textured journal bearing ($L/D = 1,\ S_p = 0.6,\ \Delta\bar{h} = 0.1,\ \alpha = 1$)

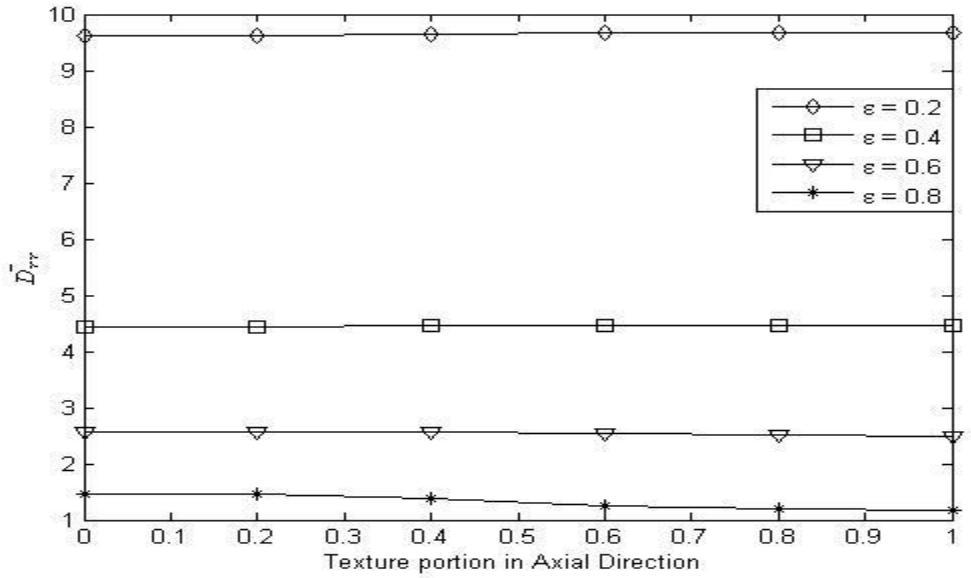

Figure 5.36: Effect of textured portion in axial direction on direct damping coefficient, $\overline{D}_{rr}$, of cylindrical textured journal bearing ($L/D = 1,\ S_p = 0.6,\ \Delta\bar{h} = 0.1,\ \alpha = 1$)

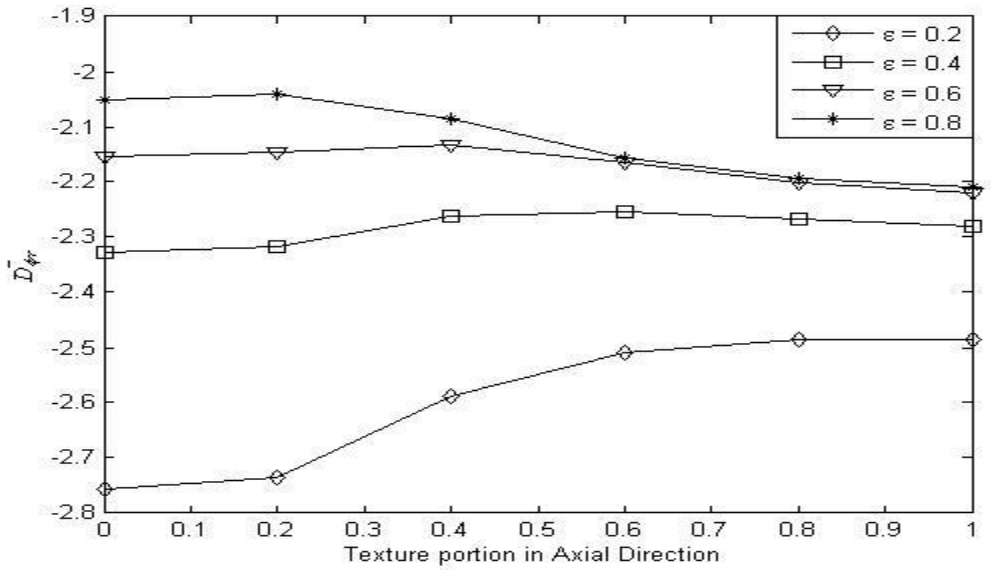

Figure 5.37: Effect of textured portion in axial direction on cross-coupled damping coefficient, $\overline{D}_{\phi r}$, of cylindrical textured journal bearing ($L/D = 1,\ S_p = 0.6,\ \Delta\bar{h} = 0.1,\ \alpha = 1$)

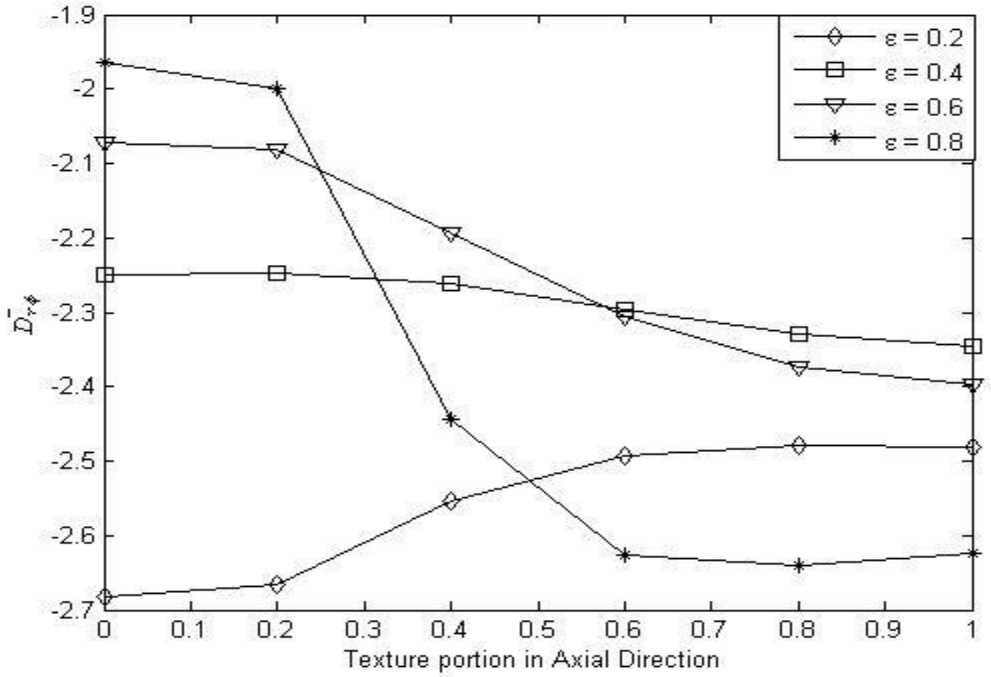

Figure 5.38: Effect of textured portion in axial direction on cross-coupled damping coefficient, $\overline{D}_{r\phi}$, of cylindrical textured journal bearing ($L/D = 1,\ S_p = 0.6,\ \Delta\overline{h} = 0.1,\ \alpha = 1$)

5.1.8 Effect of textured portion in axial direction on mass parameter and whirl ratio:

It has been observed from Fig 5.39 that the critical mass parameter decreases from 20% to 40% textured condition and then increases up to fully textured condition in axial direction for eccentricity ratio 0.6. However, in the case of eccentricity ratios 0.2 and 0.4, the critical mass parameter increases steadily from 20% textured condition to fully textured condition in axial direction. Corresponding whirl ratios are found to be below 0.5 as seen in Fig 5.40, affirming half-frequency whirling.

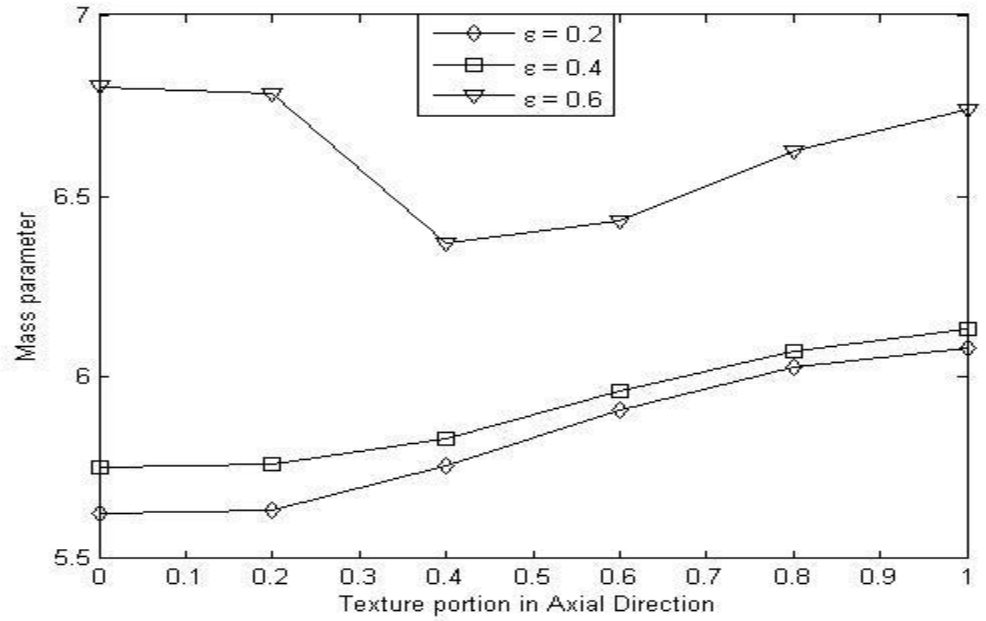

Figure 5.39: Effect of textured portion in axial direction on mass parameter of cylindrical textured journal bearing ($L/D = 1,\ S_p = 0.6,\ \Delta\bar{h} = 0.1,\ \alpha = 1$)

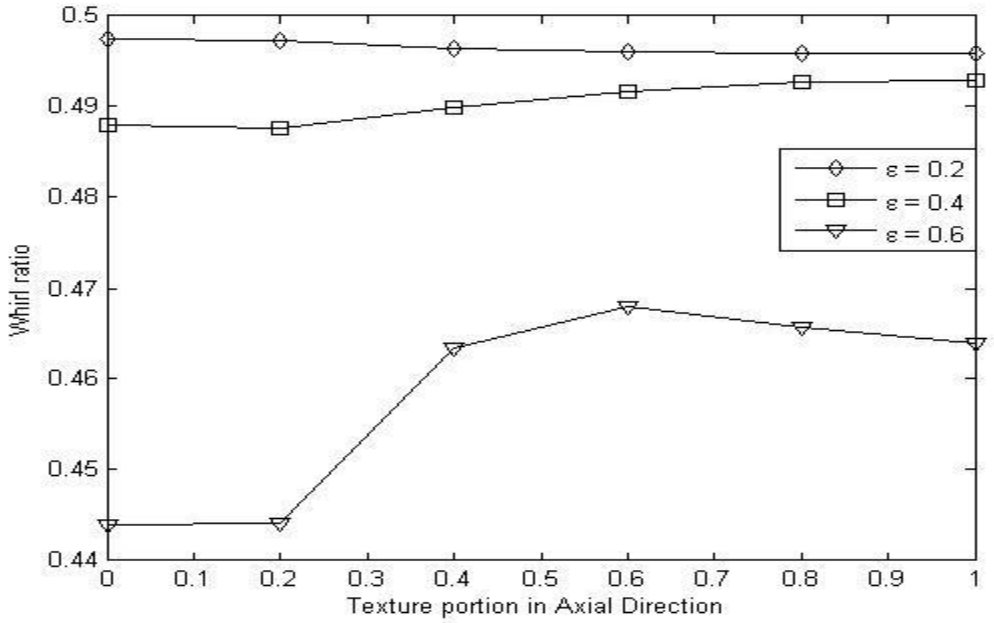

Figure 5.40: Effect of textured portion in axial direction on whirl ratio of cylindrical textured journal bearing ($L/D = 1,\ S_p = 0.6,\ \Delta\bar{h} = 0.1,\ \alpha = 1$)

5.2 Summary:

In this chapter, the dynamic and stability characteristics like stiffness, damping coefficients, mass parameter and whirl ratio are presented for cylindrical textured journal bearing. Effects of textured area density, textured depth, eccentricity ratio, textured portion in circumferential as well as axial direction on these parameters have been discussed. Some interesting and important observations have been made. It has been found that partial texturing in circumferential direction beyond 60% has no effect on these parameters. Similarly, partial texturing below 20% in axial direction also does not have any influence on these parameters.

CHAPTER 6

DYNAMIC CHARACTERISTICS AND STABILTY OF POSITIVE ELLIPTICAL TEXTURED JOURNAL BEARING

6.0 Introduction:

Steady state characterization of both positive and negative elliptical textured bearing was carried out in Chapter 4. Since performance characteristics of negative elliptical textured bearing were not found suitable, a theoretical analysis has been carried out to study the dynamic characteristics and stability of positive elliptical textured journal bearing only. The dynamic characteristics i.e., stiffness, damping coefficients and stability parameters, i.e., mass parameter and whirl ratio are presented in this chapter. Different plots are plotted by varying texture area density and texture portion etc.

6.1.1 Effect of eccentricity ratio and texture area density on stiffness and damping coefficients:

Variation of stiffness and damping coefficients with eccentricity ratio is presented here for $L/D = 1$, $\Delta\bar{h} = 0.1$, $\alpha = 1$, $\beta = 1$ and texture area density 0, 0.2, 0.4 and 0.6 in Figs. 6.1 through 6.8. Non-dimensional direct stiffness coefficient, $\overline{K}_{\phi\phi}$, increases with increase in eccentricity ratio for all texture area density considered as seen from Fig. 6.1. However, increase in the parameter is relatively more for texture area density 0.6. On the other hand non-dimensional direct stiffness coefficient, $\overline{K}_{rr}$, behavior is observed to be interesting for different texture area density as depicted in Fig. 6.2. The parameter increases from eccentricity ratio 0.2 to 0.4 for all texture area density and then the increase is slowed down for texture area densities 0 and 0.2 up to eccentricity ratio 0.8. In case of texture area density 0.4, increase in the parameter is slowed down up to eccentricity ratio 0.6 and then remains the same up to eccentricity ratio 0.8. The most interesting result is observed in case of texture area density 0.6 as the parameter starts decreasing little bit from eccentricity ratio 0.4 to 0.8. Besides the value of the stiffness coefficient at eccentricity ratio 0.2 is more than the values for texture area density 0 and 0.2, when it is less than the value corresponding to texture area density 0.4. Moreover, the value of the coefficient for texture area density 0.6 is the lowest at eccentricity ratio 0.8 compared to other

texture area densities. It implies that effect of texture area density on $\overline{K}_{rr}$ is not uniform and higher texture area density results in decrease in the parameter. It has been observed from Fig. 6.3 that the non-dimensional cross-coupled stiffness coefficient, $\overline{K}_{\phi r}$, decreases with increase in eccentricity ratio for all texture area densities considered and higher the texture area density the coefficient is also marginally higher particularly at higher eccentricity ratios. The non-dimensional cross-coupled stiffness, $\overline{K}_{r\phi}$, increases sharply from eccentricity ratio 0.2 to 0.4 and then increment slows down up to eccentricity ratio 0.6 and finally it dips a little up to eccentricity ratio 0.8 for all texture area density considered as evident from Fig. 6.4. The parameter is marginally more for texture area density 0.2 for the entire range of eccentricity ratio. The coefficient drops relatively sharply from eccentricity ratio 0.6 to 0.8 for texture area density 0.6. It has been observed from Fig. 6.5 that the non-dimensional direct damping coefficient, $\overline{D}_{\phi\phi}$, initially get decreased from eccentricity ratio 0.2 to 0.4 and then rate of decrease slows down up to eccentricity ratio 0.6 and finally it increases from eccentricity ratio 0.6 to 0.8 for all texture area density considered. On the other hand, the non-dimensional direct damping coefficient, $\overline{D}_{rr}$, decreases with increase in eccentricity ratio for all texture area densities considered. The coefficient is marginally less for texture area density 0.2, when other texture area densities have no effect on the parameter over the entire range of eccentricity ratio as observed from Fig. 6.6. The non-dimensional cross-coupled damping coefficients, $\overline{D}_{\phi r}$ and $\overline{D}_{r\phi}$ increase with increase in eccentricity ratio as seen from Figs 5.17 and 5.18. However, the effect of texture area density on the parameter is not uniform in all the cases. The sequence of largest to smallest $\overline{D}_{\phi r}$ are found to be for texture area density of 0.6 & 0.4, 0, 0.2 at eccentricity ratio 0.2, for texture area density of 0.4, 0 & 0.6, 0.2 at eccentricity ratio 0.4, for texture area density of 0.4, 0 & 0.6, 0.2 at eccentricity ratio 0.6, for texture area density of 0.4, 0 & 0.2, 0.6 at eccentricity ratio 0.8. Similarly The sequence of largest to smallest $\overline{D}_{r\phi}$ are found to be for texture area density 0.4, 0.6, 0, 0.2 at eccentricity ratio 0.2, for texture area density 0.4, 0 & 0.2, 0.6 at eccentricity ratio 0.4, for texture area density 0.4, 0.2, 0, 0.6 at eccentricity ratio 0.6 and for texture area density 0.2, 0.4, 0, 0.6 at eccentricity ratio 0.8.

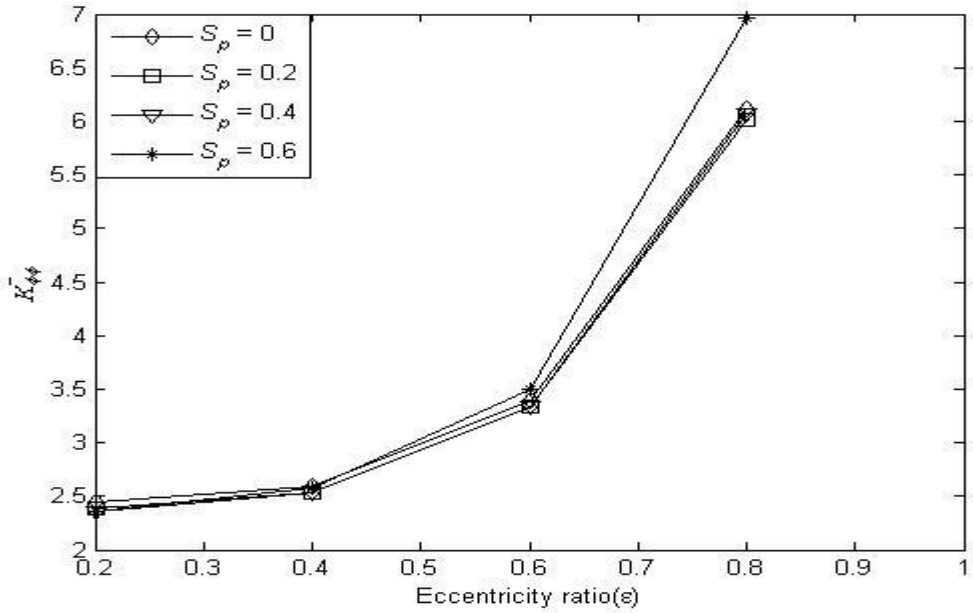

Figure 6.1: Variation of direct stiffness coefficient, $\overline{K}_{\phi\phi}$, with eccentricity ratio ($L/D = 1,\ \Delta\bar{h} = 0.03,\ \alpha = 1,\ \beta = 1$)

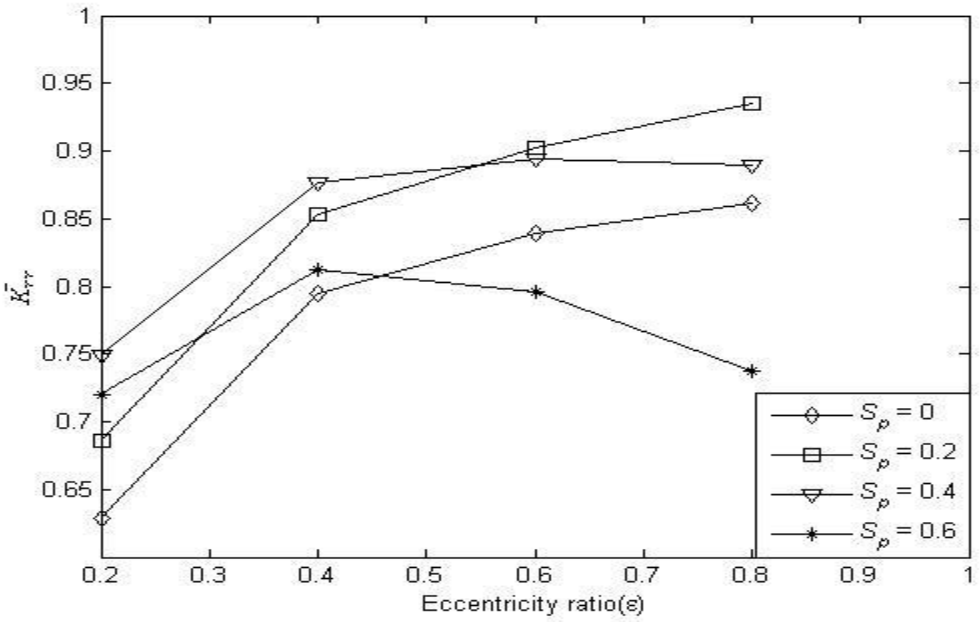

Figure 6.2: Variation of direct stiffness coefficient, $\overline{K}_{rr}$, with eccentricity ratio ($L/D = 1,\ \Delta\bar{h} = 0.03,\ \alpha = 1,\ \beta = 1$)

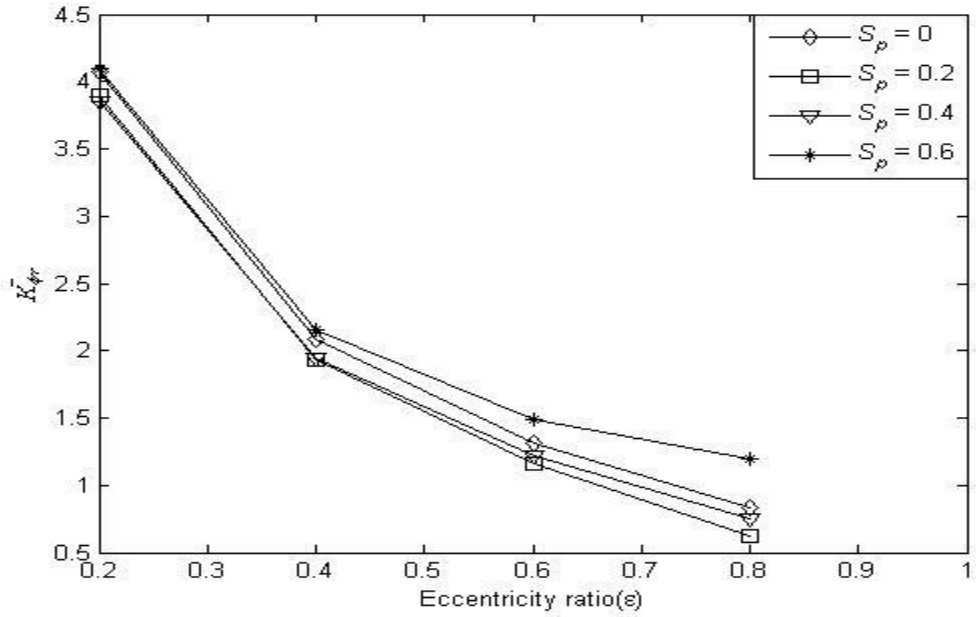

Figure 6.3: Variation of cross-coupled stiffness coefficient, $\overline{K}_{\phi r}$, with eccentricity ratio ($L/D =$ 1, $\Delta\bar{h} = 0.03$, $\alpha = 1$, $\beta = 1$)

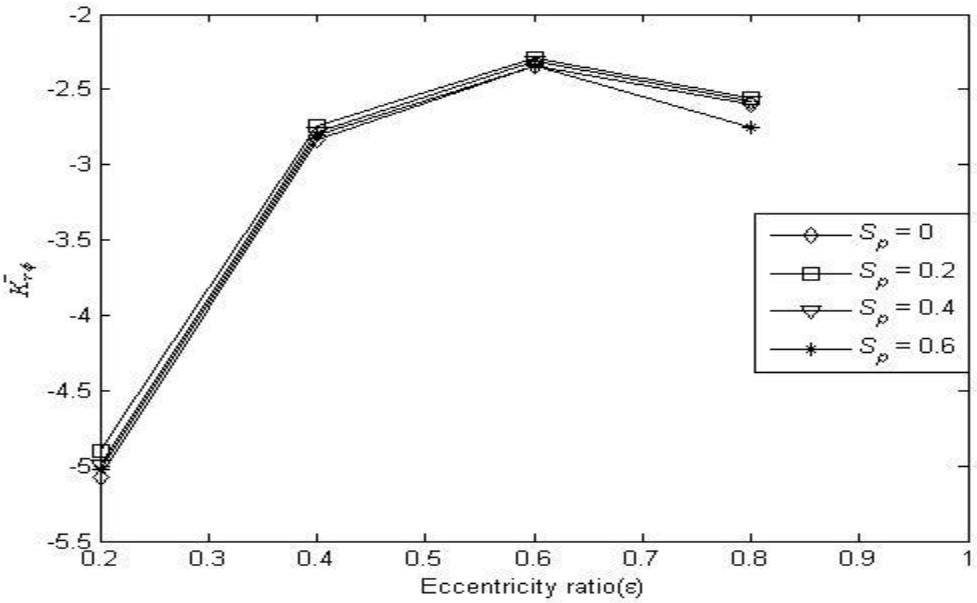

Figure 6.4: Variation of cross-coupled stiffness coefficient, $\overline{K}_{r\phi}$, with eccentricity ratio ($L/D =$ 1, $\Delta\bar{h} = 0.03$, $\alpha = 1$, $\beta = 1$)

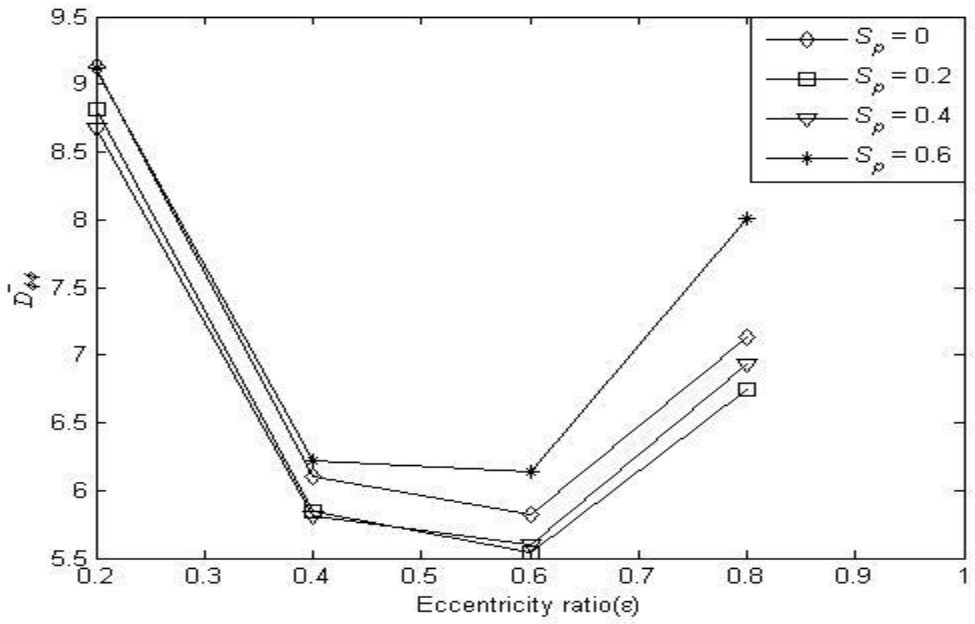

Figure 6.5: Variation of direct damping coefficient, $\bar{D}_{\phi\phi}$, with eccentricity ratio ($L/D = 1,\ \Delta\bar{h} = 0.03,\ \alpha = 1,\ \beta = 1$)

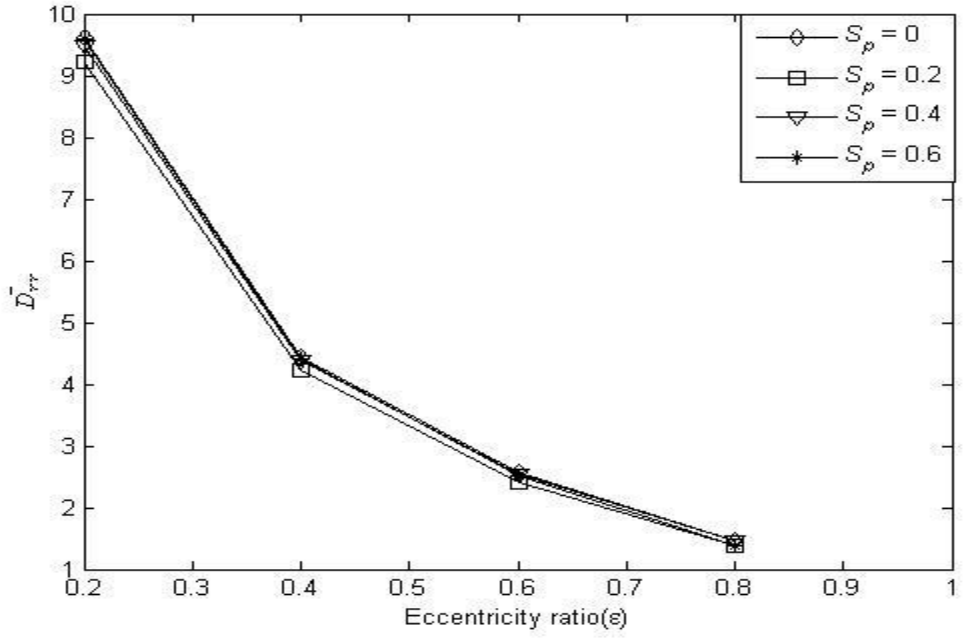

Figure 6.6: Variation of direct damping coefficient, $\bar{D}_{rr}$, with eccentricity ratio ($L/D = 1,\ \Delta\bar{h} = 0.03,\ \alpha = 1,\ \beta = 1$)

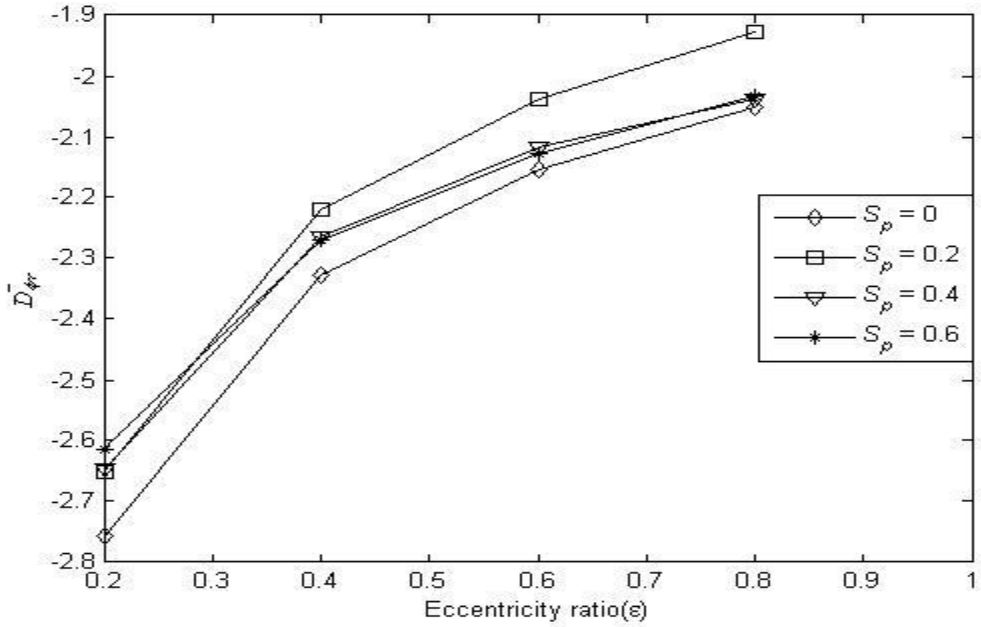

Figure 6.7: Variation of cross-coupled damping coefficient, $\bar{D}_{\phi r}$, with eccentricity ratio ($L/D = 1,\ \Delta\bar{h} = 0.03,\ \alpha = 1,\ \beta = 1$)

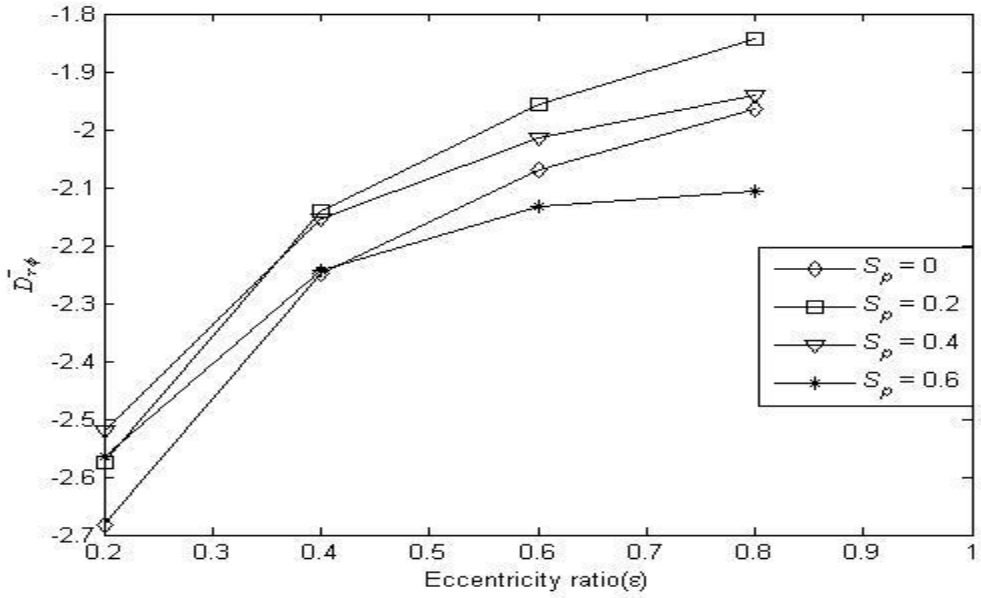

Figure 6.8: Variation of cross-coupled damping coefficient, $\bar{D}_{r\phi}$, with eccentricity ratio ($L/D = 1,\ \Delta\bar{h} = 0.03,\ \alpha = 1,\ \beta = 1$)

6.1.2 Effect of eccentricity ratio on mass parameter and whirl ratio:

As mentioned in Chapter 5, critical mass parameter and corresponding whirl ratio are estimated for eccentricity ratios, 0.2, 0.3, 0.4, 0.5 and 0.6. Since the critical mass parameter shoots up at higher eccentricity ratios, therefore, it has not been presented in the plots. The dynamic coefficients estimated for different eccentricity ratios and texture area densities are utilized to estimate critical mass parameter and whirl ratio and presented in Figs 6.9 and 6.10 for $L/D = 1$, $\Delta\bar{h} = 0.03$, $\alpha = 1$, $\beta = 1$. In general, critical mass parameter increases with increase in eccentricity ratio, however, it has been observed that when the journal is better stable at eccentricity ratios 0.2 and 0.3 for texture area density 0.6 compared to other texture area density considered, the same is not the case at other eccentricity ratios. Maximum stability is achieved for texture area density 0.4 at eccentricity ratios 0.4, 0.5 and 0.6. An interesting observation from the figure is that stability deteriorates for texture area density 0.6 from eccentricity ratio 0.4 onwards and it is even less than un-textured bearing (texture area density 0.0) at eccentricity ratio 0.6. As usual the whirl ratios are found to be below 0.5 as seen in Fig 6.10 affirming the critical mass parameters correspond to half-frequency whirling.

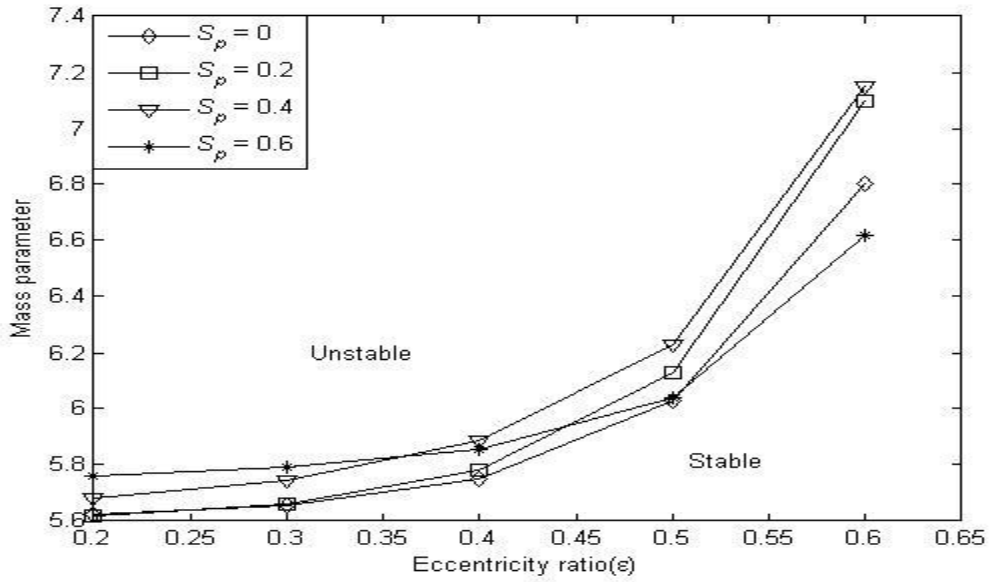

Figure 6.9: Variation of mass parameter with eccentricity ratio ($L/D = 1$, $\Delta\bar{h} = 0.03$, $\alpha = 1$, $\beta = 1$)

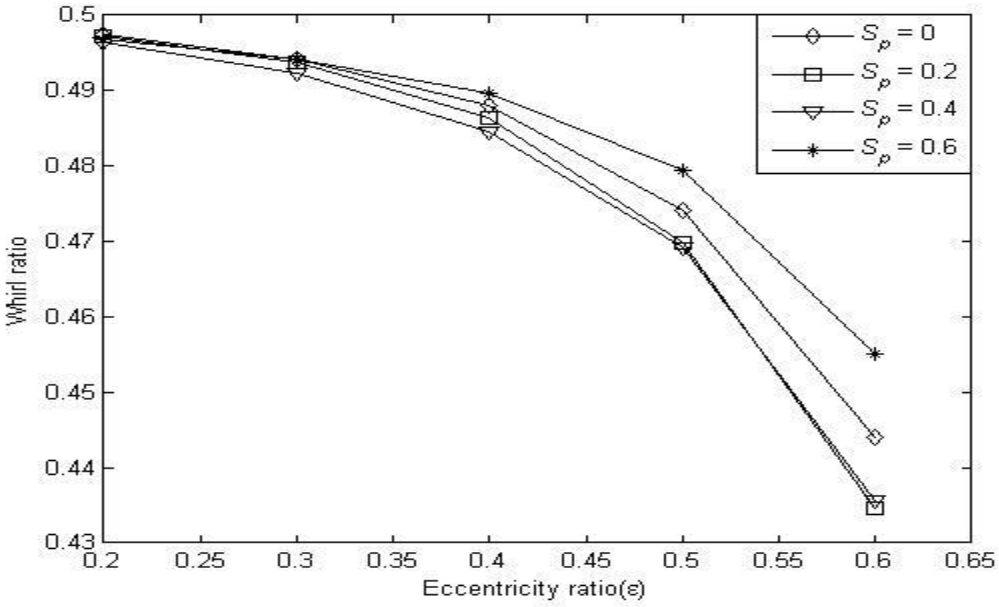

Figure 6.10: Variation of whirl ratio with eccentricity ratio ($L/D = 1,\ \Delta\bar{h} = 0.03,\ \alpha = 1,\ \beta = 1$)

6.1.3 Effect of textured portion in circumferential direction on stiffness and damping coefficients:

Textured portion in circumferential direction is varied keeping the axial direction fully textured for $L/D = 1,\ S_p = 0.6,\ \Delta\bar{h} = 0.1$ to study the effect of textured portion in the circumferential direction on dynamic characteristics. The results are presented in Figs. 6.11 through 6.18. It has been observed that the non-dimensional direct stiffness coefficient, $\overline{K}_{\phi\phi}$, increases from 40% textured portion to 60% textured portion for eccentricity ratio 0.8 and 0.6 as seen in Fig. 6.11. The increase is substantial for eccentricity ratio 0.8, when the increase is not much significant at eccentricity ratio 0.6. The higher $\overline{K}_{\phi\phi}$ for eccentricity ratio 0.8 may be attributed to the fact that stability of a bearing at higher eccentricity ratio is substantially high, in general, indicating higher stiffness. The parameter is not much affected due to variation of textured portion in all other cases considered. Further it has been observed from Fig. 6.12 that the non-dimensional direct stiffness coefficient, $\overline{K}_{rr}$, increases initially from un-textured condition to 40% textured portion, then it decreases up to 60% textured condition and finally it remains constant until fully textured condition is arrived at for all eccentricity ratios considered. The drop in the coefficient

from 40% to 60% textured portion is relatively sharper for eccentricity ratio 0.8 compared to other eccentricity ratios considered. It has been observed from Fig 6.13 that the non-dimensional cross-coupled stiffness coefficient $\overline{K}_{\phi r}$ decreases little with increase in texture portion from 20% to 40% textured portion, then it increases up to 60% textured portion and finally remains constant up to fully textured condition in axial direction for eccentricity ratio 0.2. There is a small increase in the coefficient from 40% to 60% textured portion for eccentricity ratios 0.2, 0.4 and 0.6, when there is a relatively sharp increase in the coefficient from 40% to 60% textured portion for eccentricity ratios 0.8. It has been noticed from Fig 6.14 that the cross-coupled stiffness coefficient, $\overline{K}_{r\phi}$ is not affected by variation of textured portion in axial direction for eccentricity ratios 0.2, 0.4 and 0.6. Interestingly the stiffness coefficient remains maximum for eccentricity ratio 0.6 from un-textured to fully textured condition and there is a sharp decrease in it for eccentricity ratio 0.8 from 40% to 60% textured portion. The non-dimensional direct damping coefficient, $\overline{D}_{\phi\phi}$, decreases from 20% to 40% textured condition and then increases from 40% to 60% textured condition and remains constant beyond 60% to fully textured condition in circumferential direction as seen from Fig 6.15. There is a sharp increase in the parameter from 40% to 60% textured condition for eccentricity ratio 0.8 compared to other eccentricity ratios considered. On the other hand the effect of texture portion in circumferential direction on the non-dimensional direct damping coefficient, $\overline{D}_{rr}$, is not significant for all the eccentricity ratios as seen in Fig.6.16. The non-dimensional cross-coupled damping coefficients are plotted in Figs. 6.17 and 6.18. $\overline{D}_{\phi r}$ increases from un-textured condition to 40% textured condition and finally remain constant up to fully textured condition eccentricity ratios 0.2 and 0.4 as seen in Fig. 6.17.The effect of textured portion on the coefficient for other eccentricity ratios considered is not significant. In the case of $\overline{D}_{r\phi}$, it increases initially from un-textured condition to 40% textured condition , then decreases up to 60% textured condition and finally remains constant up to fully textured condition for all eccentricity ratios considered though rate of increase and decrease are different for different eccentricity ratios as depicted in Fig. 6.18.

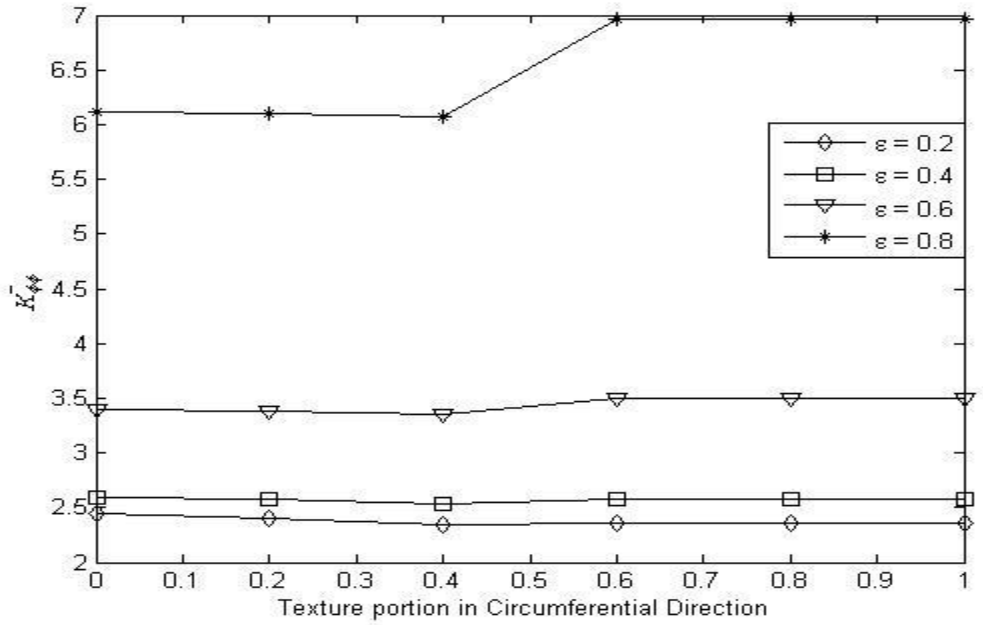

Figure 6.11: Effect of textured portion in circumferential direction on direct stiffness, $\overline{K}_{\phi\phi}$, coefficient of textured journal bearing ($L/D = 1,\ S_p = 0.6,\ \Delta\bar{h} = 0.03,\ \beta = 1$)

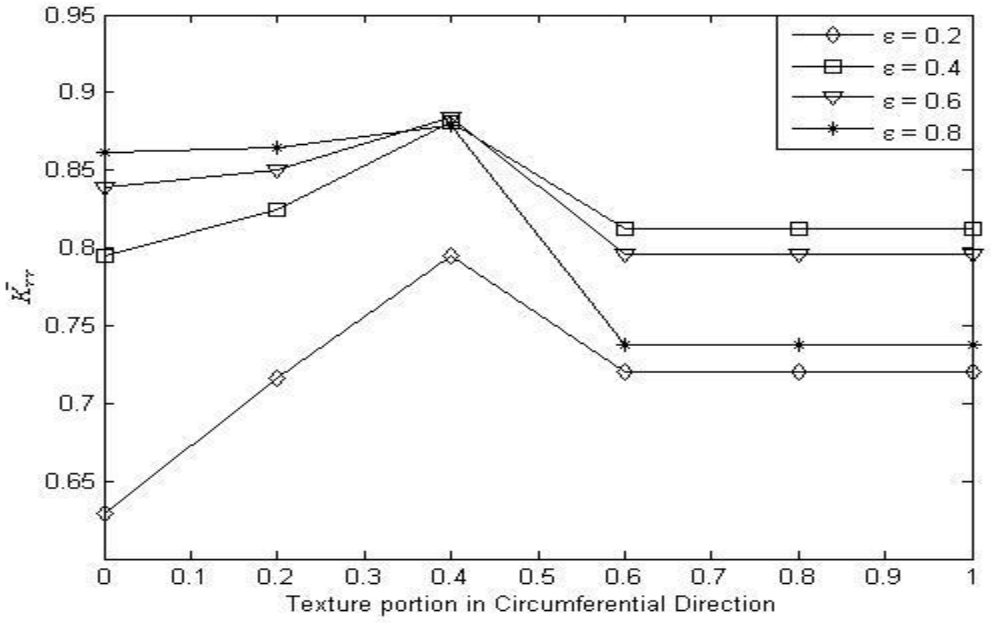

Figure 6.12: Effect of textured portion in circumferential direction on direct stiffness coefficient, $\overline{K}_{rr}$, of textured journal bearing ($L/D = 1,\ S_p = 0.6,\ \Delta\bar{h} = 0.03,\ \beta = 1$)

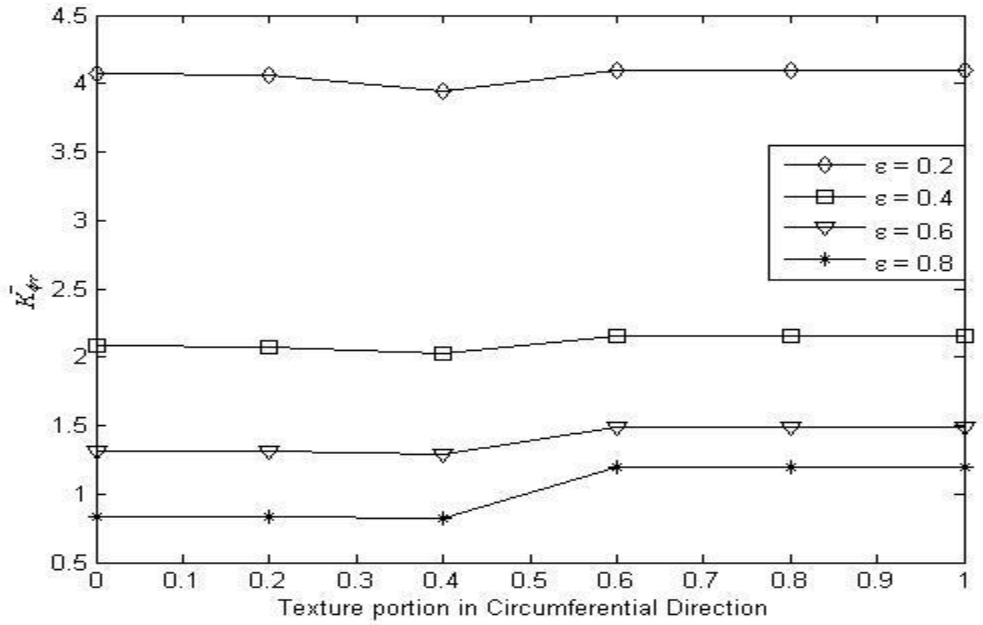

Figure 6.13: Effect of textured portion in circumferential direction on cross-coupled stiffness coefficient, $\overline{K}_{\phi r}$, of textured journal bearing ($L/D = 1,\ S_p = 0.6,\ \Delta\bar{h} = 0.03,\ \beta = 1$)

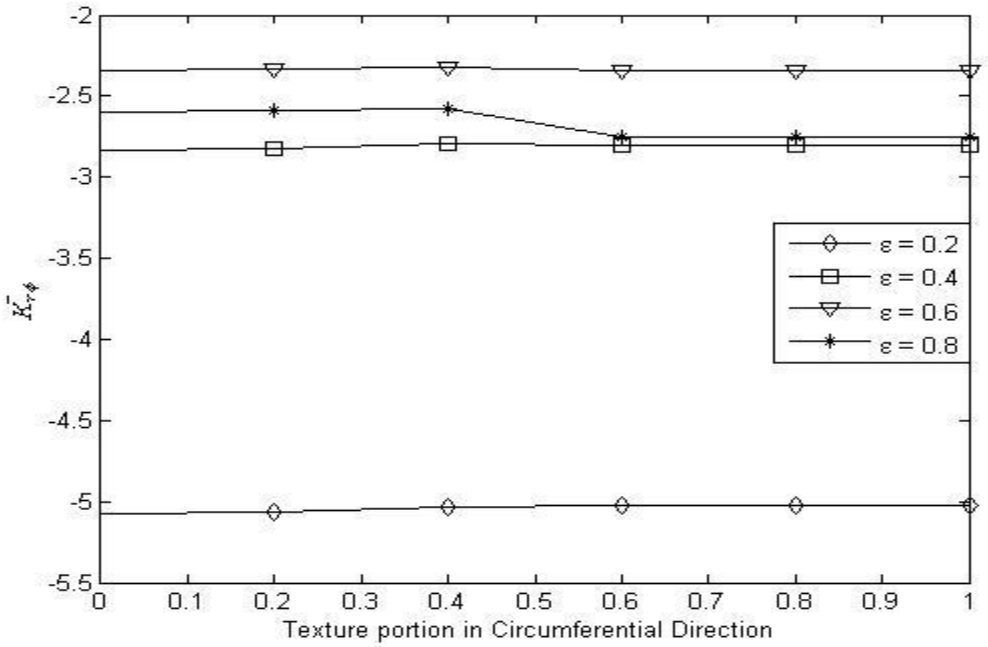

Figure 6.14: Effect of textured portion in circumferential direction on cross-coupled stiffness coefficient, $\overline{K}_{r\phi}$, of textured journal bearing ($L/D = 1,\ S_p = 0.6,\ \Delta\bar{h} = 0.03,\ \beta = 1$)

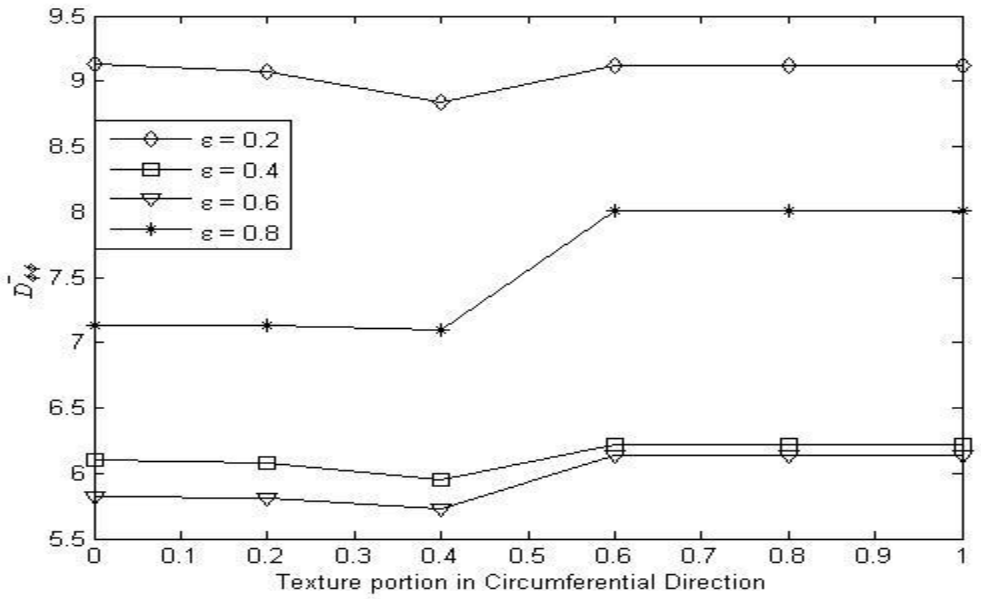

Figure 6.15: Effect of textured portion in circumferential direction on direct damping coefficient, $\bar{D}_{\phi\phi}$, of textured journal bearing ($L/D = 1,\ S_p = 0.6,\ \Delta\bar{h} = 0.03,\ \beta = 1$)

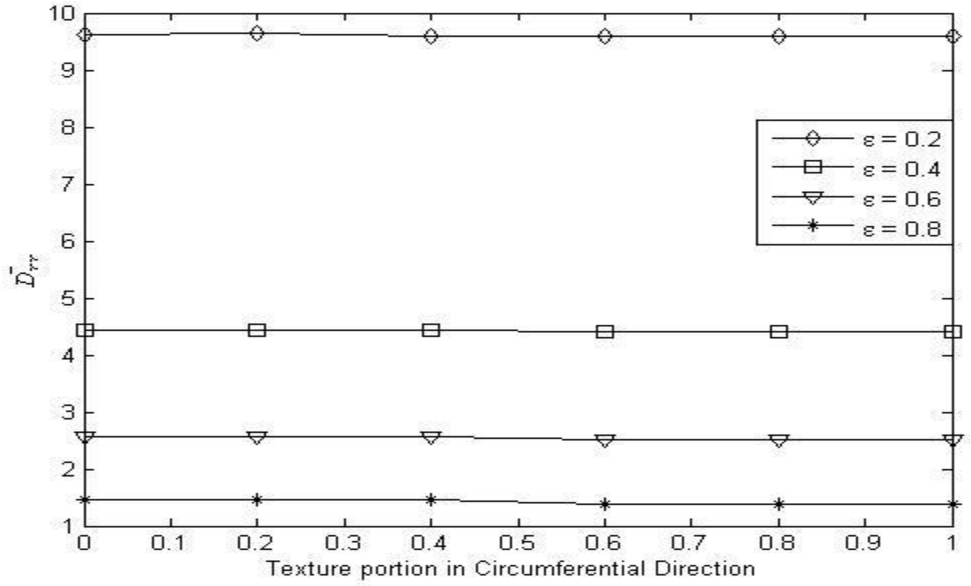

Figure 6.16: Effect of textured portion in circumferential direction on direct damping coefficient, $\bar{D}_{rr}$, of textured journal bearing ($L/D = 1,\ S_p = 0.6,\ \Delta\bar{h} = 0.03,\ \beta = 1$)

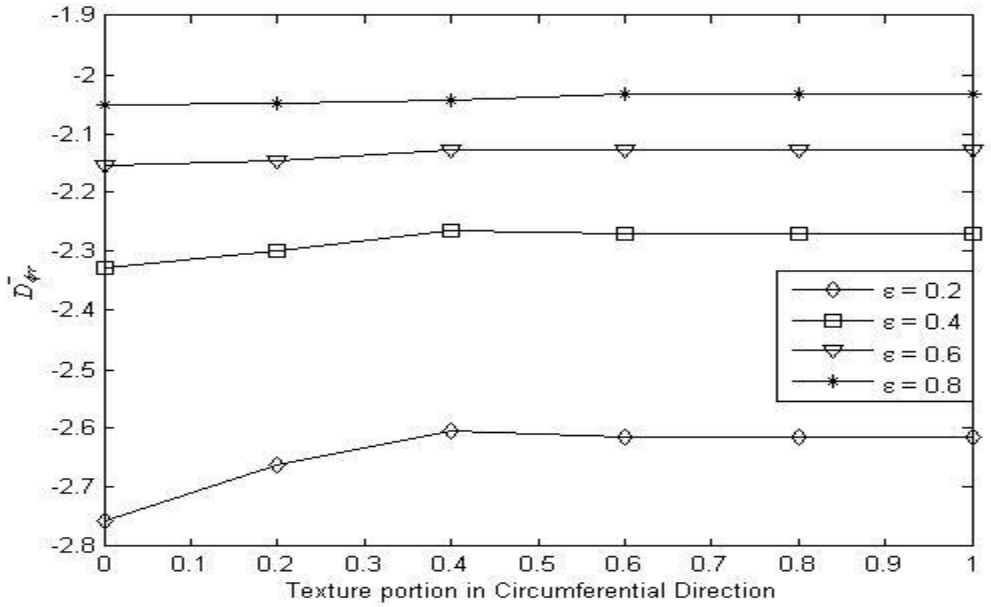

Figure 6.17: Effect of textured portion in circumferential direction on cross-coupled damping coefficient, $\overline{D}_{\phi r}$, of textured journal bearing ($L/D = 1,\ S_p = 0.6,\ \Delta\overline{h} = 0.03,\ \beta = 1$)

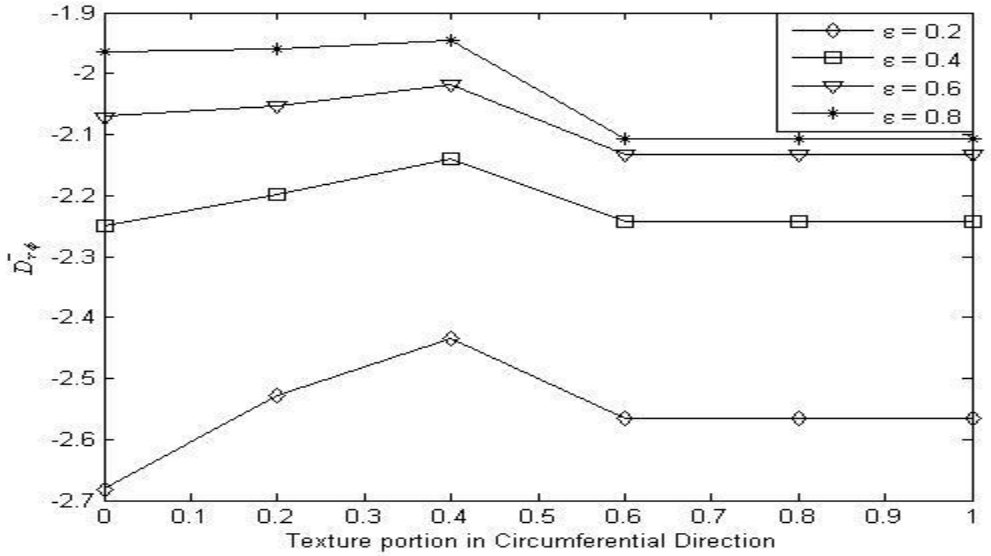

Figure 6.18: Effect of textured portion in circumferential direction on cross-coupled damping coefficient, $\overline{D}_{r\phi}$, of textured journal bearing ($L/D = 1,\ S_p = 0.6,\ \Delta\overline{h} = 0.03,\ \beta = 1$)

6.1.4 Effect of textured portion in circumferential direction on mass parameter and whirl ratio:

Critical mass parameter and corresponding whirl ratio are estimated for eccentricity ratios, 0.2, 0.4 and 0.6. Since the critical mass parameter shoots up at higher eccentricity ratios, therefore, it has not been presented in the plots as explained earlier. The dynamic coefficients estimated for different eccentricity ratios and texture portions in circumferential direction are utilized to estimate critical mass parameter and whirl ratio and presented in Figs 6.19 and 6.20. Critical mass parameter increases from un-textured condition to 40% textured portion and then decreases up to 60% textured portion and finally it remains constant up to fully textured condition in circumferential direction for eccentricity ratios 0.4 and 0.6. However the coefficient increases slightly from un-textured condition to 20% textured portion and then it remains more or less the same up to fully textured condition for eccentricity ratio 0.2. Maximum stability is achieved for 40% textured portion for all eccentricity ratios considered. As usual the whirl ratios are found to be below 0.5 as seen in Fig 6.20 affirming the critical mass parameters correspond to half-frequency whirling.

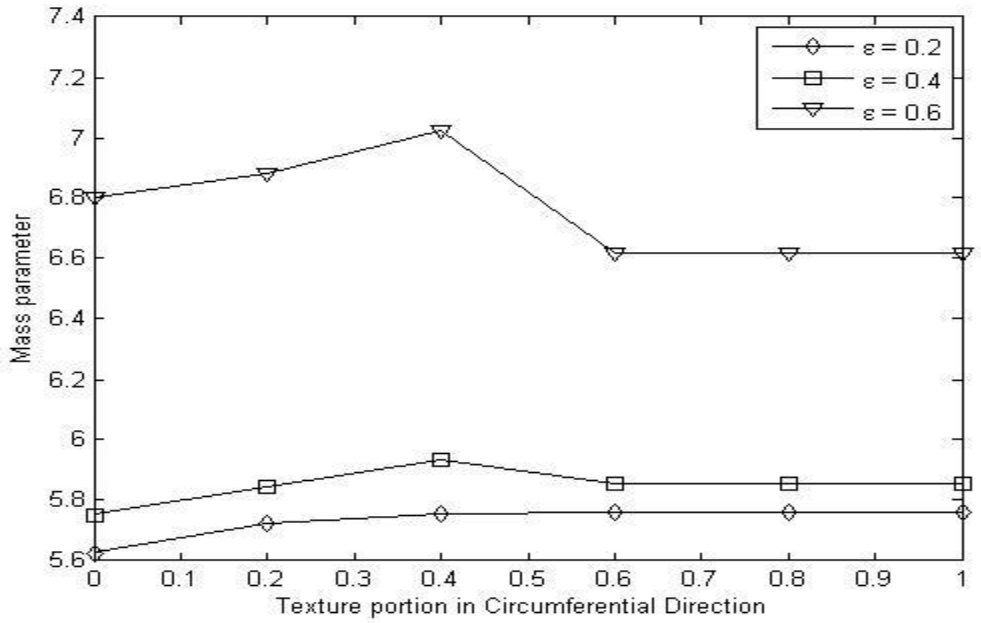

Figure 6.19: Effect of textured portion in circumferential direction on mass parameter of textured journal bearing ($L/D = 1$, $S_p = 0.6$, $\Delta\bar{h} = 0.03$, $\beta = 1$)

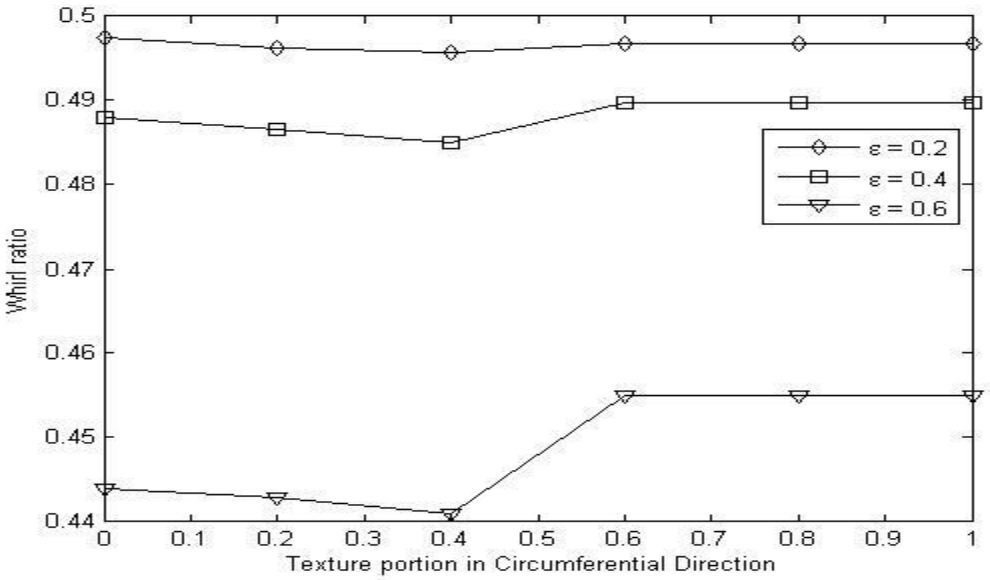

Figure 6.20: Effect of textured portion in circumferential direction on whirl ratio of textured journal bearing ($L/D = 1,\ S_p = 0.6,\ \Delta\bar{h} = 0.03,\ \beta = 1$)

6.1.5 Effect of textured portion in axial direction on stiffness and damping coefficients:

Four stiffness and four damping coefficients are estimated by varying textured portion in axial direction and keeping the circumferential direction fully textured for $L/D = 1,\ S_p = 0.6,$ $\Delta\bar{h} = 0.03$ and $\alpha = 1$. The results are presented in Figs. 6.21 through 6.28. The non-dimensional direct stiffness coefficients, $\overline{K}_{\phi\phi}$, increases from un-textured condition to fully textured condition in axial direction for eccentricity ratio 0.8 as seen in Fig. 6.21. However, the parameter is least affected by variation of textured portion in axial direction for other eccentricity ratios considered here. The other non-dimensional direct stiffness coefficient, $\overline{K}_{rr}$, increases significantly for eccentricity ratio 0.2, increases slightly for 0.4, decreases slightly for 0.6 and decreases significantly for 0.8 as depicted in Fig. 6.22. The non-dimensional cross-coupled stiffness coefficient, $\overline{K}_{\phi r}$, increases slightly for eccentricity ratios 0.6 and 0.8, when there is no significant changes noticed in the coefficient for eccentricity ratios 0.2 and 0.4 as seen in Fig. 6.23. On the other hand, it has been seen from Fig. 6.24 that the non-dimensional cross-coupled stiffness, $\overline{K}_{r\phi}$, decreases slightly for eccentricity ratio 0.8, when the coefficient is least affected by variation of textured portion in axial direction for all other eccentricity ratios considered here.

The non-dimensional direct damping coefficient, $\overline{D}_{\phi\phi}$, increases from 20% textured portion onward for eccentricity ratio 0.8, increases slightly for eccentricity ratios 0.4 and 0.6, and least affected for eccentricity ratio 0.2 as observed from Fig. 6.25. The other non-dimensional direct damping coefficient, $\overline{D}_{rr}$, has been found to be not affected by the variation of textured portion in axial direction as seen in Fig. 6.26. The non-dimensional cross-coupled damping coefficient, $\overline{D}_{\phi r}$, increases slightly for eccentricity ratios 0.2, when it increases marginally for eccentricity ratio 0.4 and o.6, from un-textured condition to 40% textured portion only. The coefficient increase from un-textured condition to 20% textured portion and then decreases marginally from 40% textured portion to fully textured condition for eccentricity ratio 0.8 as depicted in Fig. 6.27. The other non-dimensional cross-coupled damping coefficient, $\overline{D}_{r\phi}$, increases for eccentricity ratio 0.2, increases initially up to 20% textured portion and then remains more or less the same up to fully textured condition for eccentricity ratio 0.4, initially increases up to 40% textured condition and remains more or less the same up to fully textured condition for eccentricity ratio 0.6. However, the trend is somewhat different for eccentricity ratio 0.8. In this case the coefficient initially increases up to 20% textured portion and then decreases up to fully textured condition in axial direction as observed in Fig. 6.28.

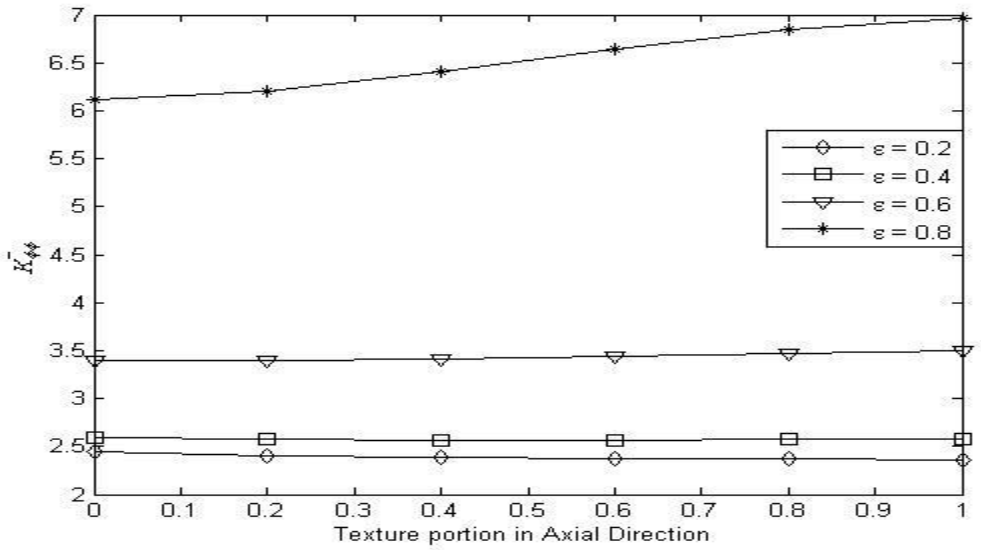

Figure 6.21: Effect of textured portion in axial direction on direct stiffness coefficient, $\overline{K}_{\phi\phi}$, of textured journal bearing ($L/D = 1$, $S_p = 0.6$, $\Delta\bar{h} = 0.03$, $\alpha = 1$)

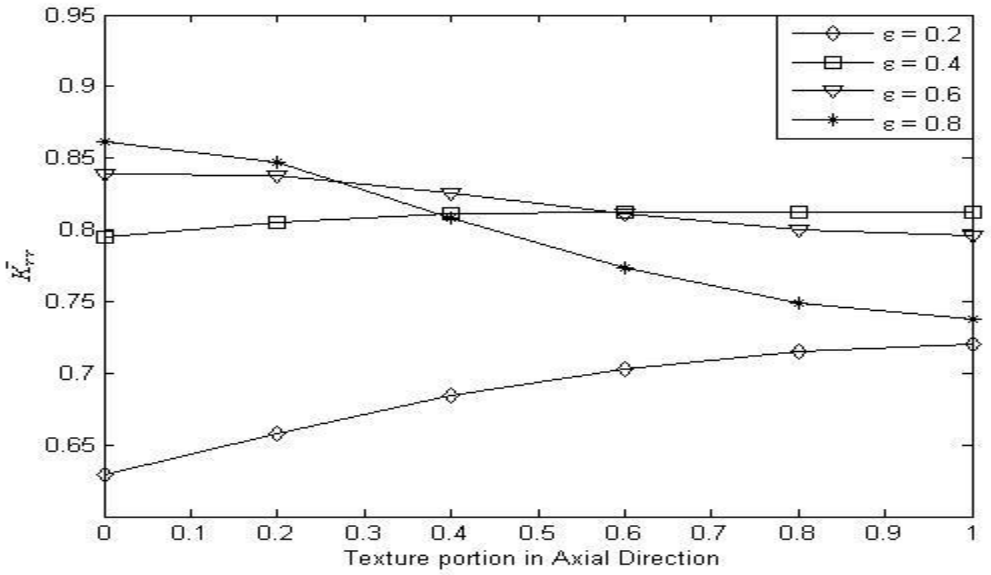

Figure 6.22: Effect of textured portion in axial direction on direct stiffness coefficient, $\overline{K}_{rr}$, of textured journal bearing ($L/D = 1,\ S_p = 0.6,\ \Delta\bar{h} = 0.03,\ \alpha = 1$)

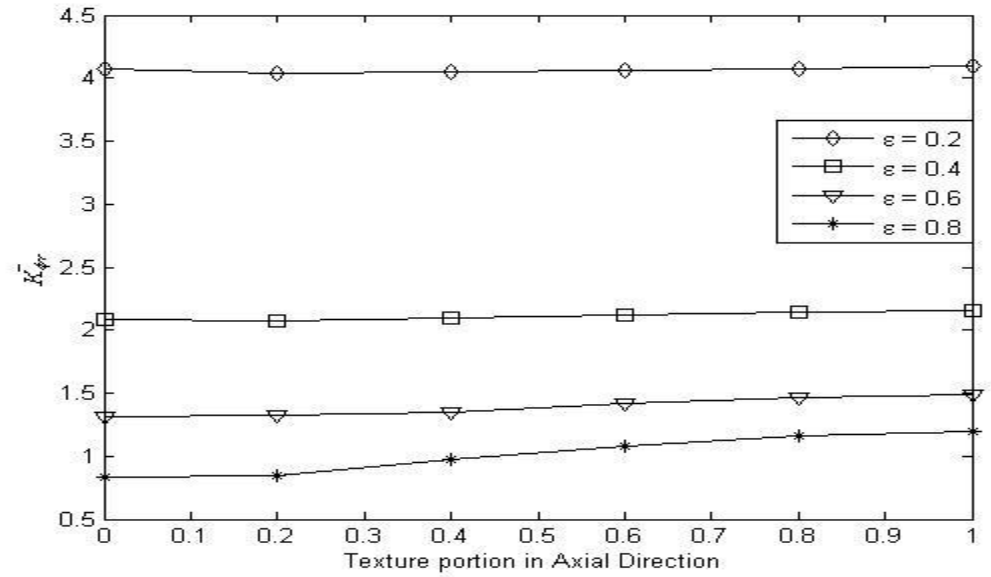

Figure 6.23: Effect of textured portion in axial direction on cross-coupled stiffness coefficient, $\overline{K}_{\phi r}$, of textured journal bearing ($L/D = 1,\ S_p = 0.6,\ \Delta\bar{h} = 0.03,\ \alpha = 1$)

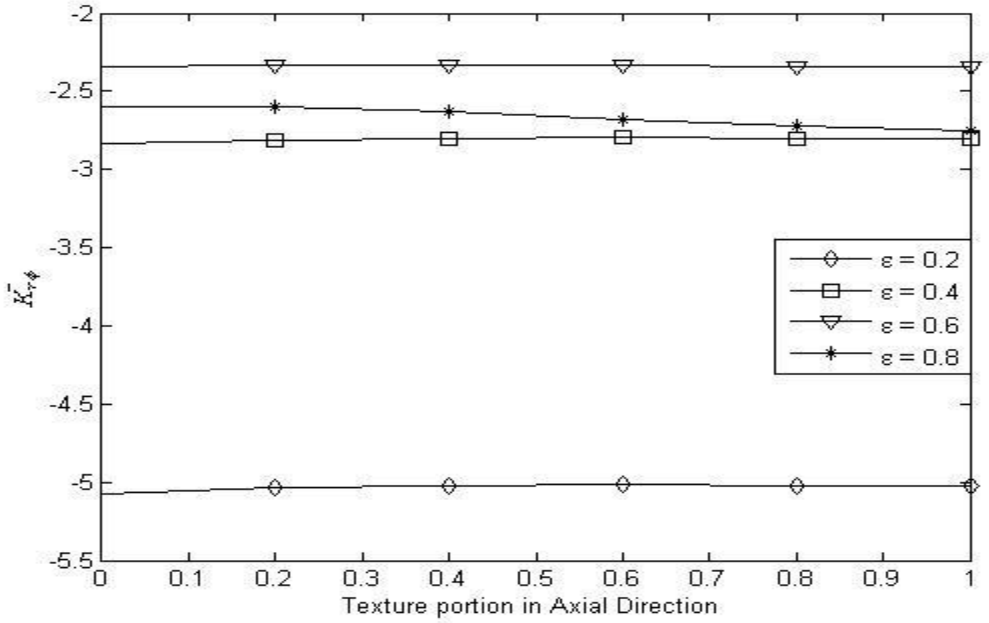

Figure 6.24: Effect of textured portion in axial direction on cross-coupled stiffness coefficient, $\overline{K}_{r\phi}$, of textured journal bearing ($L/D = 1,\ S_p = 0.6,\ \Delta\bar{h} = 0.03,\ \alpha = 1$)

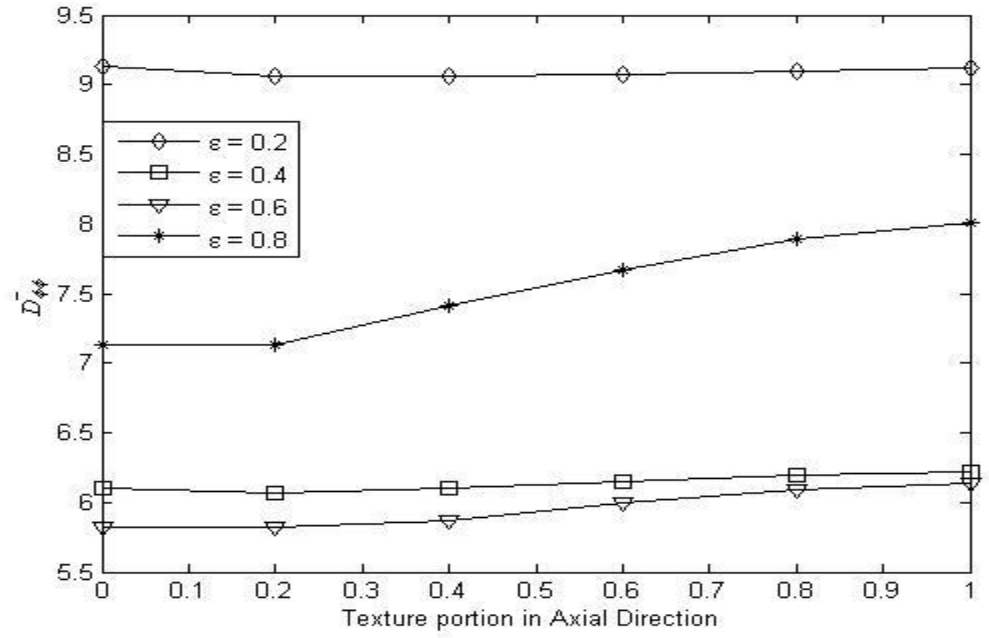

Figure 6.25: Effect of textured portion in axial direction on direct damping coefficient, $\overline{D}_{\phi\phi}$, of textured journal bearing ($L/D = 1,\ S_p = 0.6,\ \Delta\bar{h} = 0.03,\ \alpha = 1$)

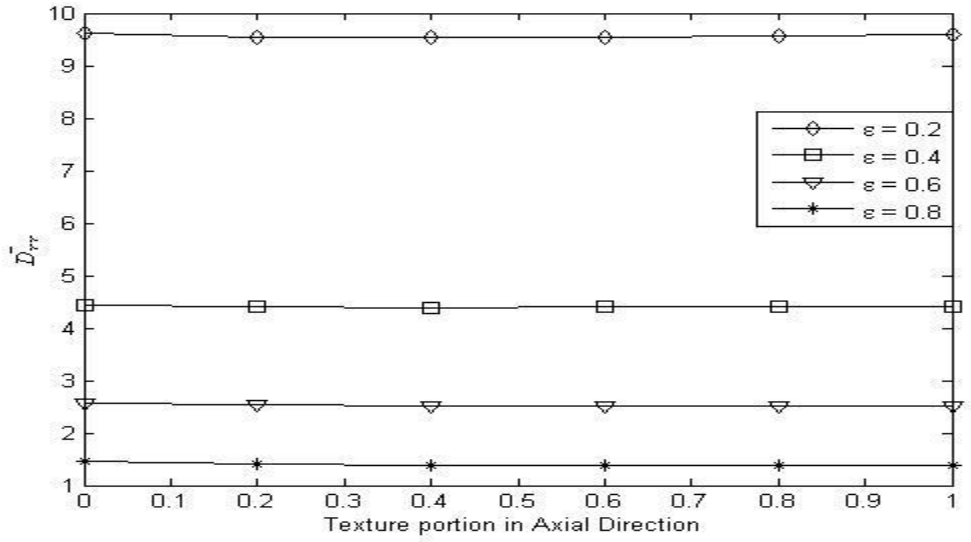

Figure 6.26: Effect of textured portion in axial direction on direct damping coefficient, $\overline{D}_{rr}$, of textured journal bearing ($L/D = 1,\ S_p = 0.6,\ \Delta\bar{h} = 0.03,\ \alpha = 1$)

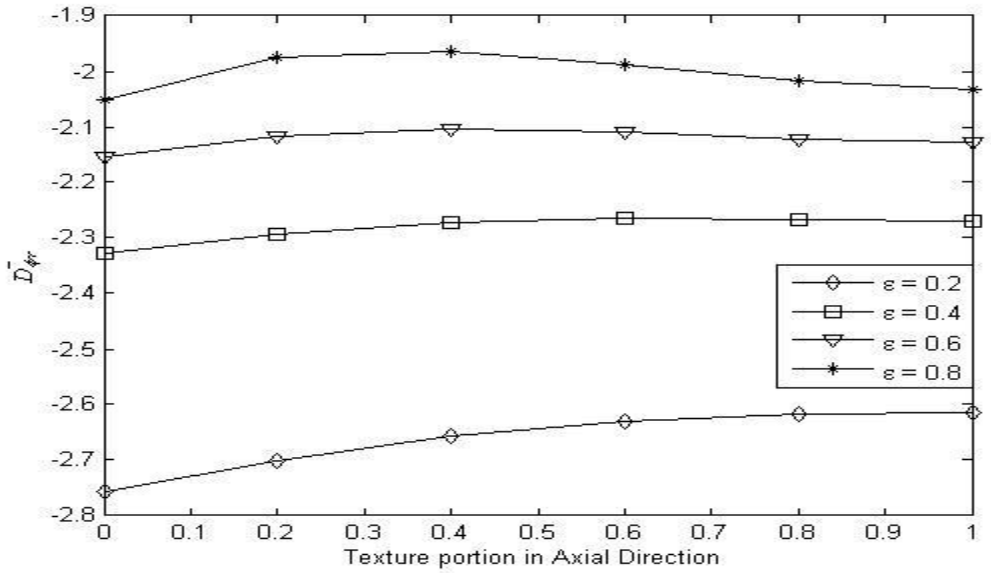

Figure 6.27: Effect of textured portion in axial direction on cross-coupled damping coefficient, $\overline{D}_{\phi r}$, of textured journal bearing ($L/D = 1,\ S_p = 0.6,\ \Delta\bar{h} = 0.03,\ \alpha = 1$)

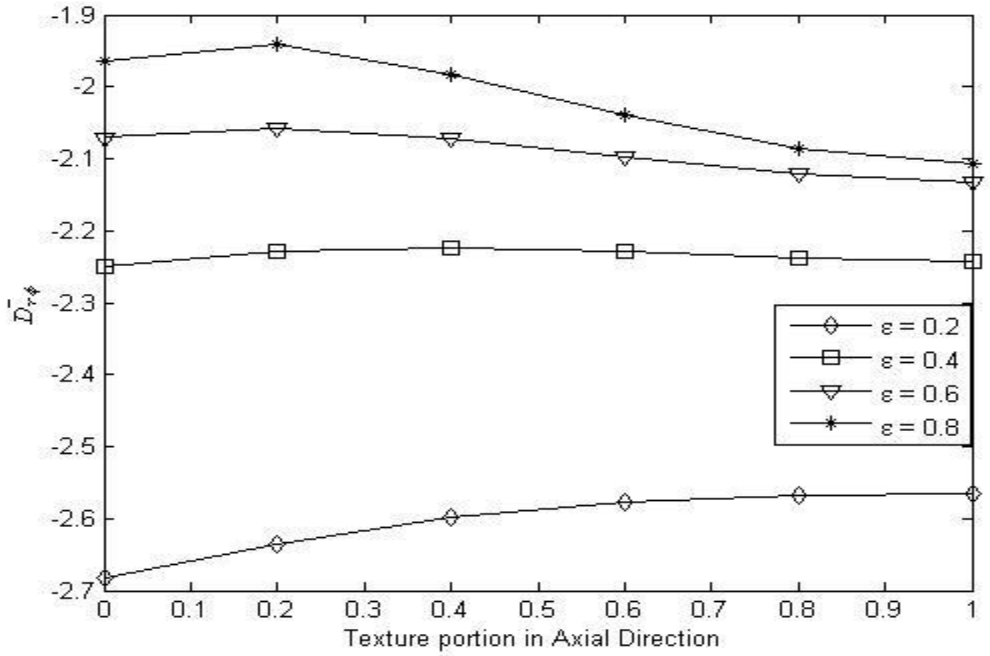

Figure 6.28: Effect of textured portion in axial direction on cross-coupled damping coefficient, $\overline{D}_{r\phi}$, of textured journal bearing ($L/D = 1,\ S_p = 0.6,\ \Delta\bar{h} = 0.03,\ \alpha = 1$)

6.1.6 Effect of textured portion in axial direction on mass parameter and whirl ratio:

As mentioned earlier, the critical mass parameter shoots up at higher eccentricity ratios; therefore, it has not been presented in the plots. Critical mass parameter and whirl ratio are estimated utilizing the dynamic coefficients estimated for different eccentricity ratios and texture portions in axial direction and presented in Figs 6.29 and 6.30. Critical mass parameter decreases from 40% textured portion onward for eccentricity ratio 0.6, when there is a slight improvement in stability with increase in textured portion in axial direction for eccentricity ratio 0.2 and 0.4. Maximum stability is achieved up to 40% textured portion for eccentricity ratio 0.6. As usual the corresponding whirl ratios are found to be below 0.5 as seen in Fig 6.30 affirming the critical mass parameters correspond to half-frequency whirling.

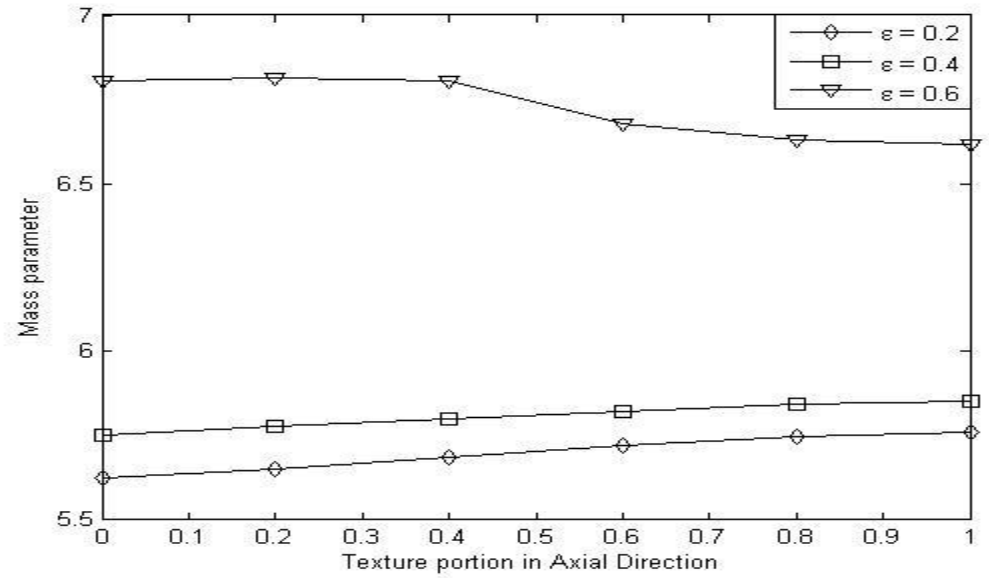

Figure 6.29: Effect of textured portion in axial direction on mass parameter of textured journal bearing ($L/D = 1,\ S_p = 0.6,\ \Delta\bar{h} = 0.03,\ \alpha = 1$)

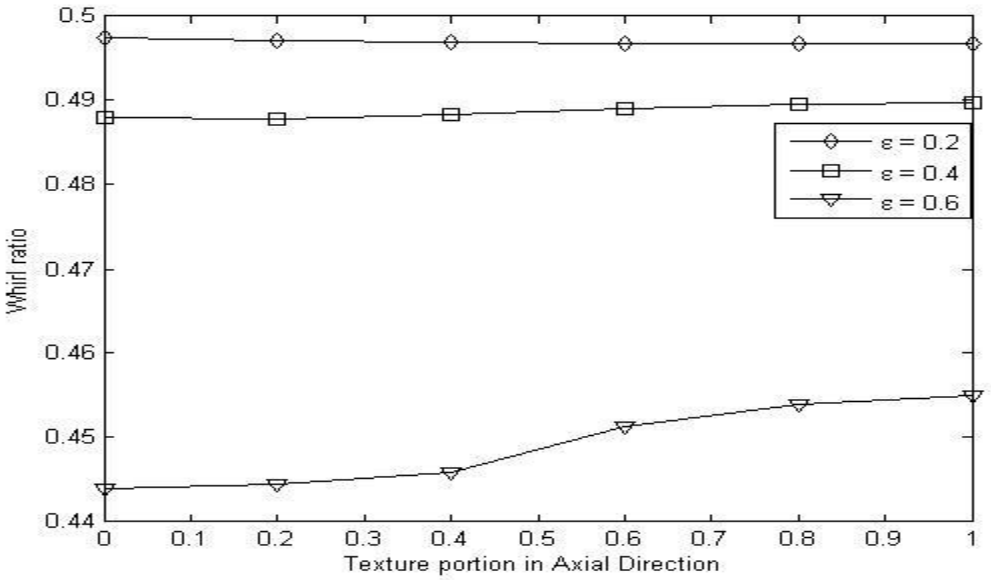

Figure 6.30: Effect of textured portion in axial direction on whirl ratio of textured journal bearing ($L/D = 1,\ S_p = 0.6,\ \Delta\bar{h} = 0.03,\ \alpha = 1$)

6.2 Summary:

Effects of textured area density, eccentricity ratio and textured portion in circumferential as well as axial direction on the dynamic and stability characteristics like stiffness and damping coefficients, mass parameter and whirl ratio are presented for elliptical textured journal bearing in this chapter. Some interesting and important observations have been made. It has been found that partial texturing in circumferential direction beyond 60% has no effect on these parameters. Similarly, partial texturing below 20% in axial direction also does not have any influence on these parameters.

CHAPTER 7

COMPARISON OF CYLINDRICAL AND ELLIPTICAL TEXTURED JOURNAL BEARINGS AND CONCLUSIONS

7.0 Introduction:

An attempt has been made in this present work to characterize cylindrical and elliptical textured journal bearings. In view of this both steady state and dynamic characteristics have been estimated and presented in chapters 3 through 6. Steady state characteristics include estimation of the performance parameters, viz., non-dimensional load carrying capacity, flow coefficient and friction variable with the variation of eccentricity ratio, textured density and textured portion in circumferential and axial directions of cylindrical and elliptical textured journal bearings. Steady state characteristics are presented in chapter 3 and chapter 4 for cylindrical textured and elliptical textured bearings respectively. Dynamic characteristics include two direct and two cross coupled stiffness coefficients and two direct and two cross coupled damping coefficients. Besides stability parameters are estimated for both cylindrical and elliptical textured bearings. Dynamic characteristics and stability analyses have been presented in chapter 5 and chapter 6 for cylindrical textured and elliptical textured bearings respectively.

To ascertain the better performing bearing between cylindrical and elliptical textured bearings, a comparison of the performance parameters have been presented in the following sections. Finally concluding remarks followed by future scopes for extending the present work have been presented in this chapter.

7.1 Comparison of cylindrical and elliptical textured journal bearings:

7.1.1 Effect of eccentricity ratio:

Figures 7.1 to 7.3 represent variation of load carrying capacity, flow coefficient and friction variable respectively of positive and negative cylindrical textured as well as elliptical textured bearing with eccentricity ratio for L/D=1, S_p = 0.6, $\Delta\bar{h}$ =0.03. Full texturing has been taken in circumferential as well as axial directions. Load carrying capacity increases with increase in eccentricity ratio all four types of bearings considered as observed from Fig. 7.1. Load carrying capacities of positive cylindrical and elliptical textured bearings are observed to be more than negative cylindrical and elliptical textured bearings. Film thickness in case of positive textured

bearing in the textured locations is thinner than negative textured bearing, which helps in developing more pressure resulting higher load carrying capacity particularly at higher eccentricity ratios. Another important observation from the presented result has been made that texturing whether it is cylindrical or elliptical does not have much influence on load carrying capacity. It may be attributed to the fact that the texture parameters like texture depth and texture area densities are the same for both cylindrical and elliptical textured bearings. Similar observations are made for flow coefficient for both elliptical and cylindrical textured bearings as seen in Fig. 7.2. However, the increase in flow coefficient is more or less linear with eccentricity ratio. On the other hand friction variable has been observed to be decreasing with increase in eccentricity ratio of all four types of journal bearing. Positive textured bearing has less friction variable while compared to negative textured bearing.

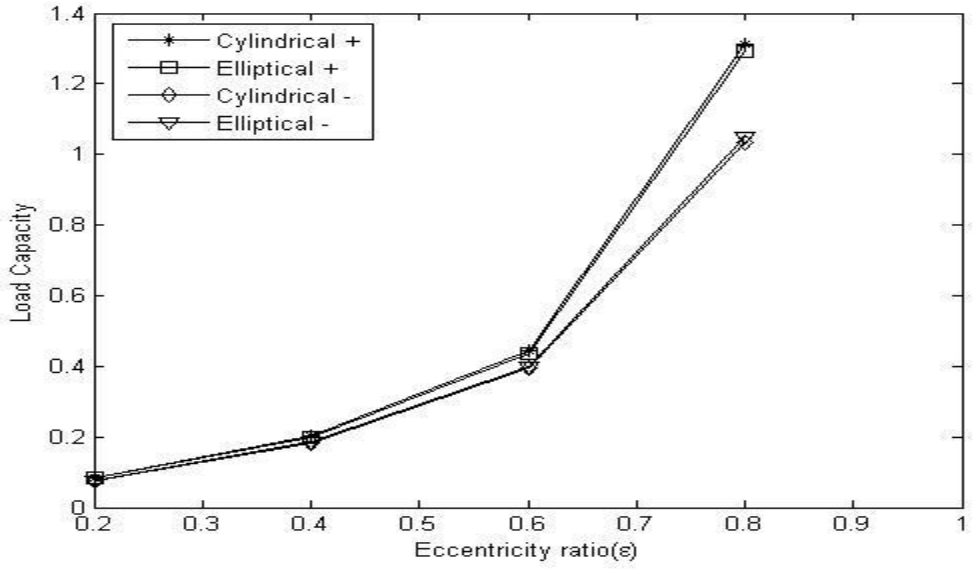

Figure 7.1: Variation of load carrying capacity with eccentricity ratio of textured journal bearing

(L/D=1, S_p = 0.6, $\Delta\bar{h}$ =0.03, α =1, β =1)

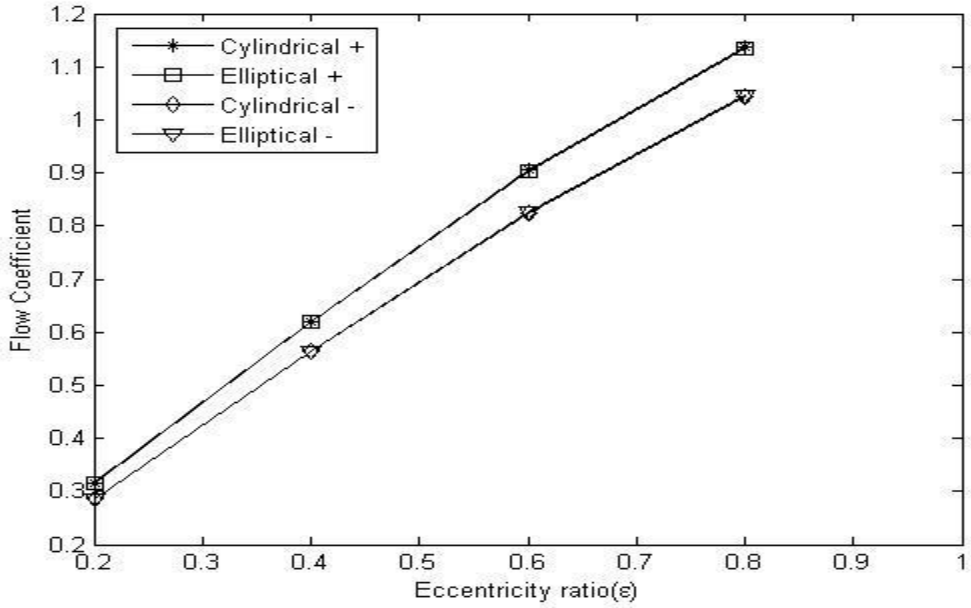

Figure 7.2: Variation of flow coefficient with eccentricity ratio of textured journal bearing

(L/D=1, S_p = 0.6, $\Delta\bar{h}$ =0.03, α =1, β =1)

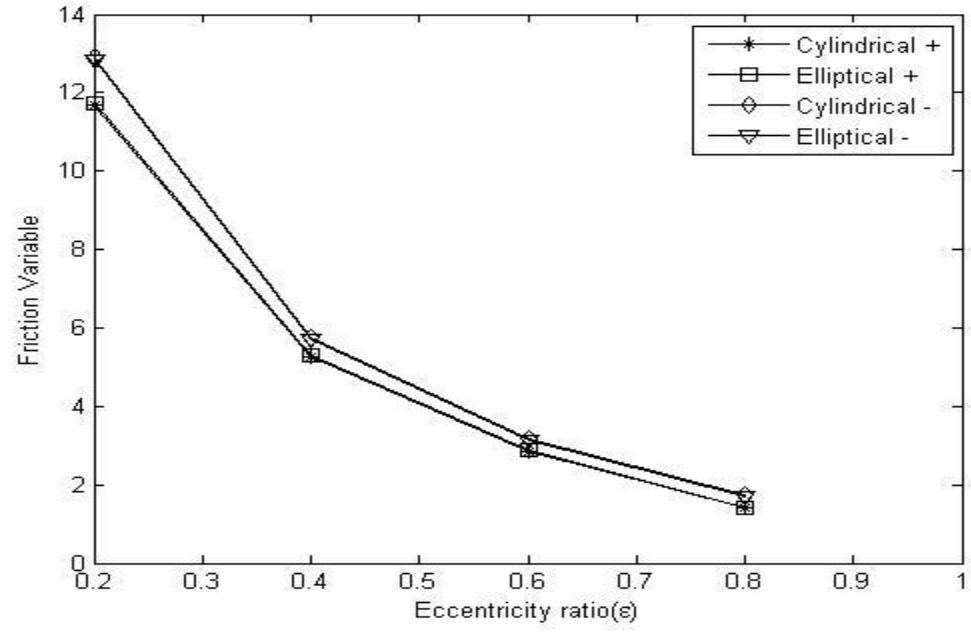

Figure 7.3: Variation of friction variable with eccentricity ratio of textured journal bearing

(L/D=1, S_p = 0.6, $\Delta\bar{h}$ =0.03, α =1, β =1)

7.1.2 Effect of texture area density:

Figures 7.4 through 7.6 represent variations of load carrying capacity, flow coefficient and friction variable with the variation of textured area density of the bearing respectively. It has been observed from these figures that the trends of change in these performance parameters for positive textured bearing and negative textured bearing are opposite to each other. The film thickness at the textured location for the positive textured bearing is reduced, whereas it is increased in case of negative textured bearing. This causes in higher pressure built up in case of positive textured bearing and this should be the reason for better performance of the positive textured bearing. In case of positive cylindrical and elliptical textured journal bearing, load carrying capacity initially increases from un-textured condition to 20% textured area density, then it decreases up to 40% textured area density and finally increases up to 60% textured area density. Load carrying capacity of positive cylindrical textured bearing increases rapidly from 40% to 60% textured area density compared to load carrying capacity of positive elliptical textured bearing. In contrast load carrying capacity of negative cylindrical and elliptical bearing initially decreases from un-textured condition to 20% textured area density, then increases up to 40% textured area density and finally drops up to 60% textured area density. Load carrying capacity of negative cylindrical textured bearing decreases rapidly from 40% to 60% textured area density compared to load carrying capacity of negative elliptical textured bearing as observed from Fig. 7.4. In case of flow coefficient, the trends are similar to that of load carrying capacity except from 20% to 40% textured area density; flow coefficient remains more or less same in this range for both negative and positive textured bearing as has been seen in Fig. 7.5. Friction variable, on the other hand decreases initially from un-textured to 20% textured area density, then increases up to 40% textured area density and finally it decreases up to 60% textured area density for positive cylindrical and elliptical textured bearing, whereas it increases initially up to 20% textured area density, then decreases up to 40% textured area density and finally increases up to 60% textured area density for negative cylindrical and elliptical textured bearing as depicted in Fig. 7.6.

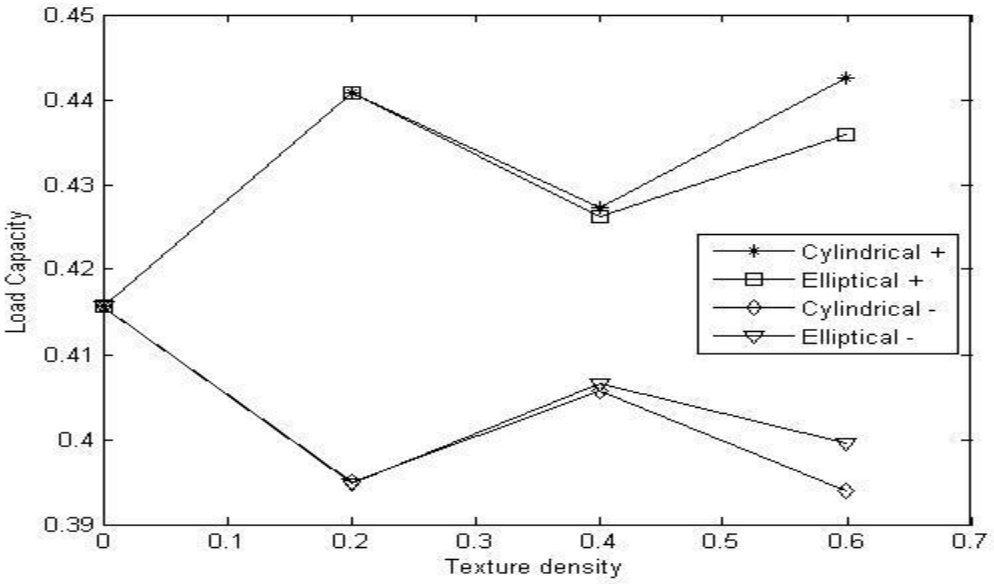

Figure 7.4: Variation of load carrying capacity with texture area density of journal bearing

(L/D=1, ε=0.6, $\Delta\bar{h}$=0.03, α=1, β=1)

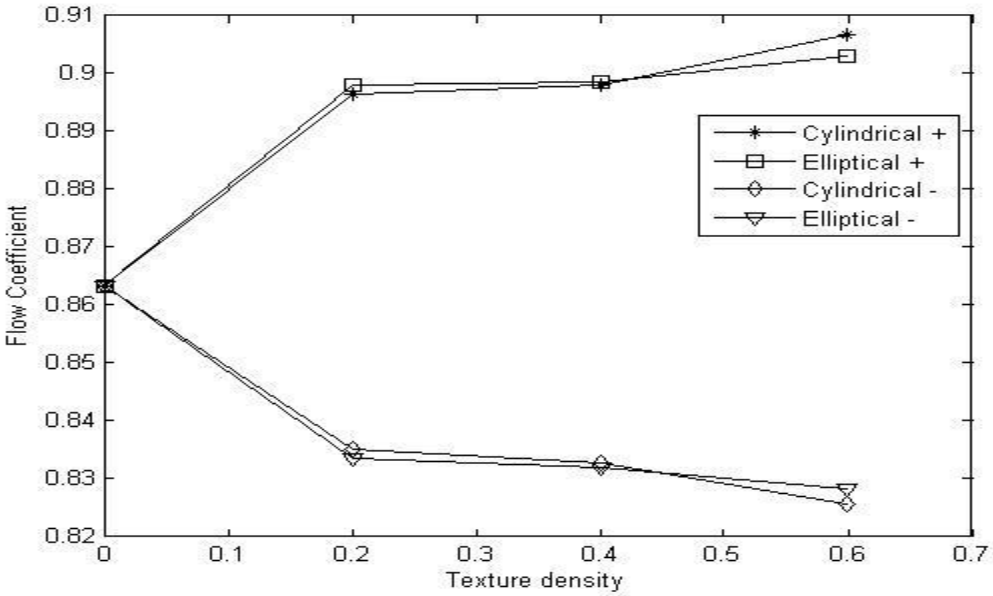

Figure 7.5: Variation of flow coefficient with texture area density of journal bearing

(L/D=1, ε=0.6, $\Delta\bar{h}$=0.03, α=1, β=1)

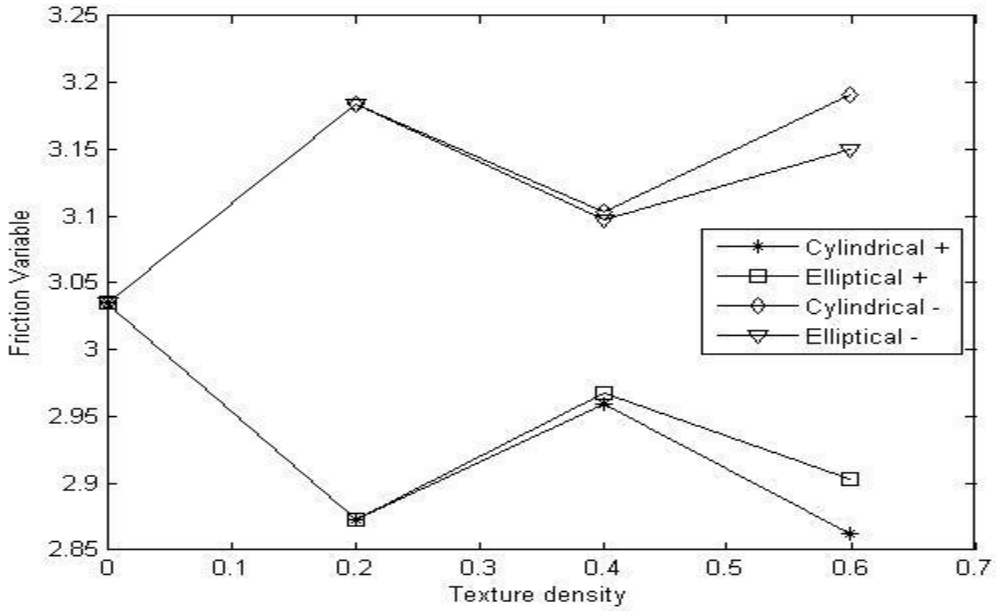

Figure 7.6: Variation of friction variable with texture area density of journal bearing

(L/D=1, ε=0.6, $\Delta\bar{h}$=0.03, α=1, β=1)

7.1.3 Effect of texture portion in circumferential direction:

Load carrying capacity, flow coefficient and friction variable have been plotted against textured portion in circumferential direction in Figs. 7.7 through 7.9 for L/D=1, ε=0.6, $\Delta\bar{h}$=0.03, S_p = 0.6. Full texture has been taken in axial direction and textured portion is varied in circumferential direction. Load carrying capacity increases from un-textured to 60% texture in circumferential direction for positive cylindrical and elliptical textured bearings and then remains constant up to fully textured condition. Load carrying capacity decreases with increase in texture portion in circumferential direction from un-textured to 60% texture and then remains constant for both negative cylindrical and elliptical textured journal bearings as seen in Fig. 7.7. When positive cylindrical textured bearing has better load carrying capacity compared to positive elliptical textured bearing, it is observed from the figure that negative cylindrical textured bearing has less load carrying capacity compared to negative elliptical textured bearing beyond 20% textured portion in circumferential direction. Flow coefficient increases from un-textured to 60% textured portion for positive cylindrical and elliptical textured bearings and then remains the same up to fully textured condition. In contrast, flow coefficient considerably decreases for

negative cylindrical and elliptical bearings up to 60% textured portion and then remains the same. Flow coefficient is marginally more in case of positive cylindrical textured bearing compared to positive elliptical textured bearing beyond 20% textured condition. For negative cylindrical and elliptical bearings, the effect of increase in textured portion in circumferential direction on flow coefficient is just the opposite to positive textured bearings. Flow coefficient decreases with increase in textured portion in circumferential direction up to 60% textured condition and then it remains almost constant up to fully textured condition as seen in Fig. 7.8. Friction reduces considerably for positive textured bearings, when it increases in case of negative textured bearings from un-textured to 60% textured portion.

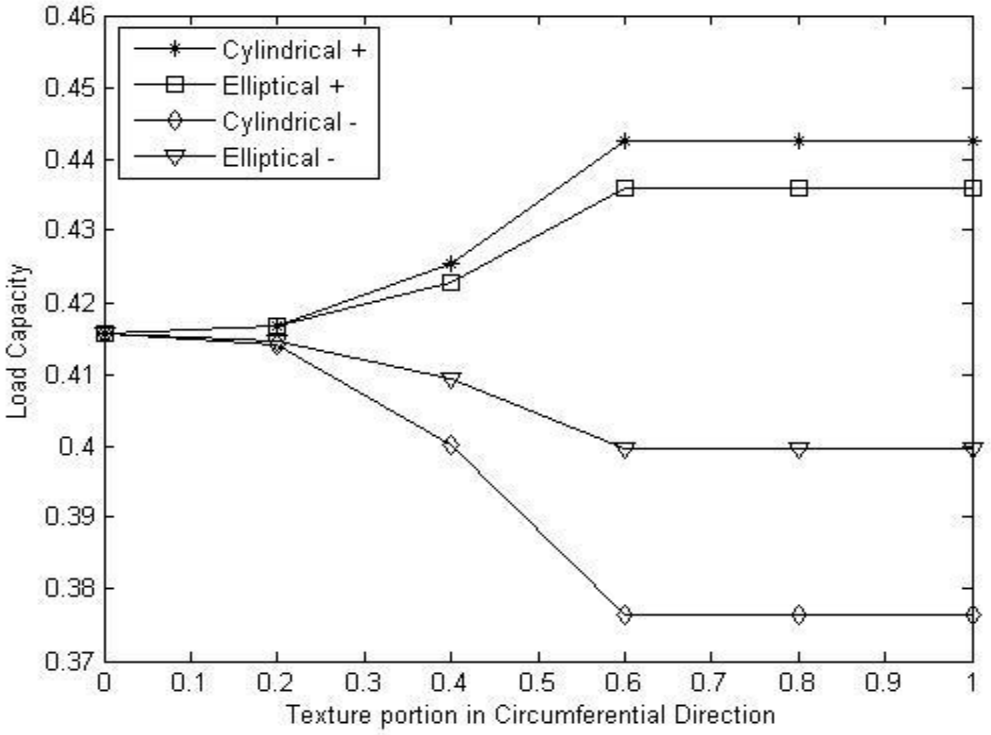

Figure 7.7: Variation of load carrying capacity with textured portion in circumferential direction of journal bearing (L/D=1, ε =0.6, $\Delta\bar{h}$ =0.03, S_p = 0.6, β =1)

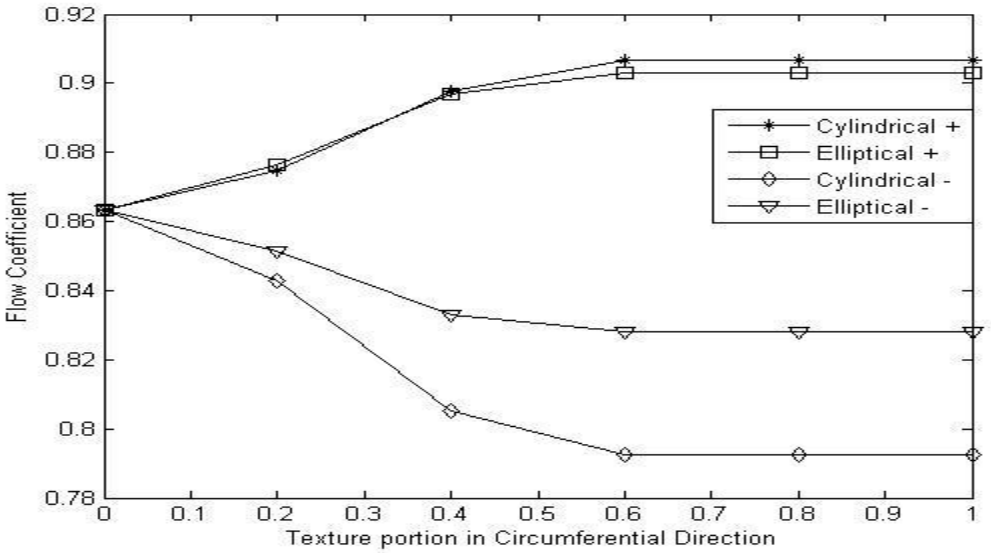

Figure 7.8: Variation of flow coefficient with textured portion in circumferential direction of journal bearing (L/D=1, ε =0.6, $\Delta\bar{h}$ =0.03, S_p = 0.6, β =1)

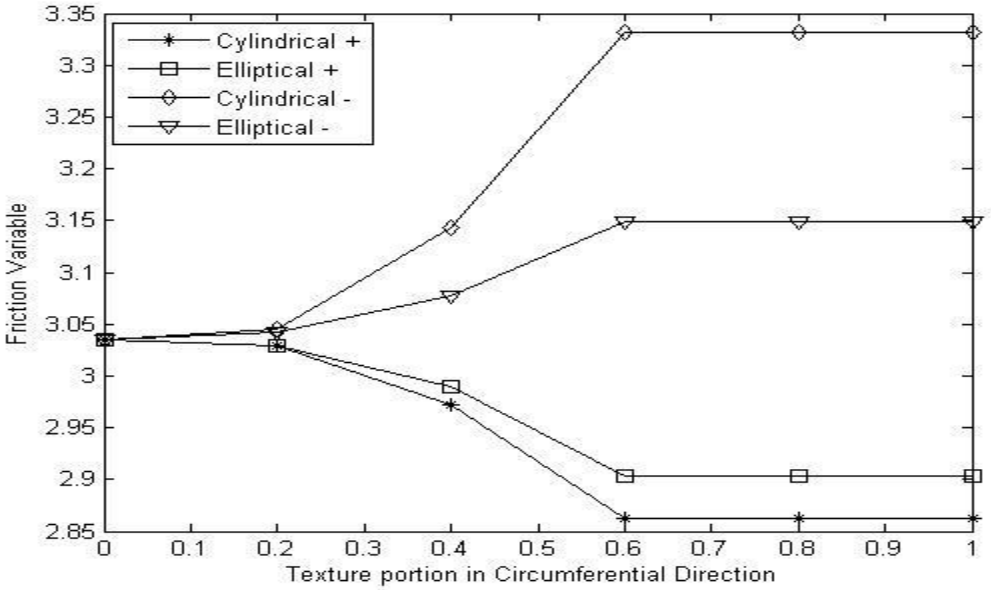

Figure 7.9: Variation of friction variable with textured portion in circumferential direction of journal bearing (L/D=1, ε =0.6, $\Delta\bar{h}$ =0.03, S_p = 0.6, β =1)

7.1.4 Effect of texture portion in axial direction:

Load carrying capacity, flow coefficient and friction variable have been plotted against textured portion in axial direction for L/D=1, ε=0.6, $\Delta\bar{h}$=0.03, S_p = 0.6 in Figs. 7.10 through 7.12. Full texture has been considered in circumferential direction and textured portion is varied in axial direction. Full texturing has high load carrying capacity for both positive cylindrical and elliptical textured journal bearings. Load carrying capacity of positive textured journal bearing is better than that of negative textured journal bearing as seen in Fig. 7.10. Positive texturing in axial direction improves flow coefficient compared to un-textured bearing. Full texturing gives better flow coefficient for both positive cylindrical and elliptical textured journal bearings, cylindrical bearing exhibiting better. However, negative texturing results in deterioration in flow coefficient for both cylindrical and elliptical textured bearings as depicted in Fig. 7.11. On the other hand, it has been observed that friction variable decreases with increase in textured portion in axial direction for positive texture, when it increases for negative texture as observed from Fig. 7.12. As a whole, it may be inferred that full texturing results in better performance for both positive cylindrical and elliptical textured journal bearings.

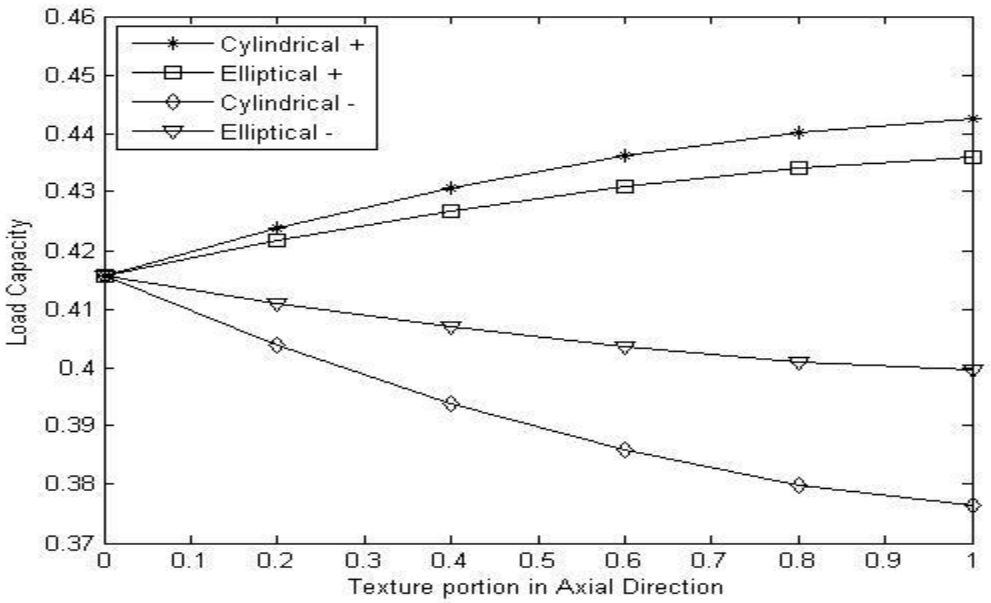

Figure 7.10: Variation of load carrying capacity with textured portion in axial direction of journal bearing (L/D=1, ε=0.6, $\Delta\bar{h}$=0.03, S_p = 0.6, α=1)

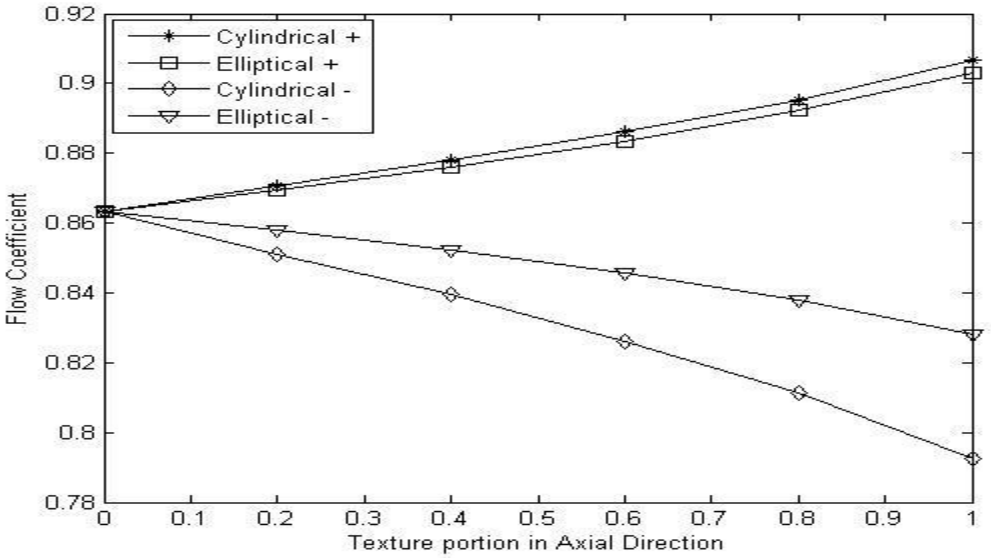

Figure 7.11: Variation of flow coefficient with textured portion in axial direction of journal bearing (L/D=1, ε =0.6, $\Delta\bar{h}$ =0.03, S_p = 0.6, α =1)

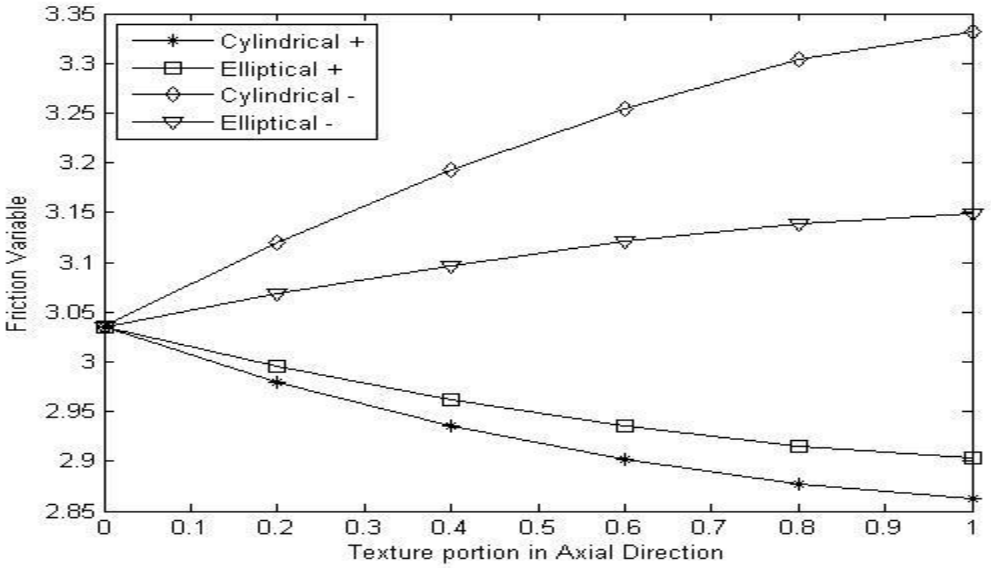

Figure 7.12: Variation of friction variable with textured portion in axial direction of journal bearing (L/D=1, ε =0.6, $\Delta\bar{h}$ =0.03, S_p = 0.6, α =1)

7.1.5 Effect of eccentricity ratio on mass parameter:

Stability map has been presented in Fig. 7.13 for $L/D = 1$, $\Delta\bar{h} = 0.03$, $S_p = 0.6$, $\alpha = 1$, $\beta = 1$. Critical mass parameter, a function of operating speed, has been plotted against eccentricity ratio in the figure for all four types of bearings. It has been observed that the positive textured bearings are more stable up to eccentricity ratio 0.5. Beyond this the negative textured bearings are observed to be more stable. This may be attributed to the reason that negative textured bearings possess better stability at higher eccentricity ratio resulting in better stability. However, stability is a cause of concern particularly at lower eccentricity ratios or lightly loaded bearings. From this point of view, it has been inferred that performance of positive textured cylindrical and elliptical bearing is superior to negative textured cylindrical and elliptical bearing.

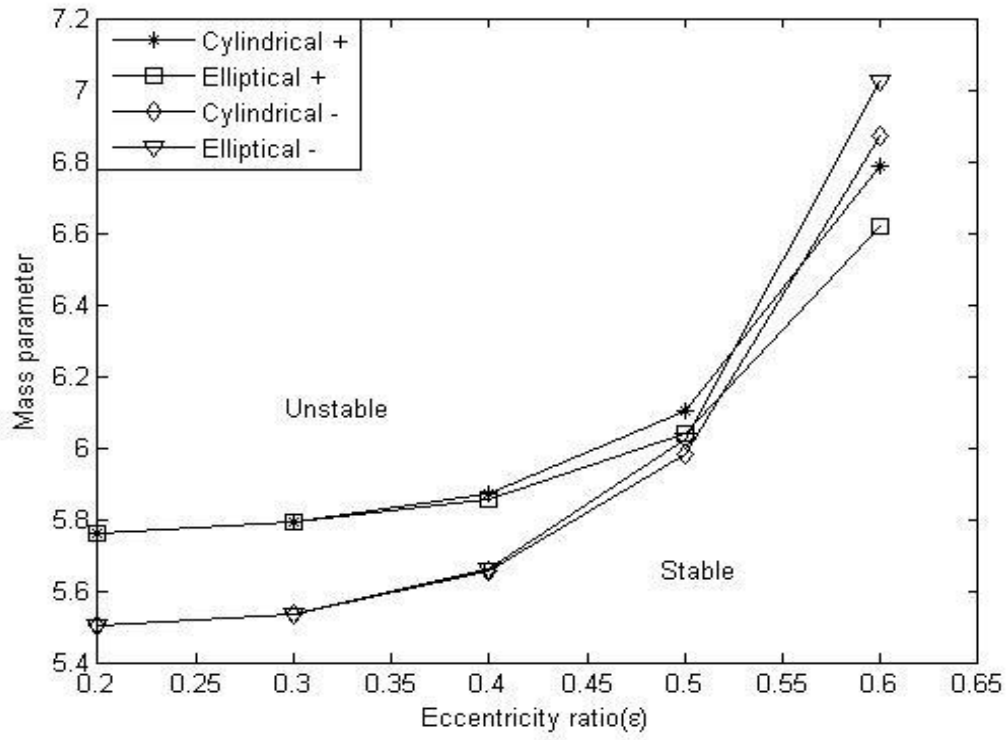

Figure 7.13: Variation of mass parameter with eccentricity ratio ($L/D = 1$, $\Delta\bar{h} = 0.03$, $S_p = 0.6$, $\alpha = 1$, $\beta = 1$)

7.2 Concluding remarks:

From the results it can be inferred that

- Film thickness in case of positive textured bearing in the textured locations is thinner than negative textured bearing, which results in more pressure build-up and it causes better performance in terms of higher load carrying capacity, higher flow coefficient and lower friction variable.
- Stability characteristic of positive textured cylindrical and elliptical bearing is superior to negative textured cylindrical and elliptical bearing particularly for lightly loaded bearings.
- The steady-state performance parameters of positive cylindrical and elliptical textured bearing vary with texture area density, i.e., the parameters do not consistently increase or decrease with increase in texture density. Further study may be carried out to find out the optimum texture area density for best performance of such bearings and also to ascertain the cause of such variation.
- Performance parameters of positive cylindrical and elliptical bearings improve up to 60% textured portion in circumferential direction. Therefore, texturing beyond 60% in circumferential direction may be avoided as it does not contribute in improving performance of the bearings.
- Texturing in axial direction, on the other hand, consistently improves the performance of the bearings up to full textured condition. Therefore, full texturing in axial direction is recommended.
- Better stability is exhibited when texture area density is 0.6 between eccentricity ratios 0.2 to 0.3, whereas stability is better for texture area density 0.4 between eccentricity ratios 0.3 to 0.5. Beyond eccentricity ratio 0.5, stability improves for texture area density 0.2. Overall, stability improves for textured bearing as stability of un-textured bearing (texture area density 0.0) is observed to be the minimum.
- It is observed that the critical mass parameter increases with increase in texture portion from un-textured condition up to 40% textured condition, then decreases up to 60% textured condition and finally remains constant up to fully textured condition in circumferential direction in case of cylindrical textured bearing.

- The critical mass parameter decreases from 20% to 40% textured condition and then increases up to fully textured condition in axial direction for eccentricity ratio 0.6. However, in the case of eccentricity ratios 0.2 and 0.4, the critical mass parameter increases steadily from 20% textured condition to fully textured condition in axial direction in case of cylindrical textured bearing.
- It has been observed that when the journal is better stable at eccentricity ratios 0.2 and 0.3 for texture area density 0.6 compared to other texture area density considered, the same is not the case at other eccentricity ratios. Maximum stability is achieved for texture area density 0.4 at eccentricity ratios 0.4, 0.5 and 0.6.
- An interesting observation from the Fig. 6.9 is that stability deteriorates for texture area density 0.6 from eccentricity ratio 0.4 onwards and it is even less than un-textured bearing (texture area density 0.0) at eccentricity ratio 0.6.
- Critical mass parameter increases from un-textured condition to 40% textured portion and then decreases up to 60% textured portion and finally it remains constant up to fully textured condition in circumferential direction for eccentricity ratios 0.4 and 0.6. However the coefficient increases slightly from un-textured condition to 20% textured portion and then it remains more or less the same up to fully textured condition for eccentricity ratio 0.2. Maximum stability is achieved for 40% textured portion for all eccentricity ratios considered in case of elliptical textured bearing.
- Critical mass parameter decreases from 40% textured portion onward for eccentricity ratio 0.6, when there is a slight improvement in stability with increase in textured portion in axial direction for eccentricity ratio 0.2 and 0.4. Maximum stability is achieved up to 40% textured portion for eccentricity ratio 0.6 in case of elliptical textured bearing.

7.3 Scope for future work:

The following issues may be taken up in extending the present work:

- Optimum texture density and textured portion in circumferential and axial directions may be of interest for the designers to ascertain the best performance of cylindrical and elliptical textured bearings, which may be taken up in future.

- The present characterization is limited to cylindrical and elliptical textured bearing for *L/D* ratio 1. It would be better to characterize these bearings for other *L/D* ratios. Also other texture geometries may be taken up for characterization.
- In the present work Reynolds boundary conditions are used. As mentioned in Chapter 2, there are other boundary conditions like JFO, Kicinski etc. It would be interesting to utilize these boundary conditions to characterize the bearings to see if there are any changes in the performance parameters.
- Characterization of bearings theoretically needs experimental validation. Therefore, it is suggested that experimentalists may take up these results for experimental validation.

7.4 Summary:

The thesis includes results pertaining to steady state, dynamic and stability characteristics of cylindrical and elliptical textured bearings. Since the results presented are dimensionless, therefore, a wide range of design data is being generated for the benefit of bearing designers. It is hoped that the present results would be quite useful for bearing designers. However, the results presented here are only for L/D = 1.0 only. The same procedure can be followed for estimation of design data pertaining to L/D other than 1.0.

REFERENCES

[1] Tala-Ighil, N., Fillon, M. and Maspeyrot, P., "Effect of textured area on the performances of a hydrodynamic journal bearing", *Tribology International*, 2011, Vol. 44(3), pp.211–219.

[2] Ma, C. and Zhu, H., "An optimum design model for textured surface with elliptical-shape dimples under hydrodynamic lubrication" *Tribology International*, 2010, Vol. 44(9), pp.987–995.

[3] Kraker, D. A., Ostayen, V.R.A.J. and Rixen, D. J., "Development of a texture averaged reynolds equation", *Tribology International*, 2010, Vol. 43 (11), pp.2100–2109.

[4] Aurelian, F., Patrick, M. and Mohamed, H., "Wall slip effects in (elasto) hydrodynamic journal bearings", *Tribology International*, 2011, Vol. 44 (7), pp. 868–877.

[5] Sinanoglu, C., Nair, F. and Karams, B. M., "Effects of shaft surface texture on journal bearing pressure distribution", *Journal of Materials Processing Technology*, 2005, Vol. 168(2), pp. 344–353.

[6] Adatepe, H., Bıyıklıoglu, A. and Sofuoglu, H., "An experimental investigation on frictional behavior of statically loaded micro-grooved journal bearing", *Tribology International*, 2011, Vol. 44(12), pp. 1942–1948.

[7] Matsumura, T., Iida, F., Hirosea, H. and Yoshino, M., "Micro machining for control of wettability with surface topography", *Journal of Materials Processing Technology*, 2012, Vol. 212(12), pp.2669– 2677.

[8] Matsumura, T., Sadakata, H., Makihata, H. and Yoshino, M. "Micro fabrication on cylinder surface for control of wettability", *Journal of Manufacturing Processes*, 2013, Vol. 15(1), pp.8–13.

[9] Kango, S., Singh, D. and Sharma, R. K., "Numerical investigation on the influence of surface texture on the performance of hydrodynamic journal bearing", *Meccanica*, 2012, Vol. 47(2), pp.469–482.

[10] Brizmer, V. and Kligerman, Y., "A laser surface textured journal bearing", *Journal of Tribology*, 2012, Vol. 134(3) pp. 031702-9.

[11] Marian, V. G., Gabriel, D., Knoll, G. and Filippone, S., "Theoretical and experimental analysis of a laser textured thrust bearing", *Tribology Letters*, 2011, Vol. 44(3), pp. 335–343.

[12] Gherca, A. R, Maspeyrot, P., Hajjam, M. and Fatu, A., "Influence of texture geometry on the hydrodynamic performances of parallel bearings", *Tribology Transactions*, 2013, Vol. 56(3), pp. 321-332.

[13] Li, J. and Wang, X., "Numerical simulation of the influence of the bulges around laser surface textures on the tribological performance", *Tribology Transactions*, 2013, Vol. 56(6), pp. 1011-1018.

[14] Cupillard, S., Glavatskih, S. and Cervantes, M. J, "3D thermo hydrodynamic analysis of a textured slider", *Tribology International*, 2009, Vol. 42(10), pp. 1487–1495.

[15] Rahmani, R., Mirzaee, I., Shirvani, A. and Shirvani, H., "An analytical approach for analysis and optimization of slider bearings with infinite width parallel textures", *Tribology International*, 2010 Vol. 43(8), pp. 1551–1565.

[16] Tønder, K. "Dimpled pivoted plane bearings: modified coefficients", *Tribology International*, 2010, Vol. 43(12), pp. 2303–2307.

[17] Tønder, K. "Hydrodynamic effects of tailored inlet roughness: extended theory", *Tribology International*, 2004, Vol. 37(2), pp.137–142.

[18] Tønder, K. "Effects of striated texturing on pivoted gas sliders", *Tribology International*, 2008, Vol. 41(9), pp. 896–900.

[19] Wolski, M., Podsiadlo, P. and Stachowiak, G. W., "Effects of information loss in texture details due to the PIFS encoding on load and friction in hydrodynamic bearings", *Tribology International*, 2011, Vol.44(12) , pp. 2002–2012.

[20] Pei, S., Ma, S., Xu, H., Wang, F. and Zhang, Y., "A multiscale method of modeling surface texture in hydrodynamic regime", *Tribology International*, 2011, Vol. 44(12), pp. 1810–1818.

[21]Mezghani, S., Demircia, I.,Zahouani, H. and Mansori, M. E., "The effect of groove texture patterns on piston-ring pack friction", *Precision Engineering*, 2012, Vol. 36(2), pp. 210– 217.

[22] Yuan, S., Huang, W. and Wang, X., "Orientation effects of micro-grooves on sliding surfaces", *Tribology International*, 2011, Vol. 44 (9), pp. 1047–1054.

[23] Costa, H. L. and Hutchings, I. M., "Hydrodynamic lubrication of textured steel surfaces under reciprocating sliding conditions", *Tribology International*, 2007, Vol. 40(8), pp. 1227–1238.

[24] Pettersson, U. and Jacobson, S., "Influence of surface texture on boundary lubricated sliding contacts", *Tribology International*, 2003, Vol. 36(11), pp. 857–864.

[25] Vilhena, L. M., Sedlacek, M., Podgornik, B., Vizintin, J., Babnik, A. and Mozina, J., "Surface texturing by pulsed Nd: YAG laser", *Tribology International*, 2009, Vol. 42(10), pp. 1496–1504.

[26] Wang, X., Kato, K., Adachi, K. and Aizawa, K., "Loads carrying capacity map for the surface texture design of SiC Thrust bearing sliding in water", *Tribology International*, 2003, Vol. 36(3), pp. 189–197.

[27] Wang, X., Kato, K., Adachi, K. and Aizawa, K., "The effect of laser texturing of SiC surface on the critical load for the transition of water lubrication mode from hydrodynamic to mixed", *Tribology International*, 2001, Vol. 34(10), pp. 703–711.

[28] Wang, X., Liu, W., Zhou, F. and Zhu, D., "Preliminary investigation of the effect of dimple size on friction in line contacts", *Tribology International*, 2009, Vol. 42(7), pp. 1118–1123.

[29] Shen, C., Huang, W., Ma, G. and Wang, X., "A novel surface texture for magnetic fluid lubrication", *Surface& Coatings Technology*, 2009, Vol. 204(4), pp. 433–439.

[30] Qiu, Y. and Khonsari, M. M., "Experimental investigation of tribological performance of laser textured stainless steel rings", *Tribology International*, 2011, Vol. 44(5), pp. 635–644.

[31] Galda, L., Koszela, W. and Pawlus, P., "Surface geometry of slide bearings after percussive burnishing", *Tribology International*, 2007, Vol. 40(10), pp. 1516–1525.

[32] Das, S., Guha, S. K. and Chattopadhyay, A. K., "Linear stability analysis of hydrodynamic journal bearings under micro polar lubrication", *Tribology International,* 2004, Vol. 38(5), pp. 500-507.

[33] Roy, L. and Laha, S. K., "Steady state and dynamic characteristics of axial grooved journal bearings", *Tribology International,* 2009, Vol. 42(5), pp. 754–761.

[34] Pai, R., Rao, D. S.,Shenoy B. S., and Pai, R. S., "Stability characteristics of a tri-taper journal bearing: a linearized perturbation approach", *Journal of Materials Research and Technology,* 2012, Vol. 1(2), pp. 84–90.

[35] Chetti, B. "Micro polar fluids effects on the dynamic characteristics of four-lobe journal bearing", *World Academy of Science, Engineering and Technology,* 2011, Vol. 5(11), pp. 11–28.

[36] Kini, M. V., Pai, R. S., Rao, D. S., Shenoy, B. S. and Pai, R., "Effect of groove location on the dynamic characteristics of multiple axial groove water lubricated journal bearing", *World Academy of Science, Engineering and Technology,* 2009, Vol. 3(12), pp. 12–24.

[37] Brizmer, V., Kligerman, Y. and Etsion, I., "A laser surface textured parallel thrust bearing," *Tribology Transactions,* 2003, Vol. 46(3), pp. 397-403.

[38] Qiu, M., Delic, A. and Raeymaekers, B., "The effect of texture shape on the load-carrying capacity of gas-lubricated parallel slider bearings," Tribol Lett DOI 10.1007/s11249-012-0027-4.

[39] Roy, L. and Kakoty, S. K., "Optimum groove location of hydrodynamic journal bearing using genetic algorithm", *Advances in Tribology,* Vol. 2013, Article ID 580367, 13 pages, 2013. doi:10.1155/2013/580367.

[40] Majumdar, B. C., "Introduction to tribology of bearings," *A. H. Wheeler & Co., Private Limited,* A. H. Wheeler & Co., Private Limited 1996, 1st Edition.

APPENDIX

$$C1 = \left(\overline{P}_{i+1,j} + \overline{P}_{i-1,j}\right)$$

$$C2 = \left(\frac{D}{L}\right)^2 \left(\overline{P}_{i,j+1} + \overline{P}_{i,j-1}\right)\left(\frac{\Delta\theta}{\Delta\overline{Z}}\right)^2$$

$$C3 = -\frac{3}{2}\varepsilon\left(\frac{\overline{P}_{i+1,j} - \overline{P}_{i-1,j}}{\overline{h}_{i,j}}\right)(\Delta\theta)\sin\theta_i$$

$$C4 = \varepsilon\left(\frac{\sin\theta_i}{\overline{h}_{i,j}^3}\right)(\Delta\theta)^2$$

$$C5 = 2\left\{1+\left(\frac{D}{L}\right)^2\left(\frac{\Delta\theta}{\Delta\overline{Z}}\right)^2\right\}$$

List of Publications

1. T S Reddy Ganji and S K Kakoty "Dynamic characteristics and stability of cylindrical textured journal bearing", *International Journal of Recent Advances in Mechanical Engineering*, 2014, Vol.3, no.3, pp.1-14.
2. T S Reddy Ganji and S K Kakoty "Effect of cylindrical texture on dynamic characteristics of journal bearing", *International Journal of Recent Advances in Mechanical Engineering*, 2014, Vol.3, no.4, pp.105-117.
3. T S Reddy Ganji and S K Kakoty "Analysis on micro-elliptical textured journal bearing", *International Journal of Current Engineering and Technology*, 2014, special issue-2 pp.648-650.

Vitae

Born and brought up in Sattenapalli, Andhra Pradesh Mr. Thrisekhar reddy Ganji is the youngest son of Mr. Velugonda reddy and Mrs. Jaya. After schooling from Sattenapalli, he graduated in Mechanical Engineering from Dr. Samuel George Institute of Engineering & Technology, Markapur (Dr. SGIT) in 2007. He took his Master of Engineering (M.E.) degree in Computer aided Design and Manufacturing from Andhra University, Visakhapatnam in 2009. Then he joined Department of Mechanical Engineering of Indian Institute of Technology Guwahati as a Research Scholar in 2010 and worked under supervision of Prof. S K Kakoty.